5-24-2012

Studying Topochemistry of Solid State Photoreactions using Solid State Nuclear Magnetic Resonance Spectroscopy

Sarah Mattler
Washington University in St. Louis

WASHINGTON UNIVERSITY IN ST. LOUIS

Department of Chemistry

Dissertation Examination Committee:
Sophia E. Hayes (Chair)
Mark S. Conradi
Viktor Gruev
Richard Mabbs
Kevin D. Moeller
Jacob Schaefer

Studying Topochemistry of Solid State Photoreactions using Solid State Nuclear Magnetic Resonance Spectroscopy

by

Sarah Jane Mattler

A dissertation presented to the
Graduate School of Arts and Sciences
of Washington University in
partial fulfillment of the
requirements for the degree
of Doctor of Philosophy

May 2012

St. Louis, Missouri

Abstract

[2+2] photocycloadditions have been the basis of study for many years, due to numerous potential applications, for example: optical switches, shape-memory polymers, and photolithography. Even though these reactions have been widely studied, there are still unanswered questions. These cycloadditions in the solid state become more complicated due to the limited movement allowed by solids. Understanding the effect this limit has on the system is necessary for understanding the photoreaction. A specific example is a single-crystal-to-single-crystal (SC to SC) transformation. Generally, materials undergo a SC to SC reaction when irradiated with light in the tail of the absorption band ("tail" irradiations) or wavelength selective irradiations. The reaction progresses differently with broadband irradiations. There are very few materials that actually can undergo a single-crystal-to-single crystal photoreaction. Cinnamic acid is one of those few materials.

Two materials, cinnamic acid and a supramolecular complex, 2(4, 4 bipyridyl ethylene) · 2(resorcinol), have been studied using tail irradiations. Partially-reacted single crystals of cinnamic acid have been examined, and the tensor of the product has been determined. Domain size experiments using spin diffusion have been performed for determining the mechanism of formation of the products under wavelength selective irradiation in cinnamic acid single crystals. The wavelength selective kinetics curve for the supramolecular complex has been determined. The crystal structure of the product has also been determined and confirmed with powder X-ray diffraction and simulations. The third material studied is a shape-memory polymer which was synthesized for the purpose of analyzing the photoreaction and the reversible crosslinking. The results of ^{13}C CP (cross polarization) and CPMAS solid state NMR experiments will be discussed.

Acknowledgements

As I write this I am reminded of all of the people who have helped me to be able to get this far. I would like to thank my committee, Dr. Jake Schaefer and Dr. Kevin Moeller for being there for me in my committee meetings, and for being willing and able to answer any and all questions that I had for you. Thank you for all of your help in my committee meetings helping to make sure that I stayed on track and for helping me to acknowledge the gaps in my knowledge. I would also like to thank my defense committee, Dr. Richard Mabbs, Dr. Viktor Gruev, and Dr. Mark Conradi for being willing to take the time out of their busy schedules to read my thesis and be a part of my defense. I would like to especially thank Dr. Mark Conradi for his help in the design and understanding of my probe. You are always a wealth of knowledge and I have always enjoyed our interactions. I would also like to thank our collaborators on these projects, Dr. Marko Bertmer and Dr. Len MacGillivray.

I need to acknowledge a few people in the Moeller lab for being willing to help a physical chemist actually make something. Thank you to Jennifer Bartels and Laura Anderson for helping Jason and I with synthesis questions and for being a great support group. Thank you, Libo Hu, for synthesis of the polymer in the photo-crosslinking studies.

I would like to thank all of my fellow graduate student group members, former: Stacy, Ryan, Kannan, and Kim and current: Katie, Erika, Dustin, Andy, and Jeremy, for being a part of my life as a graduate student and for being willing to read and edit my thesis. I would like to thank Ryan Nieuwendaal for his previous work on the cinnamic acid materials, as well as his willingness to train a new graduate student on the equipment and the project. I have always admired your knowledge and I wish that I could be more like you as a scientist and a researcher. Any time I have a question, even now you are more than willing with an answer.

One group that I really need to acknowledge is the hardworking undergraduates who have worked on all of the projects with me over the years. Adam Johnson for his help with the probe; Jason Shields for his amazing synthesis abilities, the polymer project would not have progressed without him; Kimberly Hartstein for her hard work with a lamp that was broken most of the time and for her work on the MacGillivray project with the long hours of irradiations; and David Hirsh for his willingness to work on anything that I asked him to, and his friendship. I really could not have gotten here without the tireless efforts of the undergraduates.

I would like to thank everyone in the chemistry department who does work behind the scenes and makes everything run smoothly, especially Greg and Jason for all of their help.

I would like to thank Sophia for being willing to let me into the lab. She really inspired me to love NMR. I would like to thank her for the freedom that she allowed me in my research. Thank you for being willing to always answer questions when I had them. I also want to thank you for allowing us to travel to so many conferences; you are one of the best people at networking and being able to see that helped me to become a better networker as well. I would also like to thank you for being there for me when things were hard, and letting me take the time I needed.

I would like to thank the Alfred P. Sloan Foundation for funding of this project. I would also like to thank the Wheeler Fellowship for the funding to be able to write my thesis.

Last but not least, I would like to thank my family: Mom, Dad, Hannah, Bekah, Katie, John Daniel, Corey, Dan, and friends: Kenny and Julie Buyle (et.al.), Toni and Dave Jackson, Susan Mallien, for being awesome and supportive of me in my graduate studies and in life.

I would especially like to thank my husband, Kevin Mattler, for being willing to put up with me writing my thesis and being an amazing and wonderful man, and for being willing to sit

through countless conversations about work. This thesis is dedicated to you.

Table of Contents

List of Figures

List of Tables

List of Schemes

Abbreviations

NMR: nuclear magnetic resonance spectroscopy

^{1}H: hydrogen isotope (also referred to as proton)

^{13}C: carbon 13 isotope

T_1: spin lattice relaxation time

rf: radio frequency

SWR: standing wave ratio

OPNMR: optically pumped nuclear magnetic resonance

B_1: induced magnetic field

RT: room temperature

MHV: miniature high voltage

CP: cross polarization

MAS: Magic Angle Spinning

CSA: chemical shift anisotropy

CPMAS: cross polarization magic angle spinning

TPPM: two pulse phase modulation

TMS: tetramethyl silane

UV: ultraviolet

SC-to-SC: single crystal to single crystal

PolyCEMA: poly (cinnamoyl oxyethyl methacrylate)

CEMA: cinnamoyl oxyethyl methacrylate

HEMA: hydroxyethyl methacrylate

EDC: 1-ethyl-3-(3-dimethylaminopropyl) carbodiimide

DMAP: 4-dimethylaminopyridine

AIBN: azobisisobutyronitrile

ATRP: atom transfer radical polymerization

CPU: central processing unit

res: resorcinol

bpe: bipyridyl ethylene

bpe·res: bipyridylethylene resorcinol co-crystal

tpcb·res: *rctt*-(tetrakis (4-pyridyl) cyclobutane) · 2(resorcinol)

pXRD: powder X-ray diffraction

GIAO: gauge-independent atomic orbital

JMAK: Johnson-Mehl-Avrami-Kolmogorov

“The most beautiful thing we can experience is the mysterious. It is the source of all true art and science.” –Albert Einstein

Chapter 1: Introduction

There has been a recent resurgence of interest in studying solid state photoreactive materials due to the potential for using the rigidity of the crystal lattice to create covalent bonds in an environment that can be stereoselective, also known as "topochemistry". Being able to manipulate solid state systems can be imperative for tailoring materials for specific applications. Solid state reactions can also remove the need for harsh organic solvents, creating a more environmentally-friendly technique for synthesis of particular materials. In recent years, co-crystallizations have been performed using mechanochemistry, removing most or all of the solvent[1]. These photoreactions have been used in many different types of applications and a number of these undergo a [2+2] photocycloaddition in the solid state. Some of the original uses were in photolithography, where poly (vinyl cinnamate) was originally developed by Minsk at Kodak as a negative photoresist[2]. These photoreactions have been used in metal organic polymer frameworks (MOFs) to form 3D lattice structures[3], shape-memory[4] and crack healing polymers[5], and in the formation of micelles[6–10]. One of the most common applications is the use of cinnamic acid derivatives as the active ingredient in sunscreens[11,12].

The original theoretical foundations of predicting pericyclic reactions, of which [2+2] photocycloadditions are a subset, were developed by Woodward and Hoffmann[13]. The "Woodward-Hoffmann rules" are based on arguments of orbital symmetry in which, for [2+2] photocycloadditions, an electron is promoted to a higher energy orbital, generally the LUMO (lowest unoccupied molecular orbital), to allow a reaction to occur. The basic energy diagram,

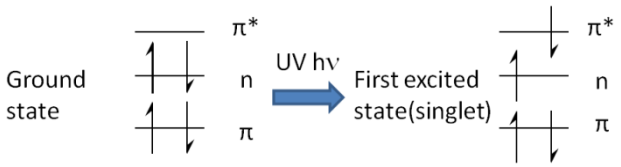

Figure 1.1: Ground state versus first excited state for the basic [2+2] photocycloaddition.

shown in Figure 1.1, provides a schematic of the process. Once in the excited state, several options exist: the singlet can return to the ground state through fluorescence (or internal conversion), it can undergo a spin flip in the excited state to form a triplet and then react, or it can react directly as a singlet[14]. There are also arguments for regioselectivity and specific stereochemistry of the substituents on the cyclobutane ring[14,15]. There have been many studies done on gas phase simulations in which the role of conical intersections has a large effect on the regioselectivity of the substituted [2+2] photocycloaddition reactions[16–18]. In solution studies of these photoreactions, multiple stereoisomers can develop as opposed to solid state studies in which, due to the orientational limitations, only one stereoisomer can develop.

The original definition of topochemistry was developed in 1919 by Kohlschütter, in which he noted the relation between the reactions occurring in the solid state and the spatial location of the products[19]. The first systematic studies of [2+2] photocycloadditions in the solid state were performed on cinnamic acid derivatives by Cohen and Schmidt in the 1960's[20–22]. There are structural limitations to the reaction that are not present in solution-phase experiments. From the study of these cinnamates the so-called topochemical postulate[20–22] was developed for determining reactivity in the solid state. The postulate utilizes constraints based on motion and crystal packing. The postulate states that reaction occurs with limited atomic or molecular movement. The constraints of the topochemical postulate were that reactive vinyl bonds must be parallel and within a distance of 4.2Å to be photoreactive. An example of this is given for the different polymorphs of cinnamic acid in Figure 1.2. In α-trans-cinnamic acid, the vinyl carbons are separated by a distance of 3.5Å, and in β-trans-cinnamic acid they are separated by a distance of 4.01Å (based on published X-ray crystal structures). There is a third polymorph, γ-*trans*-cinnamic acid, (not shown) that is not reactive due to the distance (5Å)

between the vinyl carbons. This distance constraint is not a stead-fast rule and there are a few exceptions, such as coumarins[23]. Note that the original orientation of molecules of the reactant determines the product formed (in solids). For example, the head-to-tail orientation of α-

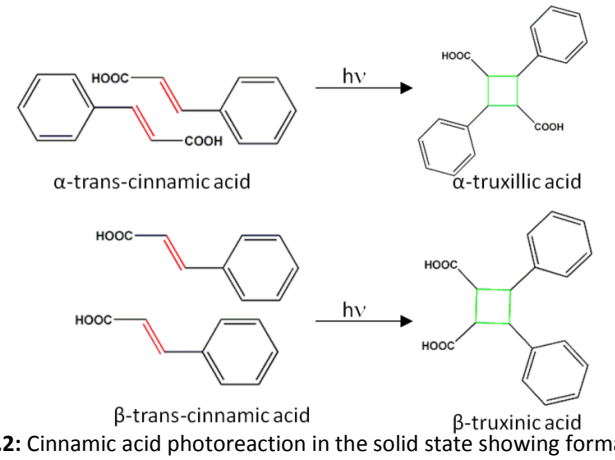

Figure 1.2: Cinnamic acid photoreaction in the solid state showing formation of products.

cinnnamic acid forms the trans product selectively, whereas the head-to-head orientation of β-cinnamic acid forms the cis product selectively (see Figure 1.2). There is an added complication to the photoreactions in the solid state, especially when it comes to predicting product crystal

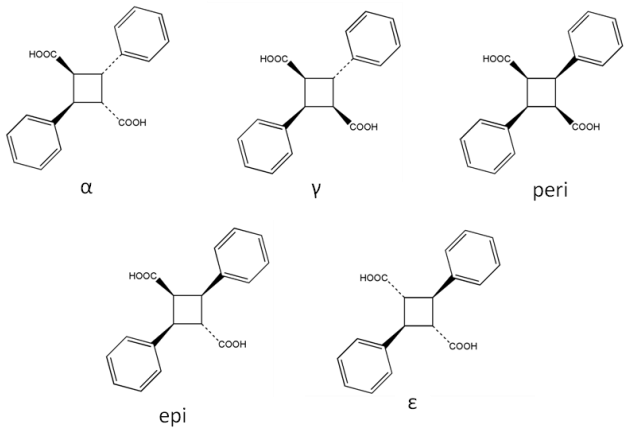

Figure 1.3: The diastereomers of truxillic acid product that can develop.

structures, due to changes in packing that can occur from re-arrangement of atoms, producing multiple polymorphs[24]. The five different diastereomers of truxillic acid that may exist are given in Figure1.3. The product that forms in the solid state is the α isomer[25].

A recent area of interest has been to use and manipulate what is known about solid state reactivity and connectivity to begin to look at crystal engineering in which materials are tailored for specific properties and structures. Some of the leading figures in this area of crystal engineering are Desiraju[26,27] and MacGillivray [28-31]. The topochemical postulate, developed and defined above, has been the motivation for development of crystals specifically engineered for photoreactivity. The MacGillivray lab uses supramolecular complexes to form templates that bring reactive groups within close proximity. These supramolecular complexes use hydrogen bonding to orient normally unreactive molecules into a configuration that meets the criteria for the topochemistry.

Solid state nuclear magnetic resonance spectroscopy is an excellent technique for the analysis of solid state reactivity as well as determination of the mechanisms under which solid state photoreactions occur. The advantage of using solid state NMR is that it is a non-destructive technique and there is no physical processing that must be done to the sample for analysis. NMR is also element selective and quantitative. The technique of solid state NMR can be used on many different types of materials such as amorphous materials (i.e. glasses or polymers) and well-ordered crystalline materials. The solid state NMR techniques used will be described in Chapter 2.

Scope of Thesis

This thesis is organized into seven chapters. Chapter 2 focuses on the fundamentals of solid state NMR and the basic NMR experiments used in this thesis. Chapter 3 focuses on the design of a probe developed for a specific application. Chapter 4 analyzes the [2+2] photocycloaddition in a single crystal of cinnamic acid. Though cinnamic acid has been well-studied, the mechanism of the single-crystal-to-single-crystal photoreaction has not been

determined. Chapter 4 will elucidate the mechanism of product formation using single crystal NMR. Also, the meta-stable polymorph has been produced in the single crystal photoreaction, and the chemical shift tensor for this polymorph is measured. Chapter 5 analyzes wavelength selective photoreaction kinetics of a supramolecular complex, from the MacGillivray lab, which has been performed using solid state NMR. These experiments coupled with powder X-ray diffraction and simulations confirm the product structure that develops. Chapter 6 focuses on a shape-memory polymer that has been synthesized for analysis of the [2+2] photocrosslinking that it undergoes when irradiated with UV light. Chapter 7 then concludes the thesis with the summary of each chapter and future work.

1.2 References

(1) Friščić, T. *Journal of Materials Chemistry* **2010**, *20*, 7599.

(2) Minsk, L. M.; Smith, J. G.; van Deusen, W. P.; Wright, J. F. *Journal of Applied Polymer Science* **1959**, *2*, 302-307.

(3) Poong, J. I.; Koo, H. G.; Park, H. M.; Jang, S. P.; Lee, Y. J.; Kim, C.; Kim, S.-J.; Kim, Y. *Inorganica Chimica Acta* **2011**, *376*, 605-611.

(4) Lendlein, A.; Jiang, H.; Junger, O.; Langer, R. *Nature* **2005**, *434*, 695-697.

(5) Chung, C.; Roh, Y.; Cho, S.; Kim, J. *Chemistry of Materials* **2004**, *16*, 3982-3984.

(6) Ding, J.; Liu, G. *Macromolecules* **1998**, *31*, 6554-6558.

(7) Liu, F.; Liu, G. *Macromolecules* **2001**, *34*, 1302-1307.

(8) Tao, J.; Liu, G.; Ding, J.; Yang, M. *Macromolecules* **1997**, *30*, 4084-4089.

(9) Henselwood, F.; Liu, G. *Polymer* **1997**, *30*, 488-493.

(10) Kousaka, S.; Sugahara, M.; Endo, T.; Yusa, S.-ichi *Journal of Physics: Conference Series* **2011**, *012012*, 1-4.

(11) Salvador, A.; Chisvert, A. *Analytica Chimica Acta* **2005**, *537*, 1-14.

(12) Giokas, D. L.; Salvador, A.; Chisvert, A. *TrAC Trends in Analytical Chemistry* **2007**, *26*, 360-374.

(13) Hoffmann, R.; Woodward, R. . *Science* **1970**, *167*, 825-831.

(14) Schuster, D. I.; Kaprinidis, N.; Wink, D. J.; Dewan, J. C. *Society* **1991**, *56*, 561-567.

(15) Shen, R.; Corey, E. J. *Organic Letters* **2007**, *9*, 1057-1059.

(16) Bentzien, J.; Klessinger, M. *The Journal of Organic Chemistry* **1994**, *59*, 4887-4894.

(17) Bernardi, F.; De, S.; Olivucci, M.; Robb, M. A. *Journal of the American Chemical Society* **1990**, *112*, 1737-1744.

(18) Bernardi, F.; Olivucci, M.; Robb, M. A. *Accounts of Chemical Research* **1990**, *23*, 405-412.

(19) Boldyrev, V. V. *Reactivity of Solids* **1990**, *8*, 231-246.

(20) Cohen, M. D.; Schmidt, G. M. *Journal of the Chemical Society* **1964**, *June*, 1996-2000.

(21) Cohen, M. D.; Schmidt, G. M.; Sonntag, F. I. *Journal of the Chemical Society* **1964**, 2000-2013.

(22) Schmidt, G. M. J. *Journal of the Chemical Society* **1964**, 2014-2021.

(23) Nakanishi, B. Y. H.; Hasegawa, M.; Mori, T. *Acta Crystallographica* **1985**, *C41*, 70-71.

(24) Desiraju, G. R. *Crystal Growth & Design* **2008**, *8*, 3-5.

(25) Berg, U. In *The Chemistry of Cyclobutanes*; Rapport, Z.; Liebman, Joel, F., Eds.; John Wiley & Sons, Ltd.: Hoboken, 2005; pp. 96-98.

(26) Desiraju, G. R. *Angewandte Chemie International Edition* **1995**, *34*, 2311-2327.

(27) Kearsley, S. K.; Desiraju, G. R. *Proceedings of the Royal Society A* **1985**, *397*, 157-181.

(28) Atkinson, M. B. J.; Mariappan, S. V. S.; Bučar, D.-K.; Baltrusaitis, J.; Friščić, T.; Sinada, N. G.; MacGillivray, L. R. *Proceedings of the National Academy of Sciences of the United States of America* **2011**, *108*, 10974-9.

(29) Macgillivray, L. R.; Papaefstathiou, G. S.; Friščić, T.; Varshney, D. B.; Hamilton, T. D. *Topics In Current Chemistry* **2004**, *248*, 201-221.

(30) MacGillivray, L. R.; Papaefstathiou, G. S.; Friscić, T.; Hamilton, T. D.; Bucar, D.-K.; Chu, Q.; Varshney, D. B.; Georgiev, I. G. *Accounts of Chemical Research* **2008**, *41*, 280-91.

(31) Atkinson, M. B. J.; Bucar, D.-K.; Sokolov, A. N.; Friscić, T.; Robinson, C. N.; Bilal, M. Y.; Sinada, N. G.; Chevannes, A.; MacGillivray, L. R. *Chemical Communications* **2008**, 5713-5.

Chapter 2: Basics of Solid State NMR

2.1 Introduction

Solid state nuclear magnetic resonance spectroscopy (NMR) is a spectroscopic technique that gives insight into connectivity[1–4], orientation, and some motion[5] in solid state molecules. Solid state NMR is useful for studying amorphous and ill-defined materials in addition to well-defined materials such as single crystals[6]. NMR has the capability to give connectivity information as well as orientational information that may not be available with other techniques. This chapter will give a short explanation about solid state NMR in general and then go into details about specific techniques such as cross polarization magic angle spinning (CPMAS). To be able to understand the details of the experiments that are presented it is necessary to understand the basics of NMR, so that when certain techniques are used, the basics have already been explained.

NMR Interactions

There are many types of interactions that occur between different nuclei that contribute to the signal that is seen in NMR. A Hamiltonian can be used to describe all of the possible interactions that can occur between different nuclei[7]. There are several different types of interactions that are present in NMR; these interactions can be split into two categories, external and internal interactions.

$$\boldsymbol{H} = \boldsymbol{H}_{\text{external}} + \boldsymbol{H}_{\text{internal}} \quad (1)$$

The external Hamiltonian consists of any interactions produced from external forces, such as the magnetic field, in $\boldsymbol{H}_o$, which produces the Zeeman splitting, and the coil ($\boldsymbol{H}_{induced}$) that can induce a magnetic field.

$$\boldsymbol{H}_{\text{external}} = \boldsymbol{H}_{\text{o}} + \boldsymbol{H}_{\text{induced}} \quad (2)$$

$$\boldsymbol{H}_{\text{internal}} = \boldsymbol{H}_{\text{DD}} + \boldsymbol{H}_{\text{q}} + \boldsymbol{H}_{\text{s}} + \boldsymbol{H}_{\text{L}} + \boldsymbol{H}_{\text{j}} \quad (3)$$

The internal Hamiltonian is split into several components, dipolar coupling ($\boldsymbol{H}_{DD}$), quadrupolar coupling ($\boldsymbol{H}_{Q}$), chemical shift ($\boldsymbol{H}_{s}$), interactions with the lattice ($\boldsymbol{H}_{L}$), and J-coupling ($\boldsymbol{H}_{j}$). Each portion of the Hamiltonian will be explored in the following sections. The external Hamiltonian will be described first, after which the internal Hamiltonian will be further described. Table 2.1 addresses the properties of the nuclei of interest that are important in the next few sections. There are many other NMR active nuclei, but they will not be addressed here.

Table 2.1: NMR isotope details for nuclei of interest.

Nuclear Isotope	**Spin Quantum Number** ($\mathbf{I}$)	**Gyromagnetic Ratio** (10^6 rad $s^{-1}T^{-1}$)	**Natural Abundance** (%)	**Nutation Frequency** (MHz)
^{1}H	1/2	267.513	99.98	200/ 300
^{13}C	1/2	67.262	1.108	50/ 75

2.2 External Interactions

The first set of interactions to discuss is the nucleus' interaction with external stimuli, such as the external magnetic field and induced magnetic fields (see Equation 2). Each active nucleus has a magnetic moment, $\boldsymbol{\mu}$ [8].

$$\boldsymbol{\mu}=\gamma\mathbf{L}. \quad (4)$$

The term γ in Equation 4 is the gyromagnetic ratio, which relates the magnetic moment to the angular momentum (**L**) of the nucleus. The values for the nuclei of interest are given in Table 1. Equation 4 shows the effect of placing the magnetic moment in a magnetic field; it has some angular momentum associated with it. If you observe the change in angular momentum over time, it equals $\boldsymbol{N}$, which is torque:

$$\frac{d\boldsymbol{L}}{dt} = \boldsymbol{N}. \quad (5)$$

If a nucleus with a magnetic moment is put into a magnetic field, a torque is exerted as the angular momentum changes with time. This torque causes it to precess around the magnetic field.

$$\boldsymbol{N} = \boldsymbol{\mu} \times \mathbf{B}_{\mathrm{o}}, \text{ so } \frac{\mathrm{d}\mathbf{L}}{\mathrm{dt}} = \boldsymbol{\mu} \times \mathbf{B}_{\mathrm{o}} = \gamma \mathbf{L} \times \mathbf{B}_{\mathrm{o}} = -\gamma \mathbf{B}_{\mathrm{o}} \times \mathbf{L} \qquad (6)$$

The above equations show that the magnetic moment of the nucleus precesses about the direction of the magnetic field with an angular frequency ($\boldsymbol{\omega}_o$) of

$$\boldsymbol{\omega}_o = \gamma \boldsymbol{B}_o = 2\pi \boldsymbol{f}_o \qquad (7)$$

$\boldsymbol{f}_o$ is the Larmour precession frequency and is parallel to $\mathbf{B}_0$. For instance, in a 4.7 T magnet ^{1}H precesses at a frequency of 200 MHz.

The above equations are in terms of a classical particle, whereas nuclei behave quantum mechanically, having discrete energies. In the quantum mechanical argument, $\boldsymbol{\mu}$= γħ$\mathbf{I}$, where ħ is Planck's constant/2π, and $\mathbf{I}$ is the spin angular momentum (values in Table 1), which is related to the classical angular momentum**, L**, by

$$\mathbf{L}=\hbar\mathbf{I}. \qquad (8)$$

The potential energy of a single nucleus is

$$U = -\gamma\hbar m B_o. \qquad (9)$$

For the nuclei of interest (^{13}C and ^{1}H), m = ±½. The difference between the two potential energies (U) that the nuclei can populate is $\Delta U = \hbar\gamma B_o$. This is the "Zeeman splitting". Figure 2.1 depicts how the energy levels change as the magnetic field increases.

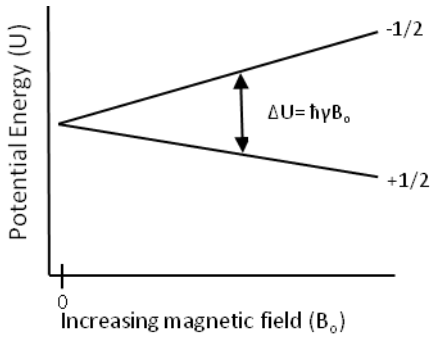

Figure 2.1: Effect of Magnetic Field on Energy levels. The change in energy between the two levels changes as the magnetic field increases. The two lines show the change in energy of the states as the magnetic field changes.

The previous paragraphs have been only about single spins. In real NMR experiments, the sum of all of the spins is what produces magnetization, but remember that there are some spins in the +½ state and -½ state. We must therefore look at the difference in population between the two states to get a measure of the magnetization that is detected in NMR.

$$\frac{N_-}{N_+} = \exp\left\{\frac{-\Delta U}{kT}\right\}, \Delta U = \hbar\omega_o \tag{10}$$

The population difference between the upper and lower states is the difference in energy between the two states weighted by their Boltzmann distribution. This difference is shown in Equation 11.

$$\frac{N_-}{N_+} \approx 1 - \exp\left\{\frac{-\Delta U}{kT}\right\} \tag{11}$$

At normal temperatures we get the expression shown above, due to the fact that $\hbar\omega_o \ll kT$.[8]

The second portion of the external Hamiltonian is a term that is related to a small magnetic field that can be induced which is produced from a coil (denoted $\boldsymbol{H}_{induced}$); this allows for manipulation of the energy levels that are present to detect the NMR signal. It can be described by the following equation:

$$\boldsymbol{H}_{induced} = -\frac{1}{2}\gamma B_1 sin\theta_{rf}\{(cos\omega t + \phi)I_x + (sin\omega t + \phi)I_y\} \tag{12}$$

The Hamiltonian is in terms of the B_1 field (the induced field strength) weighted by the

gyromagnetic ratio (γ). The next portion is the angle (θ_{rf}) of the coil with respect to the external magnetic field. Normally, depending on the experiment, the angle is perpendicular to the magnetic field and therefore this term becomes 1. In magic angle spinning experiments, this angle is set at the magic angle, which will be described in section 2.4. The other components of the pulse produced are described by: $\omega t + \phi$, which describe the frequency (ω), time (t), and phase (ϕ) of the pulse. $I_{x,y}$ are the spin components in the x and y directions respectively.

In NMR, the spins align roughly parallel or antiparallel to the magnetic field. To be able to actually detect the NMR signal, a change in the direction of the precession of the spins needs to be induced. This change in direction requires a smaller magnetic field induced perpendicular to the magnetic field. The small magnetic field is usually induced by a coil that surrounds the sample of interest. The magnetic field is produced by a pulse of radio frequencies at the frequency of interest for the nuclei (see Table 2.1), which creates an oscillating electric current through the coil of wire. Once the spins are tipped into the x-y plane, (aka transverse plane) the current that is going through the coil changes due to the interaction with the spins and this change can be detected. The measurement of the change in the current produces a free induction decay (FID).

2.3 Internal Interactions

The second part of the Hamiltonian for NMR interactions is the internal interactions which come from interactions that are present in the sample; these interactions are due to the electronic environment around the nucleus of interest as well as the other nuclei that are present in the same material. A reminder of the components is as follows:

$$\boldsymbol{H}_{\text{internal}} = \boldsymbol{H}_{DD} + \boldsymbol{H}_{\text{q}} + \boldsymbol{H}_{\text{s}} + \boldsymbol{H}_{\text{L}} + \boldsymbol{H}_{j}.$$

The internal Hamiltonian is made up of the small interactions that occur between nuclei.

$\boldsymbol{H}_{DD}$ is made up of several components: direct dipolar interactions with the same and different spins, as well as indirect interactions of the same spins and different spins. $\boldsymbol{H}_{\mathrm{q}}$ is an effect that only applies to quadrupolar nuclei (spin > ½) since all of the nuclei of interest in this thesis are spin = ½, this term can be ignored. $\boldsymbol{H}_{\mathrm{s}}$ is the shielding term of the Hamiltonian, this term arises from the electronic environment surrounding the nucleus. The electronic environment surrounding the nucleus is what induces the chemical shift that we observe in NMR. $\boldsymbol{H}_{\mathrm{L}}$ is the interaction of the spins with the lattice, or the rest of the sample, which gives information about dynamics and motion. $\boldsymbol{H}_{j}$ is J-coupling, or the interaction of two spins weakly coupled to one another, which is prevalent in liquids. Decoupling, which is used in the solid state NMR experiments, removes this interaction, so it will not be discussed further. Each of the contributions to the internal Hamiltonian will be expanded in the next couple of sections.

Dipolar Coupling

The dipolar interaction in solids is what is usually responsible for the broadening of the signal that is observed in solid state NMR. In liquids NMR, the dipolar interaction is small due to the fact that molecules in the liquid are moving around and so there is a motional averaging of the dipolar interaction [8]. Sometimes there is a need to remove heteronuclear dipolar coupling from samples in solution NMR to simplify the spectra and remove J-coupling from the other nucleus. Decoupling is usually done in ^{13}C solution NMR. In the solid state, this dipolar interaction cannot be removed by motion due to the rigid nature of solid materials. The only way to average it out is to induce a spatial averaging by using magic angle spinning. This dipole-dipole contact interaction can be defined by the following equation:

$$\boldsymbol{H}_{DD} = \sum_{i<j} \mathrm{b_{ij}}\, \mathrm{r}^{-3}(3\cos^2\theta - 1)\ (\mathrm{I_i}\cdot\mathrm{I_j} - 3\mathrm{I_{iz}}\mathrm{I_{jz}}) \tag{13}$$

$$\mathrm{b_{ij}} = \hbar\gamma_i\gamma_j/4\pi \tag{14}$$

Where γ_I, γ_j are the gyromagnetic ratios of the respective nuclei, I_i and I_j are the two spins, b_{ij} is the dipolar coupling constant, r is the inter-spin distance, and θ is the angle between the vector and B_o.[8] There are two different types of these interactions, homonuclear and heteronuclear couplings. The homonuclear dipolar couplings are between similar nuclei (^{1}H - ^{1}H or ^{13}C -^{13}C) and the heteronuclear couplings are between two different nuclei (^{1}H -^{13}C). ^{13}C -^{13}C homonuclear couplings are usually small in natural abundance ^{13}C experiments. The small coupling is due to the fact that ^{13}C nuclei are only 1% naturally abundant, as shown in Table 2.1. These spins are very dilute, thus there is a small probability of having two ^{13}C nuclei next to one another. On the other hand, ^{1}H which has a higher natural abundance has a much larger probability of a neighbor. The strength of the dipolar coupling is also proportional to the gyromagnetic ratio, which for ^{1}H is also 4 times larger as shown in Table 2.1. Both of these contributions make the dipolar coupling due to ^{1}H a much larger effect than that of ^{13}C. In some experiments presented in this thesis, the materials are isotopically labeled with ^{13}C (at specific positions) and so ^{13}C-^{13}C interactions become a larger contribution since the spins are more concentrated. This contribution will be important in determining the linewidth contributions from the single crystals which will be explored in detail in Chapter 4.

Chemical Shift/ Shielding

The next portion of the Hamiltonian that is important is the chemical shielding or chemical shift. Chemical shielding is described using a second rank tensor, **σ**. It is the response of an electronic cloud surrounding a nucleus to an induced magnetic field

$$\boldsymbol{H}_{cs} = -\gamma\hbar\, \mathbf{I}\cdot\boldsymbol{\sigma}\cdot\mathbf{B}_o. \qquad (15)$$

The tensor is made up of several components that describe a three dimensional electronic environment around the nucleus of interest. The shielding tensor is given: $\sigma = \begin{bmatrix} \sigma_{xx} & \sigma_{xy} & \sigma_{xz} \\ \sigma_{yx} & \sigma_{yy} & \sigma_{yz} \\ \sigma_{zx} & \sigma_{zy} & \sigma_{zz} \end{bmatrix}$.

The shielding tensor is mainly described by three terms that are the isotropic portion of the chemical shift (σ_{xx}, σ_{yy}, σ_{zz}). This isotropic portion is described by the terms that are along the diagonal of the matrix of the tensor (of the diagonalized matrix). The tensor can be described by several different values, isotropic chemical shift, the anisotropy, and the asymmetry. These three values have several different conventions; in this thesis the Haeberlen-Mehring-Spiess (Haeberlen) convention will be used[7]. Haeberlen notation is used because it is the convention used in the simulations that were performed with SIMPSON and SIMMOL[9,10].

$$\delta_{iso}\ (\sigma_{iso}) = 1/3(\delta_{zz} + \delta_{yy} + \delta_{xx}) \quad (16)$$

$$\delta_{aniso} = \delta_{zz} - \delta_{iso} \quad (17)$$

$$\eta = (\delta_{yy} - \delta_{xx} / \delta_{aniso}) \quad (18)$$

δ_{iso} is the isotropic chemical shift, σ_{iso} is the isotropic shielding, δ_{aniso} is the anisotropy, and η is the asymmetry. The anisotropy is defined as the largest separation from δ_{iso}, and the asymmetry is defined as the line shape deviation from an axially symmetric tensor. The tensor values are labeled as $\delta_{11} > \delta_{22} > \delta_{33}$ and ordered according to Haeberlen convention: $|\delta_{zz} - \delta_{iso}| \geq |\delta_{xx} - \delta_{iso}| \geq |\delta_{yy} - \delta_{iso}|$. These three values describe the full tensor for chemical shift and shielding. Figure 2 shows how each term is defined. Chemical shift and shielding are related by equation 19:

$$\delta = (\sigma_{ref} - \sigma_{species})/(\sigma_{ref}) \quad (19)$$

The primary reference for ^{1}H and ^{13}C is tetramethylsilane (TMS) which is conventionally defined as 0 ppm.

In most NMR experiments, the scalar term of the chemical shift, the isotropic portion, is what is detected. The isotropic shift is what is observed in solution NMR, as well as solids experiments, in which MAS is used. In solution NMR experiments, there is a motional averaging of the chemical shift tensor because the molecules are moving and tumbling. This motional averaging allows for the scalar term, isotropic shift, to be the only portion of the chemical shift that is detected. There is also an anisotropy that is present that solution NMR experiments do not usually detect, which is shown in Figure 2.2. Depending on the electronic environment there can be different tensor values and anisotropy.

The chemical shift anisotropy (CSA) of a powder can look like the powder pattern in Figure 2.2. This powder pattern can change depending on the electronic environment that is present around the nucleus and the shift values that describe the tensor. This pattern is developed due to the fact that in a powder sample that is unoriented, the crystallites can be in any possible orientation in the magnetic field. The chemical shift tensor, which is interacting

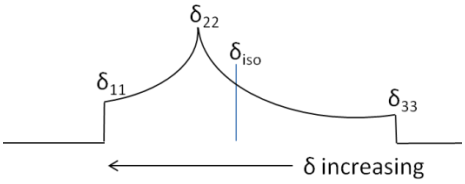

Figure 2.2: Schematic of a powder pattern depicting the terms for chemical shift anisotropy. The lineshape of the powder pattern is determined by the anisotropy.

with the magnetic field, is also oriented in every possible direction. The variation in orientation of the chemical shift tensors and crystallites produces the powder pattern shown as an example in Figure 2.2.

In single crystal experiments, the chemical shift anisotropy is mapped out as the orientation of the crystal is changed. Only a limited number of orientations are present in single crystals, proportional to the number of molecules in the unit cell. In cinnamic acid, for example,

there are two magnetically inequivalent vinyl carbons (isotopically labeled) hence two chemical

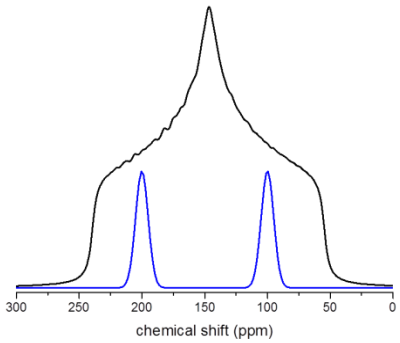

Figure 2.3: Simulated powder pattern for vinyl carbon of cinnamic acid (black) and the simulated chemical shifts for a specific orientation of the single crystal (blue).

shifts at a specific position, shown in Figure 2.3 in blue. As the orientation of the crystal is changed, the chemical shift will change as well.

Interaction with the Lattice

The last portion of the internal Hamiltonian ($\boldsymbol{H}_L$) is the interaction with the lattice, or the rest of the material. The interactions with the lattice involve dynamics, such as relaxation and motion in the solid state (T_1, T_2, and $T_{1\rho}$). There is much information contained in the terms that are present in this portion of the Hamiltonian. Just the basics will be covered in this portion, since an entire book could be written about this part alone. The portions described in this section will be only those that are applicable to this thesis. If interested, there are several books on the subject[11,12].

There are several different types of relaxation that occur in NMR. The first type of relaxation is named T_1, the spin lattice relaxation time constant. This relaxation time is the amount of time that it takes for the z-component of the magnetization to return to the normal Boltzmann distribution along the z direction (the direction of the magnetic field) after a pulse. The spin lattice relaxation time can be measured by inversion recovery[13] or by saturation recovery experiments[13]. T_2 is the spin-spin relaxation time, or transverse relaxation time, the

time it takes for the signal to decay in the transverse plane (x-y plane). Spin lattice relaxation time in the rotating frame, denoted $T_{1\rho}$, is another type of relaxation that can be measured experimentally. This relaxation refers to "the rate at which a nuclear magnetization, spin-locked in the rotating frame, re-approaches its thermal equilibrium value"[8]. This relaxation constant can generally be determined from a variable spin lock experiment. It can also be measured indirectly using CPMAS experiments with variable contact times. In general the order of the relaxation terms is $T_2 \leq T_{1\rho} \leq T_1$.

2.4 Experimental Techniques

Cross polarization (CP)

Cross Polarization (CP) is used to increase the amount of signal from a low natural abundance and low γ nucleus. It does this by transferring polarization from an abundant nuclear spin, ^1H, to a dilute spin, ^{13}C, typically in solids this is done through a dipole-dipole interaction. CP can be coupled with MAS to enhance the signal of powders and amorphous materials[14–16]. The basics of this heteronuclear interaction will be described.

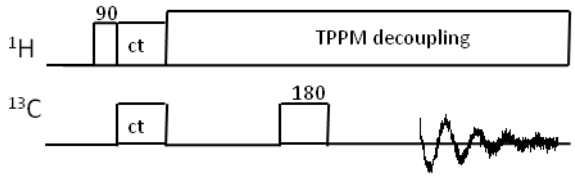

Figure 2.4: A typical cross polarization echo pulse sequence.

A basic pulse sequence for CP is shown in Figure 2.4. As stated earlier, cross polarization is a signal enhancement technique. In this technique, polarization is transferred from ^1H to ^{13}C. The transfer of polarization is done with rf irradiation and manipulation of the spins with the right energy to produce a transition between ^1H and ^{13}C. The first step is to transfer ^1H magnetization into the x-y plane where it is detectable, which is done with a 90° (π/2) pulse.

Then, a specific spin lock pulse is used which allows ^{1}H and ^{13}C to interact with one another. This spin lock pulse is set so that a condition allowing the spins to interact is produced. This condition is called the Hartmann-Hahn match, in which

$$\omega_H = \omega_C \tag{20}$$

where $\omega_{H,C}$ are the frequencies of the ^{1}H and ^{13}C respectively, $\omega_{H,C} = \gamma B_{1H,C}$.

The precession frequency of the spin lock pulse for each nucleus must be equal. When this condition is met, the spins can interact and polarization can be transferred. Then detection of the enhanced ^{13}C spins can be done, with better signal than a normal ^{13}C experiment. CP experiments can also give information about connectivity as well as some dynamics. These dynamics can be used to manipulate the spins and allow for spectral editing of the different species present in a sample. In CP there is a build-up time for the magnetization. This build-up time is dependent on the proximity of a ^{1}H to a ^{13}C species. Directly protonated species have a much faster build-up of signal than species which are not directly protonated, or have motion, such as a CH_3 group. Cross polarization dynamics of different CH_x species, referred to as carbon multiplicities, can be manipulated to edit for specific types, such as a CH versus a CH_3. This "spectral editing" is done by utilizing the differences in ^{13}C-^{1}H dipolar couplings and CP dynamics for assignment of specific resonances in CPMAS experiments[17–20].

Magic Angle Spinning

To be able to only acquire the isotropic chemical shift in powdered materials, there must be some way to induce some type of averaging in the materials with respect to the magnetic field. If this could be possible, then each crystallite would have the isotropic shift on average. Magic angle spinning (MAS) is such a technique[7,8,15]. When a sample is spun at a particular angle with respect to the magnetic field, there is a spatial averaging of the chemical

shift anisotropy of each crystallite. Since the position of each crystallite is changing as the sample is being spun, the portion of the tensor of each nucleus that is interacting with the magnetic field is changing as the position is changing, hence an induced spatial averaging, similar to the averaging seen from the rapid motion in solution NMR experiments. This spatial averaging produces the isotropic chemical shift. Now instead of getting full chemical shift anisotropy (CSA), there is a single peak for each tensor. Magic angle spinning affects the dipolar coupling as well. The magic angle is set based on the $(3\cos^2 \theta\text{-}1)$ factor that is present in the CSA and dipolar terms. If the angle is set to 54.7^{o}, then this term averages to zero. Being at the magic angle, coupled with dipolar decoupling techniques (described in the following section), narrows the linewidths in solid state NMR experiments, and allows for resolution of individual peaks.

Dipolar Decoupling

Dipolar decoupling is a technique used to suppress internuclear interactions from the NMR spectra. In solids, dipolar coupling is responsible for a large amount of the broadening that occurs. In carbon NMR experiments in which there are protons present, it is necessary to have decoupling on to remove this interaction and narrow the signals so that specific peaks can be resolved. There are specific types of experiments that can remove dipolar coupling. In general, irradiation of the proton frequency continuously will remove this interaction. The technique used in this thesis is two pulse phase modulation (TPPM) decoupling[21] in which two pulses (8.3 μs) of alternating phase ($\pm$ 12.5°) are used to remove the protons from interacting with the carbon nuclei.

Spin Diffusion Experiments

Spin diffusion is based on an experimentally observed diffusive behavior of magnetization transfer, due to exchange between spins[22]. This spin diffusion can give

information about the structure of materials, especially mixtures. Spin diffusion measurements have been used in mixtures of polymers with two different domains, (crystalline and amorphous) to probe the respective sizes through the manipulation of spin diffusion[22]. To perform spin diffusion experiments, a spatially inhomogeneous distribution of magnetization needs to be generated and then allowed to exchange. If domains are small, then exchange will be fast, and if domains are large then magnetization exchanges more slowly to the second domain. The technique used to measure domain sizes will be explained in Chapter 4.

2.5 References

(1) Baccile, N.; Laurent, G.; Babonneau, F.; Fayon, F.; Titirici, M.-magdalena; Antonietti, M. *Journal of Physical Chemisty C* **2009**, *113*, 9644-9654.

(2) Kolodziejski, W.; Klinowski, J. *Chemical Reviews* **2002**, *102*, 613-28.

(3) Borisov, A. S.; Hazendonk, P.; Hayes, P. G. *Journal of Inorganic and Organometallic Polymers and Materials* **2010**, *20*, 183-212.

(4) Choi, N. Amorphous , Multi-phase Polymer Network Systems with Shape-Memory Properties by Photopolymerization, RWTH Aachen, 2002.

(5) Rothwell, W. P. *The Journal of Chemical Physics* **1981**, *74*, 2721.

(6) *NMR Crystallography*; Harris, R. K.; Wasylishen, R. E.; Duer, M. J., Eds.; John Wiley and Sons, Ltd.: Chichester, UK, 2009.

(7) Mehring *Principles of High-resolution NMR spectroscopy in Solids*; Diehl, P.; Fluck, E.; Kosfeld, R., Eds.; Springer-Verlag: New York, 1976; pp. 6-166.

(8) Stejskal, E. O.; Memory, J. D. *High Resolution NMR in the Solid State*; Oxford University Press: New York, 1994; pp. 3-142.

(9) Bak, M.; Rasmussen, J. T.; Nielsen, N. C. *Journal of Magnetic Resonance* **2000**, *147*, 296-330.

(10) Bak, M.; Schultz, R.; Vosegaard, T.; Nielsen, N. C. *Journal of Magnetic Resonance* **2002**, *154*, 28-45.

(11) Levitt, M. *Spin Dynamics*; John Wiley and Sons, Ltd.: New York, 2001; pp. 513-570.

(12) Bakhmutov, V. I. *Practical NMR Relaxation for Chemists*; John Wiley & Sons, Ltd: Chichester, UK, 2004.

(13) Levy, G.; Peat, I. *Journal of Magnetic Resonance* **1975**, *18*, 500-521.

(14) Schaefer, J.; Sefcik, M. D.; Stejskal, E. O.; McKay, R. A. *Macromolecules* **1981**, *14*, 188-192.

(15) Stejskal, E. O.; Schaefer, J.; Sefcik, M. D.; McKay, R. A. *Macromolecules* **1981**, *14*, 275-279.

(16) Schaefer, J.; Stejskal, E. O.; Buchdahl, R. *Macromolecules* **1975**, *8*, 291-296.

(17) Burns, S.; Wu, X.; Zilm, K. *Journal of Magnetic Resonance* **2000**, *143*, 352-9.

(18) Wu, X. *Journal of Magnetic Resonance, Series A* **1993**, *102*, 205-213.

(19) Wu, X.; Zilm, K. W. *Journal of Magnetic Resonance, Series A* **1993**, *102*, 205-213.

(20) Wu, X.; Burns, S. T.; Zilm, K. W. *Journal of Magnetic Resonance, Series A* **1994**, *111*, 29-36.

(21) Bennett, A. E.; Rienstra, C. M.; Auger, M.; Lakshmi, K. V.; Griffin, R. G. *The Journal of Chemical Physics* **1995**, *103*, 6951.

(22) Schmidt-Rohr, K.; Spiess, H. W. *Multidimensional Solid-State NMR of Polymers*; Academic Press Inc.: San Diego, 1994; pp. 402-438.

Chapter 3: Unique Probe Design

3.1 Introduction

Two basic probe designs are available for low temperature NMR experiments:[1–5] transmission line and tank circuit probes. There are considerations of low temperature experiments that are important in the design of these probes, such as radio frequency (rf) transfer efficiency, circuit design, and cooling efficiency. This chapter will address the two low temperature NMR probe designs and the advantages and disadvantages of each. The design that has been chosen, the reasons for the implementation, and experimental evidence for the improved performance will be given. Then some conclusions as to the quality of the probe will be drawn.

Transmission Line Probes

Several different types of transmission line probes are used for low temperature NMR[2, 5] experiments. The simplest design is a coil attached to a length of transmission line, made from coaxial cable. The transmission line has a large amount of stored energy along the length of the line and not in the coil; this stored energy is due to the standing wave present along the line, which is the reflected current (or voltage) when the characteristic impedance, Z_o, is different than the load[5]. The characteristic impedance (units of ohms) of the line is defined as

$$Z_o = \frac{60}{\sqrt{\epsilon}} \ln\left(\frac{a}{b}\right) \qquad (1)$$

where ϵ is the relative dielectric constant, and a and b are the outer and inner diameters of the conductors. This difference (mismatch) in impedance between the load and the line is referred to as the standing wave ratio[6] (SWR), which is measured by the ratio of the maximum to minimum value of current (or voltage) of the standing wave that is present[5]. In experiments

where a large magnetic field is necessary, having a standing wave, which accounts for some loss in the system, is detrimental.

Another disadvantage of the use of transmission line probes is that the power efficiency ($P(x)$) is affected by the length of the transmission line[3] as shown in equation 2:

$$P(x) = P_0 \exp(-2\alpha x) \quad (2)$$

where x is the transmission line length (in m) and α is the attenuation constant (m^{-1}). As the length of the line increases, the power decreases exponentially, weighted by the attenuation constant, which is intrinsic to the type of conduction material used, dielectric material, radio frequency, and inner/outer conductor diameters[7]. A more efficient transmission line design was developed by McKay and Schaefer, which used a larger coaxial line that allows for a much smaller loss in the line and consequently a smaller α[8]. Transmission line probes based on McKay's design are made of copper pipes of large diameters which are used to transmit the rf to the coil with air as the dielectric. A larger diameter results in smaller attenuations. One disadvantage of using the McKay transmission line design for low temperature experiments is that copper is a good thermal conductor, 400 W/mK (at room temperature)[9], and so will act as a large heat sink. The larger diameter copper pipes also take up a large volume in the cryostat, taking longer to cool down.

One advantage of the transmission line design is the ability to move capacitors away from the coil such that they are placed outside of the magnet. This arrangement leads to more room in the sample space of the probe[10,11] and easier implementation of multiple rf channels. Having the capacitive elements in the cryostat limits the space available for multiple frequencies. One draw-back to such remote tuning is that there is higher voltage (or current) along the line once the probe has been tuned and matched. One probe for OPNMR (optically

pumped NMR) in our lab was based on the transmission line design. The design has a length of cable connected to the end of the copper pipe (which is attached to the coil) that changes the effective length. A remotely located tuning box at the end of the cable allows for the correct resonance frequencies to be reached. Depending on the resonance frequency, the point at which the cable attaches to the pipe may have very high voltage (or current) across it (based on the standing wave). Only cables and connectors that can handle extremely high voltages should be used, which limits the versatility of the design.

Tank Circuit Probes

The tank circuit design in which the tuning elements are located near the coil avoids the losses associated with the standing wave ratio in transmission line probe designs. The power loss is negligible since there is not as long a line length as in transmission lines (which can be on the order of meters) depending on the frequency. There can be a much larger B_1 field (induced magnetic field) and with less loss of power if the capacitive elements are located near the coil. The tank circuit design will only have a large voltage near the coil, since it is locally tuned, without having a large SWR along the entire length. The tuning can be adjusted over a wide range of rf with the tank circuit design; all that is needed is a different capacitance. Having the ability to adjust frequency more easily and having large magnetic fields at the coil make the tank circuit design an attractive alternative to transmission line probes, as will be shown. The materials used in the design can also be tailored to more thermally suitable materials at low temperatures, because better electrical conduction is not needed along the entire length.

3.2 Probe Design

A single channel tank circuit probe was constructed for low temperature, tunable frequency, static NMR. The probe was designed as a simple tank circuit to fit in a Janis cryostat for low temperature experiments. The blank stainless steel flange, that is part of a Kwik flange fitting used to seal the cryostat when not in use, is the top of the probe. The blank flange was modified by adding a 316L stainless (nonmagnetic) steel[9] support rod (not shown in Figure 3.1) and two Swagelok Ultra-Torr vacuum fittings as shown in Figure 3.1 in grey. One Ultra-Torr fitting was used for sealing the tuning rod (316 stainless steel rod with a copper top and bottom), which is attached to the top of the capacitor that is located at the sample space. The copper at the bottom of the tuning rod is used for better connectivity to the capacitor whose top is brass, with a thermal expansion coefficient of 18.7ppm/K[12], which is similar to the thermal constant for copper (16.5 ppm/K[12]) making it less likely to loosen at cold temperatures. There are also set screws for attaching the tuning rod to the top of the capacitor. The other Ultra-Torr fitting is to seal the second rod (see Figure 3.1), which is used for support. Copper, which is usually used in many probe designs is a good thermal conductor as stated earlier, and therefore becomes a large heat "fin". Stainless steel is a poor thermal conductor (16W/mK at RT)[9] and will require less helium to cool down; it should also provide better thermal isolation and prevent condensation of water for the portions of the probe that are outside the cryostat. There is also a cryogenically sealed BNC bulk head adaptor from Amphenol® RF on the blank flange which is used to transmit the radio frequencies to the coil for excitation. The radio frequencies were transmitted to the coil through RG-58A/U cabling from

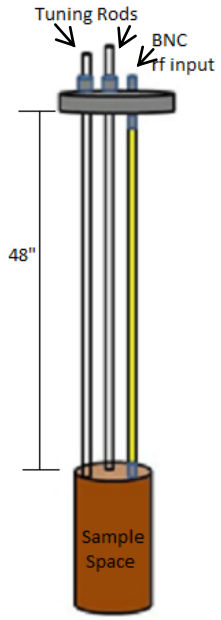

Figure 3.1: Diagram of Tank circuit probe design

Belden Inc. This cabling was made to fit loosely so that when the temperature decreases the cabling does not break from thermal shrinkage. The sample space of the probe is made out of copper. The length of the probe was optimized so that the coil would hit the center of the magnetic field of the 4.7T magnet when placed into the cryostat.

Circuit Design

In our probe, the tank circuit used is parallel-tuned[13]. There are several important components of the circuit: a frequency source (in this case our radio frequency of interest), two capacitors (one for tuning and one for matching the inductance), and a coil. These parallel-tuned circuits have a variable tuning capacitor (and in this probe a fixed capacitor across the coil) which adjusts the resonance frequency to the frequency of interest for the nucleus. The match capacitor is used to match the impedance to 50Ω. The circuit for this probe has a fixed match that uses a tap on the coil instead of a second variable capacitor. The tap removes some of the capacitive elements from the circuit[2]. The tapped tank circuit probe electronic diagram is shown in Figure 3.2.

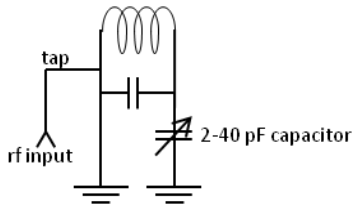

Figure 3.2: Circuit diagram for probe design

Tuning Capacitor

The tuning capacitor is the variable capacitor plus the fixed capacitor across the coil, which is in parallel. The fixed capacitor can be changed to allow for different frequency ranges depending on the capacitance value as shown in Table 3.1. The variable capacitor is a low temperature open ended sapphire trimmer capacitor from Voltronics (NMP40MEK) which suffers from some performance problems at low temperature. The problem is that the

capacitor, because it is open ended, freezes at liquid helium temperatures; it also has a working voltage of only 500V. A better capacitor would be a quartz capacitor (higher working voltage: 1 kV) that is built for low temperatures without an open end. One consideration in the choice of capacitor is the dielectric present, which could contribute to background signal depending on the nuclei of interest in the experiments. A quartz dielectric would be undesirable for ^{29}Si NMR experiments, since quartz is silicon dioxide. The sapphire dielectric cannot be used if ^{27}Al is being studied, since sapphire is composed of aluminum (III) oxide.

The fixed capacitor (Panansonic ceramic disc capacitor rated for 500V) is changed based on the resonance frequency of the specific nucleus of interest at a given field strength. Table 3.1 shows the possible radio frequencies that the probe can tune to and the necessary fixed capacitors for specific frequencies at liquid nitrogen temperatures. The capacitors used for the experiments were 82pF for ^{69}Ga, 47pF for ^{71}Ga, and 127pF for ^{29}Si. The probe is built such that only adjusting the fixed capacitor is needed to change to the frequencies of interest on a 4.7T or 7T magnet as shown in the last column of Table 3.1.

Table 3.1: Range of radio frequencies available from fixed capacitors: low and high frequencies are established by the variable capacitor (2- 40 pF) at 77K.

Fixed Capacitance (pF)	**Low Frequency** (MHz)	**High Frequency** (MHz)	**Isotope of Interest**
0	78.450	309.80	
18	65.250	107.30	^{71}Ga (7T)
27	62.250	89.250	
39	56.612	75.450	^{69}Ga (7T)
47	53.775	69.162	^{71}Ga (4.7T) ^{29}Si (7T)
68	47.293	56.450	
82	47.162	55.850	^{69}Ga (4.7T)
101	42.481	48.150	
127	39.625	42.425	
150	36.762	40.056	^{29}Si (4.7T)

Match Capacitor

The match capacitor is used to match an impedance of 50 Ω. This impedance value is chosen due to the fact that most amplifiers and cables are set to 50 Ω impedance in NMR applications, which when matched limits the amount of reflection. A tapped match is used in this circuit design, which is made by soldering a piece of wire (a "tap") to the coil and modifying the inductance along the lead length of the coil as shown in Figure 3.2, this is known as an inductive coupling design[2,14,15].

The tapping point on the coil was set by using an rf sweeper from Morris Instruments Inc. (model number 405NV+) to monitor the frequency and to help optimize the match. The Morris instrument is a continuous wave rf generator. When the resonance condition is met with the circuit, a dip at the resonance frequency is seen. The depth of the dip gives the proximity to 50 Ω impedance; if the dip hits the bottom of the scale on the Morris instrument screen it is matched. Optimization for low temperatures was done by submerging the sample space into liquid nitrogen (77 K) and adjusting the position of the tapping point so that it was matched better at low temperatures. The optimization of the position of the tapping point is done at an intermediate temperature (77K) because the match does not change much as the temperature is lowered further to 6K.

Coil Design

The solenoid coil is made from 4 turns of 16 gauge tinned copper wire with a gap of 4.16 mm for light to impinge on the sample, an inner diameter of 6.25mm, and length of 13.50mm for a total volume of 0.4142cm^3. The inductance of the coil, L, which is fixed based on the number of turns and the diameter of the coil, is at a specific resonance frequency (ω_0) when in series with a capacitor[13],

$$\omega_0 = \frac{1}{\sqrt{LC}}. \quad (3)$$

The inductance of the coil is 116nH, based on measurements of frequency at a specific capacitance (2pF).

3.3 Results and Discussion

NMR experiments were performed on a 4.7 T magnet on both the single channel transmission line probe currently being used for OPNMR and the tank circuit probe for comparison. Standard experiments were performed on 1.0 M aqueous gallium (III) nitrate solutions for ^{69}Ga (48.09 MHz) and ^{71}Ga (61.10 MHz) and TMS (tetramethyl silane) neat liquid for ^{29}Si (39.73 MHz).

Bloch decay (single pulse), and nutation experiments were done for several different nuclei to show the versatility of the new probe design, as well as to test the probe performance with specific focus on ^{69}Ga, ^{71}Ga, and ^{29}Si isotopes. These nuclei are of interest to another part of our lab studying OPNMR in semiconductors. ^{29}Si experiments could not be performed on the transmission line probe because the high voltage MHV connector needed was not available for the probe. To be able to compare the efficiency of each probe for each isotope, the spectrometer and amplifier were set so that the power into the probes for every frequency would be equivalent. The field strength, as determined from the measurement of the 360° "pulse" for each probe, is shown in Table 3.2. The pulse length[6,16] relates to the field strength, B_1 field, through equation 4:

$$B_1(kHz) = \frac{1}{360°(s)} * 10^{-4}. \quad (4)$$

Table 3.2: Comparison of B_1 efficiency and Q factor for transmission line and tank circuit probe at 4.7T.

Isotope	**Frequency** (MHz)	**Transmission line B_1 field strength** (kHz)	**Q factor for transmission line**	**Tank circuit B_1 field strength** (kHz)	**Q factor for tank circuit probe**
^{69}Ga	48.09	19.2	73.98	52.6	202.05
^{71}Ga	61.10	29.4	81.47	71.4	256.72
^{29}Si	39.73	N/A	N/A	55.5	218.29

As can be seen from the results in Table 3.2, the tank circuit probe produces a larger rf field for all nuclei at the same incident power. Nutation experiments[16] were also performed for each probe design as shown in Figure 3.3. Comparisons of the two probes based on nutation experiments for the different frequencies are shown for ^{69}Ga (3.3a) and ^{71}Ga (3.3b). Nutation

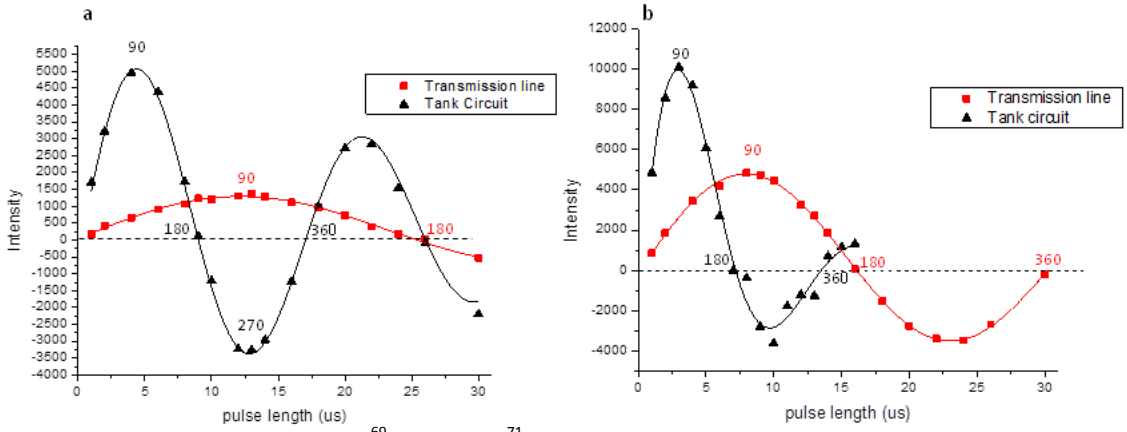

Figure 3.3: Nutation curves for a) is ^{69}Ga and b) is ^{71}Ga, ■ is the transmission line probe and ▲ is the tank circuit probe. Lines are a guide for the eye to see inversion.

curves give a measure of the B_1 field, based on the length of a 360° pulse. The comparison of the nutation curves can be seen in Figure 3.3 a) and b) for each probe. As is easily seen, the B_1 fields are larger (shorter 360° time) for the tank circuit probe for all frequencies; values are given in Table 3.2. The peak intensities are also substantially larger for the tank circuit probe.

Another aspect of the probes that can be determined from the nutation curve is rf inhomogeneity: based on the rate of decay of the sinusoid, the faster the decay, the larger the inhomogeneity. The rf inhomogeneity is larger for the tank circuit probe, as can be seen from the substantial decay of the signal in Figure 3.3b of the ^{71}Ga isotope than in the transmission line

probe, which could be due to the coil. This inhomogeneity is easily modified by using a different style of coil, such as the Helmholtz coil in the transmission line probe, which has a better homogeneity as seen in Figure 3.3. The differences in fixed capacitors could also be the reason that the curve decays more quickly in the tank circuit for ^{71}Ga than for ^{69}Ga.

One other consideration in development of the probe is the Q factor[17] (quality factor) of the probes. Measuring the Q allows a direct comparison of the probes with one another. There are certain drawbacks to having a high- or low-Q probe. The higher Q probes have a longer ring-down time, the time it takes the coil to disperse its stored energy which causes ringing in the coil. Conversely, the lower the Q factor, the shorter the ring-down time, but the magnetic field produced (H_1), which is proportional to B_1, will be smaller for a given power, as shown from the following equation from Fukushima:[13]

$$H_1 \cong 3\left(\frac{PQ}{V\nu_0}\right)^{½} \tag{5}$$

where P is power in Watts, Q is the quality factor, V is the volume of the coil in cm^3, and ν_0 is the resonance frequency in MHz. The Q of the probe can be measured using the rf sweeper (for details see Section 3.2). The Q factor of a resonant circuit probe can be determined using the bandwidth[17], or full width half maximum (FWHM), of the dip on the sweeper as seen in equation 6:

$$Q = \frac{f_0}{FWHM}. \tag{6}$$

As shown in Table 3.2, the Q and the B_1 field correlate with one another. In the case of the transmission line probe, when the power is kept the same, a larger B_1 field is produced for the ^{71}Ga nucleus than ^{69}Ga due to the higher Q factor. In comparing the Q of the tank circuit probe to that of the transmission line probe, the tank circuit probe has a higher Q at all frequencies. In

OPNMR experiments, where large B_1 fields are necessary, the higher Q probe, the tank circuit probe, is a better-performing probe.

3.4 Conclusions

A single channel tank circuit probe has been designed for low temperature NMR experiments. This probe has the versatility of being able to adjust the frequency simply by changing a fixed capacitor in the probe, giving it more broadband capability. When compared to the transmission line probe that is currently being used by the group to do OPNMR, the tank circuit probe has a higher Q and produces a larger B_1 field more efficiently. In other words, lower power is needed to the get B_1 fields that are necessary for efficient excitation in the experiments. Also because of the smaller thermal mass of the probe, the system can be cooled down faster (18 minutes versus 1 hour). Several parts of the probe could be improved further to increase the efficiency of the probe such as: a new tuning capacitor that works at low temperatures with a higher voltage rating and a more homogeneous coil similar to the one currently on the transmission line probe. All of these together determine that the tank circuit probe is a better design for these experiments than the transmission line probe that is currently being used.

3.5 References

(1) Damyanovich, A. Z.; Peternelj, J.; Pintar, M. M. *Journal of Magnetic Resonance* **2000**, *144*, 1-5.

(2) Conradi, M. S. *Concepts in Magnetic Resonance* **1993**, *5*, 243-262.

(3) Kim, Y.W. Earl, W.L., Norberg, R. E. *Journal of Magnetic Resonance* **1995**, *116*, 139-144.

(4) Kuhns, P. L.; Lee, S.-H.; Coretsopoulos, C.; Hammel, P. C.; Gonen, O.; Waugh, J. S. *Review of Scientific Instruments* **1991**, *62*, 2159.

(5) Traficante, D. D. *Concepts in Magnetic Resonance* **1993**, *5*, 57-86.

(6) Stringer, J. A.; Drobny, G. P. *Review of Scientific Instruments* **1998**, *69*, 3384.

(7) MacLaughlin, D. E. *Review of Scientific Instruments* **1989**, *60*, 3242- 3248.

(8) Schaefer, J.; McKay, R. A. Multi-Tuned Single Coil Transmission Line Probe for NMR Spectrometer **1999**.

(9) Doty, F. D.; Entzminger, G.; Yang, Y. A. *Concepts in Magnetic Resonance* **1998**, *10*, 133-156.

(10) Rath, A. R. *Magnetic Resonance in Medicine* **1990**, *13*, 370-7.

(11) Walton, J. *Journal of Magnetic Resonance* **1989**, *81*, 623-627.

(12) In *ASM Ready Reference:Thermal Properties of Metals*; Cverna, F., Ed.; ASM International: Materials Park, OH, 2002; pp. 9-13.

(13) Fukushima, E.; Roeder, S. B. W. *Experimental Pulse NMR A nuts and Bolts Approach*; Westview Press, 1981; p. 1-?

(14) Traficante, D. D. *Concepts in Magnetic Resonance* **1989**, *1*, 73-92.

(15) Kuhns, P. L.; Lizak, M. J.; Lee, S.-H. *Journal of Magnetic Resonance* **1988**, *76*, 69-76.

(16) Keifer, P. A. *Concepts in Magnetic Resonance* **1999**, *11*, 165-180.

(17) Helfrick, A. D. In *Electrical Measurement, signal processing and Displays*; Webster, J. G., Ed.; CRC Press: Boca Raton, FL, 2004; Vol. 32, pp. 16-1-7.

Chapter 4: Photoreaction of Single Crystals

4.1 Introduction

The photoreaction of α-*trans*-cinnamic acid has been studied for many years. The original studies were performed by Cohen and Schmidt in the 1960's in which different derivatives of cinnamic acid were systematically studied and in the end the topochemical postulate was developed[1]. Their observations that "1) chemically closely related compounds show significant differences in chemical behavior in the solid state; 2) a given compound reacts differently in the solid and dispersed phases; and 3) polymorphic modifications of a given compound show significant differences in chemical behavior"[1] lead to the topochemical postulate which states that limited movement in the solid state is needed for reactivity. Distance constraints of ~4.2 Å and parallel double bonds were necessary for reactivity. The constraints can be seen in Figure 4.1 for cinnamic acid. The yellow bonds denote the photoreactive species and the product formed. The double headed arrows show the distance between the vinyl bonds, note the overlap of the two vinyl bonds in yellow.

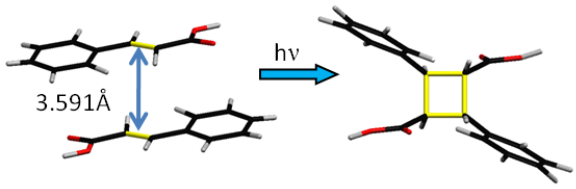

Figure 4.1: Photoreaction of α-*trans*-cinnamic acid forming α-truxillic acid.

Other labs have studied cinnamate photoreactions extensively using several different methods. Single crystal X-ray crystallography was one of the first techniques used for analysis of the cinnamic acid photoreaction[2–4]. The single-crystal-to-single-crystal reaction of cinnamic acid using "tail" irradiation was discovered by Enkelmann[2]. Other labs have since used X-ray crystallography, coupled with laser irradiation, to observe a 2-photon dimerization[5]. Previous

studies have been performed by our collaborators on β-cinnamic acid and substituted cinnamates[6–8] using solid state NMR. There has also been research in our lab on broadband and "tail" irradiations of cinnamic acid powders[9,10]. Presented here is the first time single crystal NMR of photoreacted cinnamic acid has been performed, which could give insights into how the single-crystal-to-single-crystal transformation occurs.

In single crystal NMR, rotation experiments map out the chemical shift anisotropy (CSA) of the two component species. Figure 4.2 shows the ^{13}C static NMR powder patterns for the vinyl carbon of cinnamic acid (left) and the cyclobutane carbon of truxillic acid (right). Due to

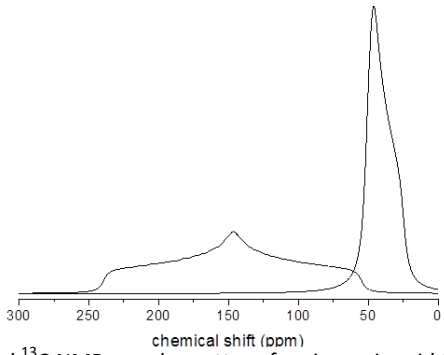

Figure 4.2: Simulated ^{13}C NMR powder pattern for cinnamic acid (left) and truxillic acid (right).

differences in the anisotropies, the pattern for cinnamic acid is broader than the pattern for the truxillic acid. This is the spectrum that would be observed in a static NMR experiment of a powder of partially reacted material. In single crystal experiments, as the crystal is rotated, the chemical shift values change due to the orientation difference of the unit cell, leading to a "mapping out" of the chemical shift anisotropy lineshape.

The unit cell for cinnamic acid is shown in Figure 4.3, which depicts the orientation of the molecules and the symmetry of the crystal structure. The cinnamic acid is isotopically labeled at the β position, the vinyl carbon next to the phenyl ring; only one carbon on each molecule is visible in the ^{13}C NMR spectrum. There are 4 molecules in the unit cell; molecules a)

and c) are related by inversion symmetry and are magnetically equivalent producing a single resonance in single crystal rotation experiments. Molecules b) and d) are also related by inversion symmetry and will produce a single resonance. Therefore, at most orientations of the crystal, 2 peaks will be observed, (at other orientations only a single resonance will appear with the two peaks overlapping.)

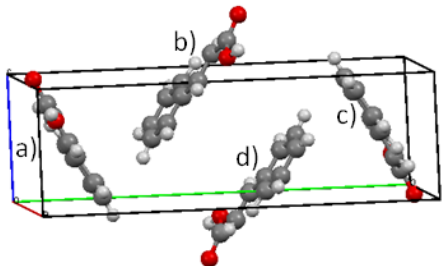

Figure 4.3: Unit cell for cinnamic acid: a) molecule 1, b) molecule 2, c) molecule 3, and d) molecule 4. Molecules a) 1 and c) 3 are related by symmetry and b) 2 and d) 4.

Cross polarization (CP) NMR spectra observing the photoreaction in the single crystal is shown in Figure 4.4, and was first observed after 15 hours of irradiation (4.4b). Unreacted peaks of cinnamic acid are given in Figure 4.4a (between 100-200ppm). After 30 hours, the truxillic acid peak can be easily resolved (between 0 and 60ppm). The difference in chemical shift

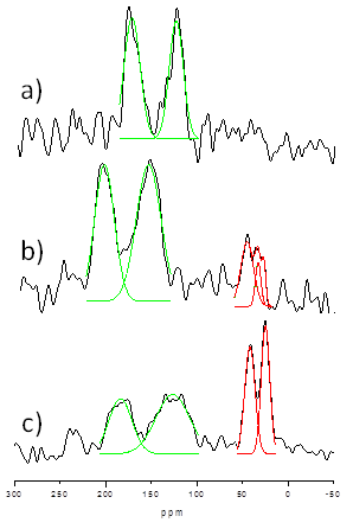

Figure 4.4: $^{13}C\{^{1}H\}$ CP of the single crystal photoreaction for a) unreacted, b) 15 hours, and c) 30 hours of irradiation at 54°. Green is cinnamic and red is truxillic (fit of data).

between 4.4a) and b) is due to the fact that sample had to be removed from the probe for irradiation, and therefore the orientation of the goniometer stage was not exactly the same every time. Note that the observed chemical shift for cinnamic acid does not change appreciably as the sample is irradiated. The intensity decreases and broadens for the cinnamic acid peaks (in green) but the chemical shift remains relatively the same, even with the product being present.

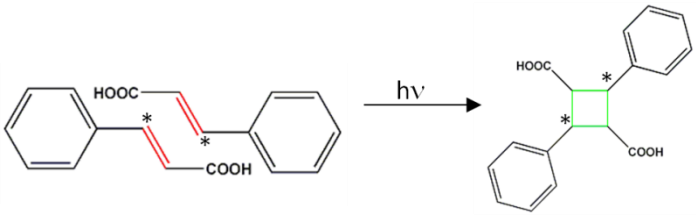

Scheme 4.1: Photoreaction of cinnamic acid forming truxillic acid product. * denotes isotopic label

As a reminder, see Scheme 4.1 for the photoreaction and the isotopic labels.

Truxillic acid as a product has several different possible crystal polymorph structures that can develop during the photoreaction. The possible crystal structures have been determined by several different groups using X-ray crystallography[4] as well as in our lab using solid state NMR in combination with wavelength-selective irradiation[10]. The crystal structure that develops initially in the photoreaction ($P2_1/n$) is meta-stable (seen in previous experiments

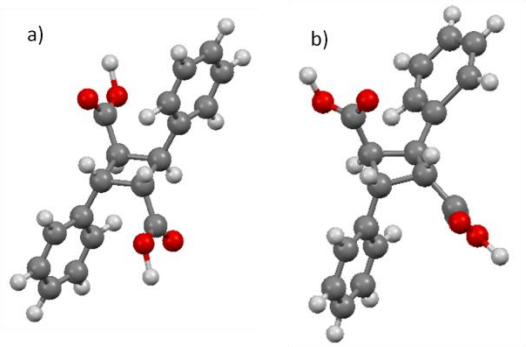

Figure 4.5: Crystal structures of truxillic acid a) $P2_1/n$ polymorph and b) C2/c polymorph.

by Nieuwendaal[11]) and eventually converts into the more stable polymorph (C2/c). Figure 4.5 shows the two different molecular structures that are found corresponding to the truxillic acid polymorphs. The cyclobutane ring of truxillic acid is flat in the $P2_1/n$ polymorph, where the C2/c

polymorph has a kinked ring. Another key difference between the polymorphs is the number of molecules in the unit cell. The $P2_1/n$ structure has 2 molecules in the unit cell, whereas C2/c has 4 molecules. Due to symmetry, the $P2_1/n$ crystal structure has 2 magnetically inequivalent β carbon sites, corresponding to 2 distinct resonances observed in the ^{13}C NMR spectrum (shown in the single crystal photoreaction spectra). The C2/c crystal structure with the kinked ring has inequivalent carbons adjacent to the phenyl moiety on the cyclobutane ring, as well as 2 magnetically inequivalent molecules in the unit cell, which would correspond to potentially 4 distinct resonances in single crystal NMR experiments. In the sequential irradiation of the single crystal in Figure 4.4, note that there are only two peaks in the cyclobutane region. This corresponds to the meta-stable $P2_1/n$ polymorph.

Irradiation of the single crystals was performed in the "tail" of the absorption band; it is reported that this tail irradiation allows the single crystals to undergo a single-crystal-to-single-crystal (SC-to-SC) transformation, which was originally observed by Enkelmann in single crystal X-ray diffraction experiments[2]. In the "tail", the light can penetrate somewhat evenly through the material, allowing for reaction of sites not just on the surface. When broadband irradiation (280nm-400 nm) is used, there is high absorption on the surface. The chemical shift tensor for $P2_1/n$ α- truxillic acid will be established in this chapter for the single-crystal-to-single-crystal photoreaction. This chapter will also elucidate the domain sizes of truxillic acid being produced in cinnamic acid single crystals after irradiation.

4.2 Experimental Methods

Synthesis and Irradiation of Crystals

^{13}C labeled single crystals of α-*trans*-cinnamic acid were synthesized[12] from a microwave synthesis of malonic acid and ^{13}C labeled benzaldehyde, thereby labeling the β vinyl position,

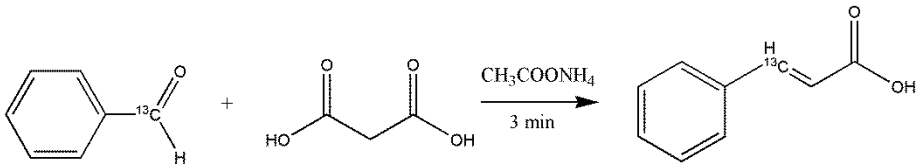

Scheme 4.1: Reaction scheme for synthesis of isotopically labeled cinnamic acid.

next to the phenyl ring, shown in Scheme 4.2. Purification was performed using sublimation. (Solution NMR data given in Appendix III) The isotopically labeled cinnamic acid was then recrystallized from diethyl ether into the α form (head-to-tail packing), resulting in large crystals (on the order of 1 cm long). A crystal was glued onto the goniometer using a low melting point halogenated wax (from Halocarbon). To re-orient the crystal, slight heating was used to remove and re-mount the crystal. Wavelength selective irradiations were performed using a 150 W Xe arc lamp from Thermo-Oriel (lamp from Ushio) with its output passed through a monochromator centered at 350 ± 10 nm. Irradiance was measured with a Scitech power meter to be 98 $\pm$8 μW/cm^2 for the 4.2 mm x 4.2mm x 0.2mm sample used in rotation experiments and 115$\pm$ 10μW/cm^2 for the 8.3 mm x 4.2 mm x 0.3mm sample used in NMR spin diffusion experiments. The samples were sequentially irradiated.

NMR Experiments

Single Crystal Rotations

^{13}C {^{1}H} Cross polarization (CP) echo[13] experiments with two pulse phase modulation (TPPM) decoupling[14] were performed with a 2-channel (^{1}H-^{13}C) transmission line goniometer probe based on the design by R.A. McKay and Jacob Schaefer[15], built by Ryan Nieuwendaal[11].

The experiments were recorded at ν_H=200.39MHz and ν_C=50.39 MHz with a Tecmag Apollo spectrometer. The Hartmann-Hahn match was set with adamantane, which served as a secondary reference to TMS at 0 ppm. Typical experimental conditions included: contact time of 5ms, 60 kHz power for CP, 80-100 kHz ^{1}H decoupling, dwell time of 10 µs, and an echo tau delay of 30 µs. Typical recycle delays were 20 minutes (T_1 of 5 minutes). Depending on the size of the crystal, different numbers of scans were recorded, not exceeding 256 transients. Step sizes were 12°/rotation.

Single Crystal Spin Diffusion

The spin diffusion experiments were performed based on an inversion recovery of the ^{1}H with indirect detection via the ^{13}C to allow for chemical shift resolution[16]. The pulse sequence is given in Figure 4.6. This experiment was performed on both an unreacted and a sequentially-reacted crystal.

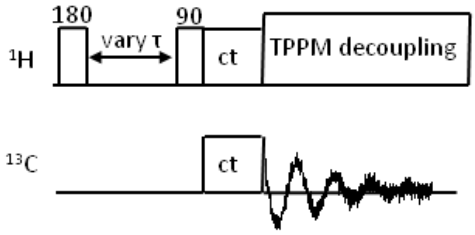

Figure 4.6: Pulse sequence for spin diffusion experiments.

Simulations

Calculations were used to determine the orientation of the chemical shift tensor for truxillic acid as well as the orientation of the unit cell of cinnamic acid within the single crystal based on the rotation experiments. *Ab initio* calculations of truxillic acid were performed using GAUSSIAN 03, 09[17], and SIMPSON and SIMMOL programs[18,19]. In all simulations, atomic positions were obtained from available X-ray crystal structures. Geometry optimizations were performed using density functional theory with B3LYP fuctional[20,21] and a 6-311++G basis set[22]. NMR

chemical shielding calculations used the GIAO method[23] with the B3LYP functional and 6-311G basis set to obtain the $\delta_{11,22,33}$ parameters for truxillic acid as input for SIMPSON and SIMMOL. Chemical shift referencing of GAUSSIAN was done with TMS (benzene as a secondary reference[24]) at the same levels of theory. SIMPSON and SIMMOL were used for simulation of rotation NMR spectra and truxillic acid tensor.

4.3 Results and Discussion

Previous experiments of unreacted cinnamic acid single crystal rotations performed by Ryan Nieuwendaal were used as the basis for this work on partially-photoreacted single crystals of cinnamic acid[11].

Chemical Shift Tensor of Truxillic Acid

The chemical shift tensor for truxillic acid was determined from rotation experiments of a partially-reacted single crystal. The orientation of the single crystal with respect to the goniometer and the unit cell are shown in Figure 4.7 a and b. The goniometer is denoted along the blue dotted arrows. The crystals were aligned macroscopically by eye such that they were approximately aligned with the goniometer. The top of the crystal is the [010] face (b axis of the unit cell) as determined from single crystal X-ray diffraction experiments. When the goniometer is oriented at 0°, the magnetic field (B_o) is parallel to the [010] face. The α' orientation was determined to be 43° off the x-axis of the unit cell, and β' is 130° off the x-axis of the unit cell (see Figure 4.7c). The unit cell x-z plane is oriented off diagonal from the rotation axis (as noted in Figure 4.7a and b) as well as the crystal. (Note: α' and β' orientations are named based on the original orientations of the unreacted cinnamic acid as defined in Ryan Nieuwendaal's thesis[11].)

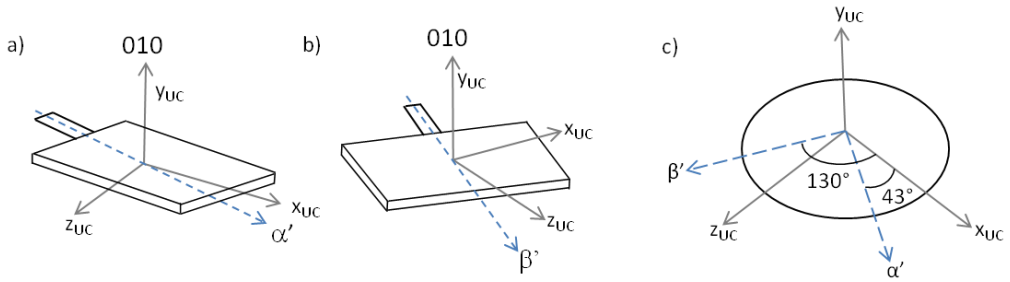

Figure 4.7: Definition of the orientation of the crystal rotations labeled a) α' and b) β' with respect to the crystal and the goniometer stage (black) c) the rotation angles in the unit cell.

The crystal was mounted in the β' orientation (12% truxillic acid), and rotations were performed,

(Figure 4.7b), then the crystal was irradiated and re-mounted in the α' position (4.7a) (26% truxillic).

The change of ^{13}C single crystal NMR chemical shifts for cinnamic acid with change in goniometer angle is shown in Figure 4.8. The red circles are chemical shifts from molecules 1 and 2 (based on simulations) and the black squares are molecules 2 and 4.

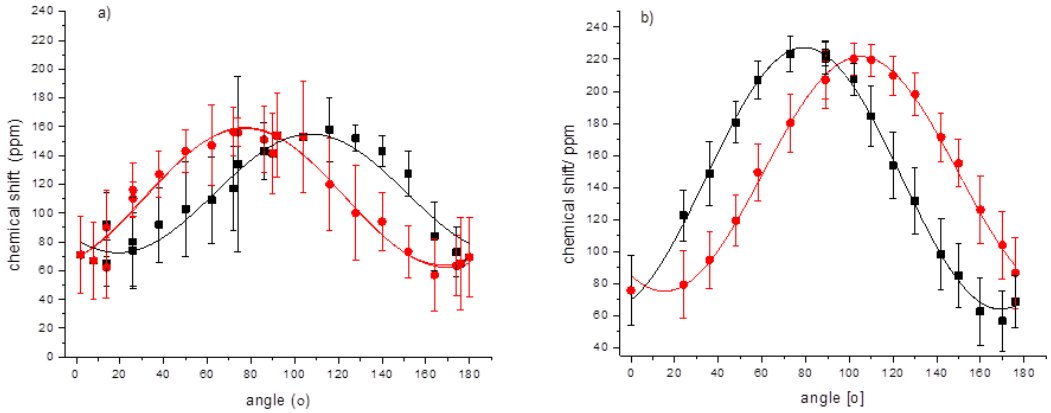

Figure 4.8: ^{13}C single crystal NMR rotation experiments of partially-reacted cinnamic acid about the a) α' orientation and b) β' orientation. Molecules 1 and 3 are denoted as ● and Molecules 2 and 4 are denoted as ■ (based on simulations).

Solid points are based on fits to Equation 1, a gaussian fit

$$\mathbf{y = y_0 + \frac{A}{w\sqrt{(\pi/2)}} * exp\left[-2 * \left(\frac{x - x_c}{w}\right)^2\right]} \quad (1)$$

where y_o is the offset, A is area, w is width, and x_c is the peak center. The data points are from the values of the peak center based on the fit. The error bars are based on the full width half maximum (FWHM) determined from the fit as well (parameter w). The error bars are larger on the α' rotations due to the broadening of the chemical shift from the photoreaction (longer irradiation to resolve the chemical shifts of truxillic acid). Linewidths will be addressed in the next section. The curves in Figure 4.8 for each set of molecules were fit to a sinusoidal function, Equation 2,

$$\mathbf{y = y_0 + A * sin\left[\pi \frac{(x - xc)}{w}\right]} \quad (2)$$

where y_o is the offset, A is the amplitude, x_c is the center of the curve, and w is the width.

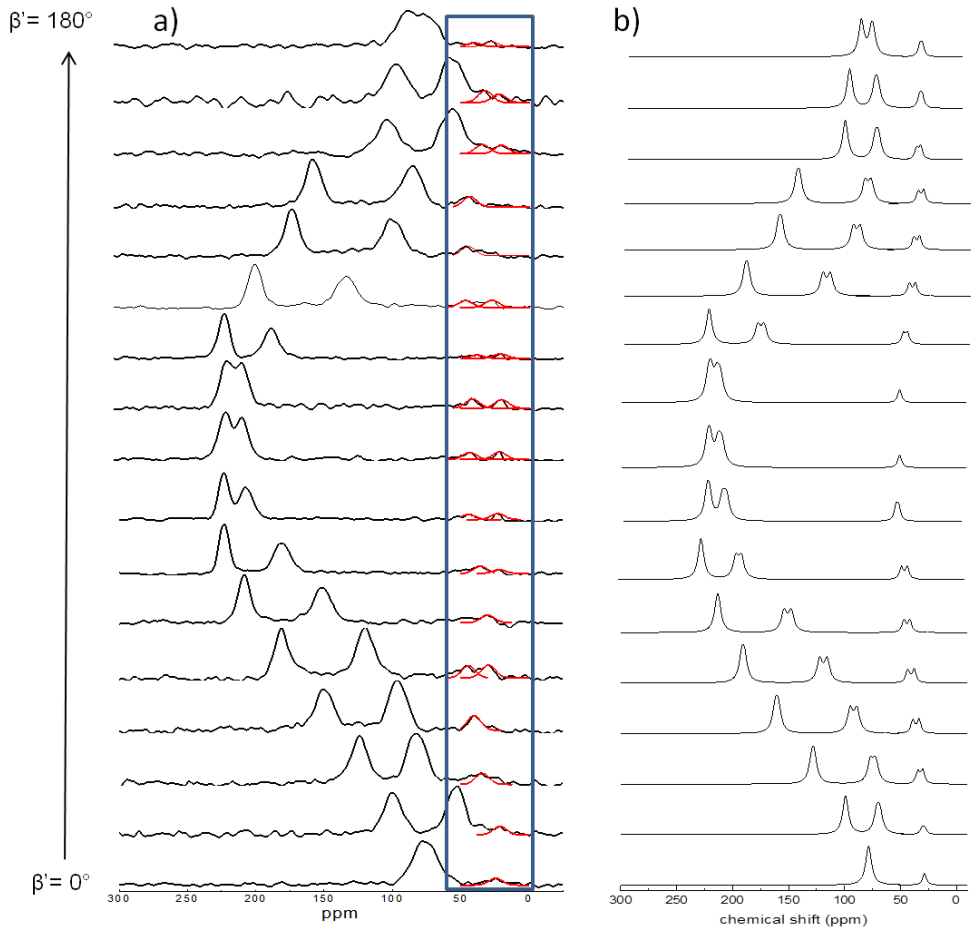

Figure 4.9: ^{13}C CP single crystal NMR rotation experiments for partially reacted crystals around β' a) are experimental and b) are simulations. Red lines and box used to emphasize truxillic acid rotations.

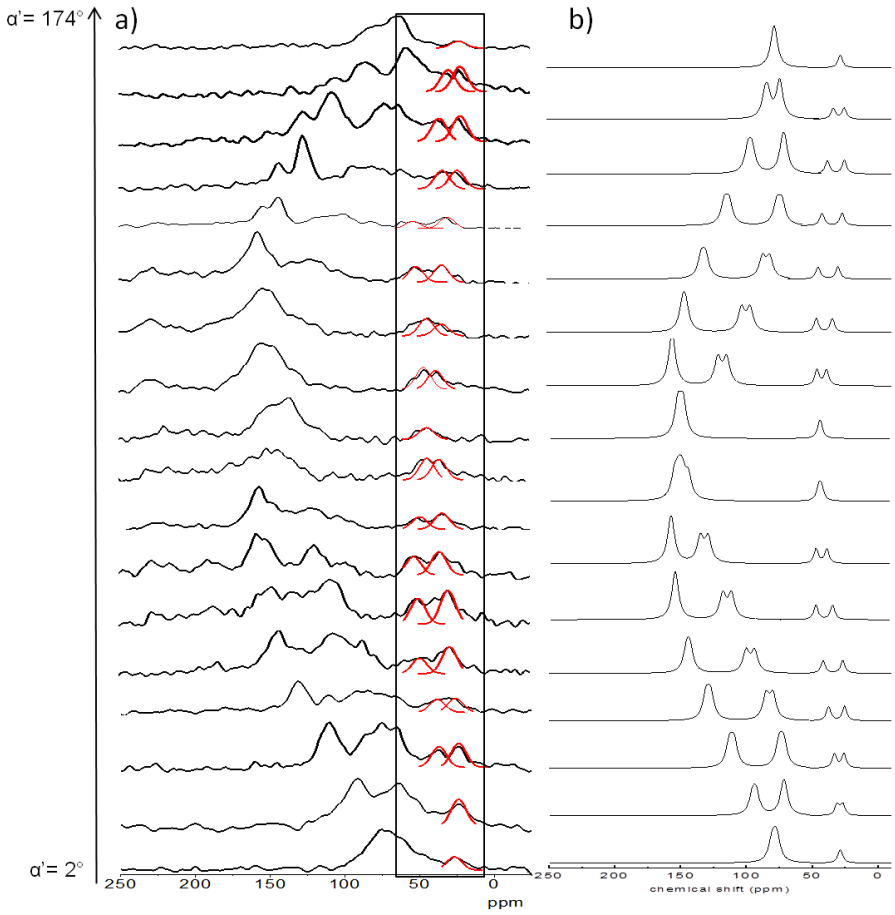

Figure 4.10: ^{13}C CP single crystal NMR stack plot for partially reacted crystals around α' a) are experimental and b) are simulations. Red lines and box used to emphasize truxillic acid rotations.

A stack plot of the rotation experiments and their corresponding simulations are given in Figures 4.9 and 4.10 for β' and α' rotations respectively. A box surrounds the truxillic acid rotations to emphasize these. The truxillic acid peaks are also outlined in red to show chemical shift changes with orientation. Due to the smaller anisotropy of the chemical shift for the truxillic acid peaks, it is more difficult to resolve the associated features. The difficulty in resolution is also due to the fact that the crystals are only partially reacted, such that the truxillic acid peak intensities are smaller than the cinnamic acid peak intensities. Simulations, generated in the program from SIMPSON, are used to match experimental data to theory, for both

cinnamic and truxillic acid and used to determine the orientation of the chemical shift tensor, are shown in Figures 4.9b and 4.10b for each set of rotations.

Rotation experiments of the partially reacted single crystals, and the knowledge that the cinnamic acid peaks largely do not change chemical shift during the photoreaction, (refer to Figure 4.4), means that there is limited movement of the cinnamic acid as the photoreaction occurs (see topochemical postulate). The knowledge that the cinnamic acid does not move appreciably and that limited movement is needed for reaction to occur suggests that the unit

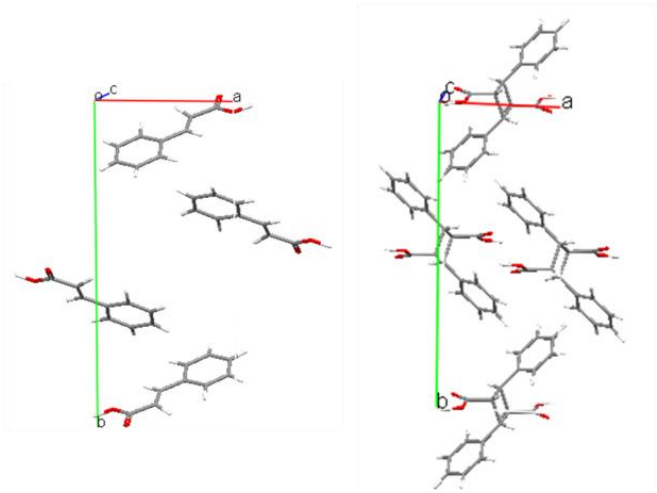

Figure 4.11: Unit cells of cinnamic acid and truxillic acid, showing the alignment of the b axis, or [010] face.

cell of truxillic acid will be aligned in the same direction as that of cinnamic acid, denoted in Figure 4.11. Note alignment of both b axes (green) in the same direction. The assumption can be made that cinnamic acid could be used to limit the orientation of the truxillic acid tensor by noting that the goniometer rotation angles with respect to the unit cell must be the same for both species.

From these assumptions and using the rotation experiments, the orientation and determination of the chemical shift tensor for truxillic acid was established. The tensor is shown in Figure 4.12b, colored purple. The greatest shielding component, σ_{zz} ($=\sigma_{TMS}-\delta_{zz}$) is oriented

parallel to the cyclobutane ring. The full tensor can be described by δ_{iso}= 40.5ppm, δ_{aniso}=−16ppm, and η= 0.3125 (defined in Chapter 2). The truxillic acid tensor is compared to the

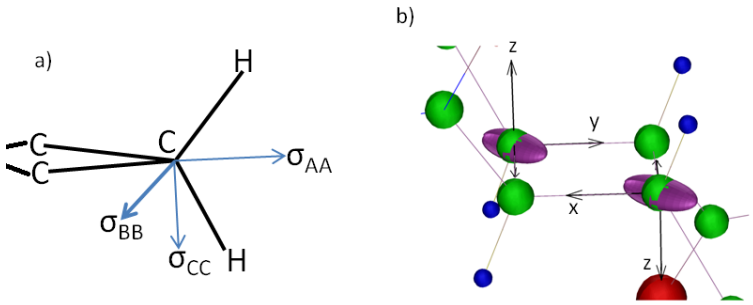

Figure 4.12: Chemical shift tensor assignment for a) cyclobutane (ref) and b) truxillic acid.

tensor assignment of cyclobutane, shown in Figure 4.12a as defined by Facelli et.al.[25] Note that the orientations of the two tensors are similar but not quite the same. This is due to the difference between the CH_2 group of cyclobutane and the CH group of the truxillic acid. The tensor is oriented with respect to the molecular frame (MF) which is shown as the black arrows around the cyclobutane. There are two tensors, related by inversion, present in the ring. The tensor values for the cyclobutane compared to the truxillic acid as well as the two polymorphs are given in Table 4.1. Note that there are two different tensors for the two different cyclobutane ring carbons (β position) for the C2/c polymorph (kinked ring), whereas the flat $P2_1/n$ species has a single site. For a more detailed description of tensors, see Chapter 2.

Table 4.1: Chemical shift tensor values for several cyclobutane rings.

Compound	**σ_{AA}** (ppm)	**σ_{BB}** (ppm)	**σ_{cc}** (ppm)	**δ_{iso}** (ppm)	**Haeberlen convention/ppm**		
					δ_{zz}	**δ_{xx}**	**δ_{yy}**
cyclobutane	23	14	39	25	39	14	23
truxillic acid ($P2_1/n$)	46.6	24.8	51.5	40.6	24.8	51.5	46.6
truxillic acid ($C2/c$)[7]	33.4 56.5	33.4 29.3	69.6 66.7	45 51	69.6 29.3	33.4 66.7	33.4 56.5

Signal Broadening from Dispersion[26]

In this section, the signal broadening effects observed in the cinnamic acid peaks will be addressed. In comparing the simulated ^{13}C NMR spectra and the experimentally determined spectra, a disparity in the linewidths has been observed. The simulated data is based on 4 molecules in the unit cell (which assumes a perfect crystal); the ^{13}C linewidths predicted from simulations are determined to be 6-10ppm. In the experimental data however, the linewidths are broader, on the order of 10- 39 ppm for α' and 10-22 ppm for β' (reminder: the α' rotations have been further reacted). In previous experiments with unreacted cinnamic acid, the observed linewidths of the ^{13}C NMR were between 6-18 ppm. There are several potential sources of broadening in static NMR experiments: ^{1}H-^{13}C heteronuclear dipolar, J-coupling, and ^{13}C-^{13}C homonuclear dipolar interactions (because these are isotopically labeled). Other effects such as bulk magnetic susceptibility anisotropy should be small (< 1ppm)[27], and the B_0 field has good homogeneity. The first two possible broadening sources (^{1}H-^{13}C dipolar and J-coupling) can be removed through heteronuclear decoupling which is used in the CP pulse sequence (B_1 ~100 kHz). Since the sample is isotopically labeled (~98%) the ^{13}C-^{13}C homonuclear dipolar coupling could be a substantial effect. The broadening based on dipolar coupling (proposed by VanVleck[28]) can be determined from the equation 3:

$$\langle \Delta \boldsymbol{\omega}^2 \rangle = \left(\frac{\mu_o}{4\pi}\right)^2 \frac{3}{4} \hbar^2 \gamma_I{}^4 \frac{I(I+1)}{N} \sum_k^N \sum_j \frac{(1-3\cos^2\theta_{jk})^2}{r_{jk}{}^6} \qquad (3)$$

where μ_0 is the permittivity of free space, $\hbar$ is Planck's constant divided by 2π, I is the nuclear spin quantum number (I=½), N is the number of inequivalent sites (4), θ_{jk} is the angle of intersect of internuclear sites (j and k) and the applied field, r_{jk} is the internuclear distance. The full width half maximum (FWHM) of the line is defined as Equation 4:

$$\Delta\boldsymbol{\omega_{1/2}} = \mathbf{2.35}\sqrt{\langle\Delta\boldsymbol{\omega}^{\mathbf{2}}\rangle} \quad (4)$$

where $\Delta\omega_{1/2}$ is the FWHM. Simulations of the homonuclear dipolar couplings range from 0.77 to 1.85ppm, contributing a small amount to the linewidth.

Table 4.2: Molecules #1 and #3 of cinnamic acid: observed chemical shifts versus goniometer orientation and linewidths.

Goniometer orientation: α'	**Chemical Shift: δ** (ppm)	**Linewidth: FWHM** (ppm)	**Crystalline Dispersion Coefficients**		
			Δδ/Δα deg/ppm	**Δδ/Δβ** deg/ppm	**Δδ/Δγ** deg/ppm
2	71	27	0.019	0.044	0.22
8	67	27	0.058	0.10	0.23
14	90	26	0.010	0.050	0.19
26	110	12	0.024	0.060	0.050
38	127	16	0.025	0.055	0.17
50	143	15	0.022	0.048	0.44
62	147	28	0.025	0.051	0.72
74	156	10	0.11	0.14	0.94
86	151	23	1.43	7.60	5.23
92	154	29	7.28E-5	0.020	1.09
104	153	39	0.016	0.0016	1.07
116	120	32	0.042	0.025	0.93
128	100	33	0.038	0.018	0.71
140	94	20	0.029	0.0059	0.43
152	73	18	0.021	0.0094	0.16
164	57	25	0.028	0.034	0.064
180	69	28	0.019	0.044	0.22

Molecules 2 & 4 and β' orientations (all molecules) given in Appendix II.

The extra linewidth could be attributed to some orientational disorder, due to crystalline imperfections[26] as well as broadening from the reaction. The crystalline dispersion effects can be quantified through simulating slight perturbations of the Euler angles (±1° increments). The change of chemical shift with Euler angle is defined as the crystalline dispersion coefficients (Table 4.2) for (Δδ/Δα,β,γ). The calculation for the effect of crystalline dispersion on linewidth can be calculated by Equation 5:

$$\boldsymbol{\Delta\omega_{CSD}} = \boldsymbol{\Delta\alpha}\left(\frac{\boldsymbol{\Delta\delta}}{\boldsymbol{\Delta\alpha}}\right) + \boldsymbol{\Delta\beta}\left(\frac{\boldsymbol{\Delta\delta}}{\boldsymbol{\Delta\beta}}\right) + \boldsymbol{\Delta\gamma}\left(\frac{\boldsymbol{\Delta\delta}}{\boldsymbol{\Delta\gamma}}\right) \quad (5)$$

With the total linewidth equation 6: $\boldsymbol{\Delta\omega_{1/2} = \Delta\omega_{DD} + \Delta\omega_{CSD}}$ (6)

where $\Delta\omega_{DD}$ refers to the homonuclear coupling linewidth[26]. $\Delta\alpha$, $\Delta\beta$, and $\Delta\gamma$ are the spreads in the orientation for each respective Euler angles and $\Delta\delta/\Delta\alpha,\beta,\gamma$ are the coefficients relating the chemical shift dispersion to orientational disorder. The broadening has increased in the α' rotations due to the increased photoreaction. The linewidths for the cinnamic acid peaks in the β' rotations are also broader than the unreacted cinnamic acid. The crystalline dispersion changes from $\{\Delta\alpha, \Delta\beta, \Delta\gamma\} = \{6.0, 7.9, 2.0\}$ for a crystal of unreacted cinnamic acid[26] to {9.8, -7.6, 16.2} for the reacted crystal. There is definite broadening in the crystals from the photoreaction, and an increase in the crystalline dispersion in the alpha and gamma angles.

Domain Size Experiments

The development and distribution of product in these single-crystal-to-single-crystal reactions has been established as occurring in two different ways in different materials. Both schemes are idealized cases. The first possible scheme is random nucleation and homogeneous growth, from the different nucleation sites, shown in the top of Scheme 4.3. The second scheme

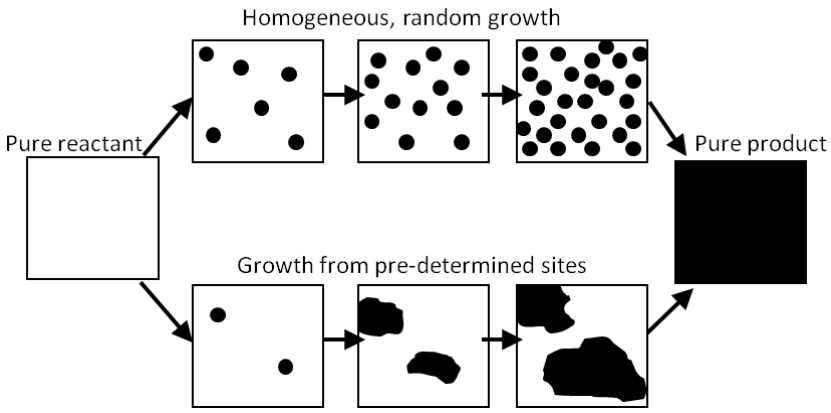

Scheme 4.2: Possible schemes for distribution of the photoproduct in the reactant matrix. The top is a homogeneous growth and the bottom is from pre-determined sites, like defects. White is reactant and black is product.

for development of product is nucleation at pre-determined sites, (bottom of Scheme 4.3) such as defects or lattice mismatches, then growth from those nucleation sites only. In spin diffusion experiments, the time scales for T_1 relaxation of each spin system will differ for these two schemes. In the bottom product development scheme, the spin diffusion behavior that would be seen (possibly bimodal), as compared to the top scheme, where the product is more intimately mixed. (For more information on spin diffusion see Chapter 2). It is possible that there might be a combination of the two schemes in a real system such as is currently being studied.

^{1}H inversion recovery experiments, remotely detected through ^{13}C, to measure the morphology of the crystal using spin diffusion were performed on a sequentially-irradiated single crystal. Figure 4.13c) shows the unreacted chemical shifts, 4.13a) has the longest irradiation time of 24 hours, and 4.13b) was irradiated for 14 hours. Note the decrease in

intensity of the cinnamic acid reactant peaks (~225ppm) and the increase of the cyclobutane signal (~40ppm) at longer irradiation times. The cinnamic acid peaks also broaden as the crystal

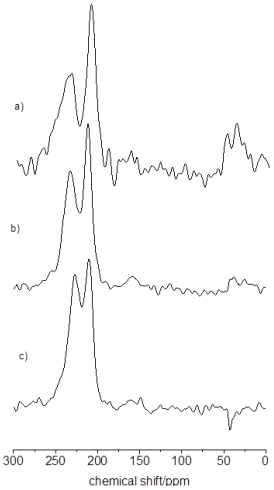

Figure 4.13: Sequential irradiation of single crystal a) 24 hours, b) 14 hours, and c) unreacted to measure spin diffusion and domain sizes.

is irradiated for longer times. One resonance (226ppm) seems to be more susceptible to the reaction than the other, as denoted by the larger amount of broadening.

Figure 4.14 shows the plots of peak intensity versus delay periods from inversion recovery for the unreacted crystal (in black), the 14 hour-irradiated (in red), and 24 hour-

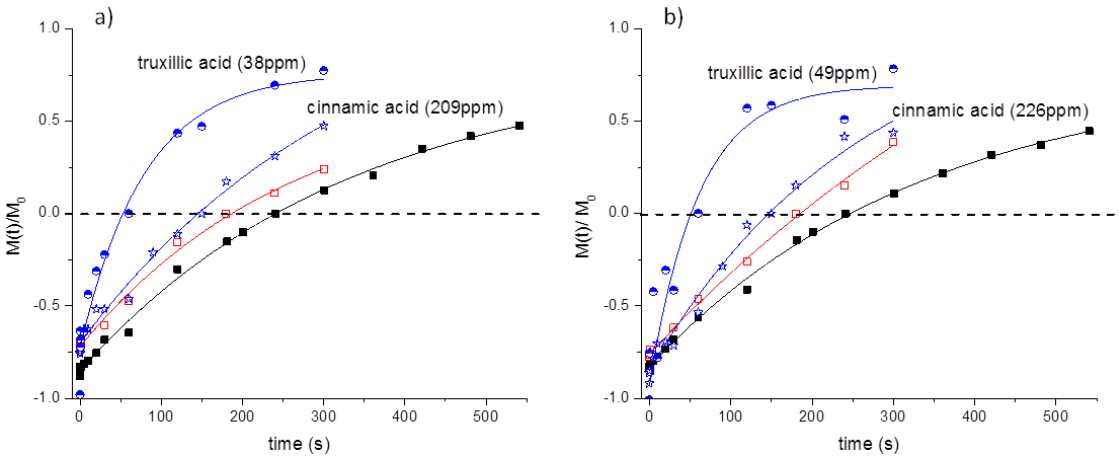

Figure 4.14: Inversion recovery experiments of a) 209ppm cinnamic acid peak, 38ppm truxillic acid and b) 226ppm cinnamic acid, 49ppm truxillic acid. Unreacted ■; 14 hours of irradiation □; and 24 hours of irradiation ★, ◓. Dashed lines denote null.

irradiated crystal (in blue). The dashed line is a guide to the eye. Figure 4.14a depicts the lower frequency cinnamic acid and truxillic acid resonance, and 4.14b depicts the higher frequency cinnamic acid and truxillic acid shifts. The unreacted sample (in black) has a 7-minute T_1 based on the measurements made. When the crystal has only been irradiated for 14 hours (red), the T_1 shortens to 5.5 minutes, even though the truxillic acid peak is not yet visible. The effect on the value for T_1 shows a change due to the presence of truxillic acid. The 24 hour irradiated crystal (blue) has visible truxillic acid peaks, and T_1 of the truxillic acid portion is measured to be 2 minutes.

Figure 4.15 depicts the semilog plot of the inversion recovery experiments. 4.15a is plotted the 209ppm cinnamic acid peak unreacted (in black) after 14 hours of irradiation (in red) and then after 24 hours irradiation (in blue) along with the truxillic acid 38ppm peak. Note the change in slope as the irradiation time increases for the cinnamic acid species. Also note that the truxillic acid species appears to have a bimodal T_1. In figure 4.15b is depicted the 226ppm shift for cinnamic acid and 49ppm shift of truxillic acid, showing similar behavior.

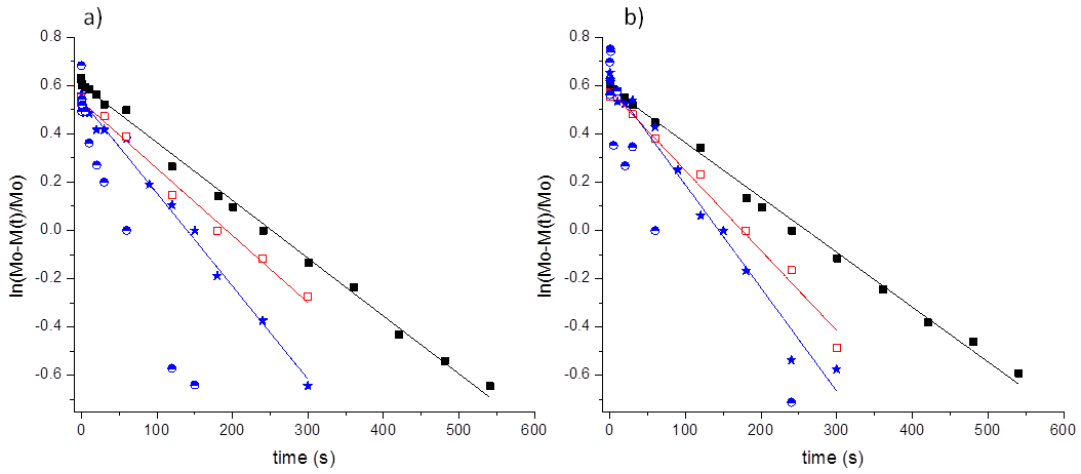

Figure 4.15: Semilog plots of inversion recovery of a) 209ppm cinnamic acid, 38ppm truxillic acid (◓) and b) 226ppm cinnamic acid, 49ppm truxillic acid (◓). Unreacted ■; 14 hours of irradiation □; and 24 hours of irradiation ★, ◓.

After disturbance of the magnetization using rf, the recovery of the magnetization along the z-axis can be described by the following equation[29]:

$$\boldsymbol{M(t) = M_0\left[(1-(1-cos\alpha)*exp\left(\frac{-t}{T_1}\right)\right]} \quad (7)$$

where M_0 is the equilibrium magnetization, α is equal to 180° for inversion-recovery, and T_1 is the spin lattice relaxation[30]. This was used as a fit for Figure 4.14 to determine T_1. The equation can be rearranged into the linear form[29]:

$$\boldsymbol{\ln\left(\frac{M_o - M(t)}{M_o}\right) = \ln(1-cos\alpha) - \frac{t}{T_1}} \quad (8)$$

Figure 4.15 shows the semilog plots for the unreacted and sequentially reacted sample, fit to equation 8. The domain sizes can be determined from the following equations: 9,10[31]

$$d = \frac{\varepsilon}{f_b}\sqrt{\left(\frac{4Dt_m}{\pi}\right)} \quad (9)$$

$$f_b = 1 - f_a \quad (10)$$

where d is the domain size, ε is the dimensionality, D is the diffusion coefficient, t_m is the time in which it takes the signal to null (see dotted line in Figure 4.14), and f_b and f_a are the respective fractions of each species. D can have a range of values, depending on the material, between about 0.8 nm^2/ms and 0.1 nm^2/ms.[32] Materials such as crystalline polyethylene have a diffusion coefficient of 0.6 nm^2/ms, which is the value used for the calculations of the domain size[32].The value of ε is equal to 1, 2, or 3 depending on the dimensionality[31]. In this case, ε is assumed to be 1. Using the t_m value of 60 seconds for the truxillic acid species, an estimate of the domain size of the truxillic acid-rich region at 24 hours of irradiation is 214 nm. Table 4.3 summarizes all of the experimentally determined T_1 values for each irradiation time and chemical shift as well as the null time (t_m). The decrease of the T_1 after irradiation for 14 hours suggests a solid

Table 4.3: Values for T_1 and spin diffusion time for the different species present at specific irradiation times.

Irradiation time	Chemical shift (ppm)	T_1 (min)	t_m (sec)
Unreacted cinnamic acid	209	6.7	241
	226	7.1	
14 hour irradiation cinnamic acid	209	5.8	180
	226	5.2	
24 hour irradiation cinnamic acid	209	4.4	150
	226	3.9	
24 hour irradiation truxillic acid	38	1.6	60
	50	1.9	

solution of truxillic acid present in the cinnamic acid crystal initially. After 24 hours of irradiation, the truxillic acid peaks are visible in the NMR spectrum. Benedict and Coppen[5] determined that even at 355nm (the irradiation wavelength used in their experiments) a high absorption on the surface was observed in cinnamic acid single crystals. Based on this, it could be assumed that the surface has a higher concentration of truxillic acid than the interior of the crystal. The truxillic acid –rich areas are also large enough that there is a distinct T_1 for the truxillic acid. There is still some mixing of the truxillic acid and cinnamic acid as there are small truxillic acid regions within the cinnamic acid-rich area. The mixing is indicated by the decrease in the T_1 with the increased irradiation time. The bimodal T_1 of truxillic acid also suggests that there are multiple truxillic acid areas: such as a truxillic acid-rich region and a cinnamic acid-rich region. The differentiation of truxillic acid-rich and cinnamic acid-rich portions of the crystal were also seen by Benedict and Coppen[5].

4.4 Conclusions

The photoreaction of cinnamic acid can be observed using single crystal NMR spectroscopy. The product that develops in the crystal during the photoreaction is the meta-stable $P2_1/n$ polymorph of the product. It is observed at a longer irradiation time than previously observed[10]. In previous experiments, when irradiation was performed at the maximum

wavelength the C2/c polymorph was the only product observed[9]. When "tail" irradiations are used, the meta-stable $P2_1/n$ polymorph is formed up to a certain point. Also, based on rotation experiments and simulations of product and reactants, the tensor for the $P2_1/n$ polymorph of truxillic acid has been determined. Previous experiments for determination of tensor values for truxillic acid using 2D PASS experiments produced tensor values for the C2/c polymorph only[7].

There is a linewidth in the photoreacted crystals that is greater than the simulated linewidths for cinnamic acid; while there is some broadening expected due to ^{13}C-^{13}C homonuclear dipolar coupling, this effect does not account for all of the linewidth. The rest of the residual linewidth can be explained by crystalline dispersion, due to imperfect crystals, as well as increased dispersion due to the photoreaction. This dispersion can be accounted for through a dispersion equation. The compositional heterogeneity for these photoreacted crystals can also be measured, and a mechanism for the development of product in the crystal has been determined. The truxillic acid-rich portion, after 24 hours of irradiation, has been determined to be 214 nm. Based on the size scale and the understanding that absorption is higher on the surface, the crystal appears to have a compositional gradient along the depth of the crystal in which the top has truxillic acid-rich domains and the bottom has cinnamic acid-rich domains.

4.5 References

(1) Cohen, M. D.; Schmidt, G. M. *Journal of the Chemical Society* **1964**, *June*, 1996-2000.

(2) Enkelmann, V.; Wegner, G.; Novak, K.; Wagener, K. B. *Journal of the American Chemical Society* **1993**, *115*, 10390-10391.

(3) Enkelmann, V. *Molecular Crystals and Liquid Crystals Science and Technology. Section A.* **1998**, *313*, 15-23.

(4) Abdelmoty, I.; Bucholz, V.; Guo, C.; Kowitz, K.; Enkelmann, V.; Wegner, G.; Foxman, B. M. *Crystal Growth & Design* **2005**, *5*, 2210-2217.

(5) Benedict, J. B.; Coppens, P. *The Journal of Physical Chemistry A* **2009**, *113*, 3116-20.

(6) Fonseca, I.; Hayes, S. E.; Blümich, B.; Bertmer, M. *Physical Chemistry Chemical Physics* **2008**, *10*, 5898-907.

(7) Fonseca, I. On the way to molecular optical switches : A solid-state NMR study of trans-cinnamic acids, Universitat Aachen, 2008, pp. 1- 154.

(8) Fonseca, I.; Hayes, S. E.; Bertmer, M. *Physical Chemistry Chemical Physics* **2009**, *11*, 10211-8.

(9) Bertmer, M.; Nieuwendaal, R. C.; Barnes, A. B.; Hayes, S. E. *Journal of Physical Chemistry B* **2006**, *110*, 6270-6273.

(10) Nieuwendaal, R. C.; Bertmer, M.; Hayes, S. E. *The Journal of Physical Chemistry B* **2008**, *112*, 12920-6.

(11) Nieuwendaal, R. C. The Topochemical [2+2] photocycloaddition reaction of alpha-trans-cinnamic acid: a perspective from solid-state NMR measurements, Washington University in St. Louis, 2008, pp. 1- 143.

(12) Ma, G.; Hayes, S. E. *Journal of Labelled Compounds and Radiopharmaceuticals* **2004**, *47*, 895-901.

(13) Earl, W. L. *Society* **1979**, 762-767.

(14) Bennett, A. E.; Rienstra, C. M.; Auger, M.; Lakshmi, K. V.; Griffin, R. G. *The Journal of Chemical Physics* **1995**, *103*, 6951.

(15) Schaefer, J.; McKay, R. A. Multi-Tuned Single Coil Transmission Line Probe for NMR Spectrometer **1999**.

(16) Takegoshi, K.; Nakamura, S.; Terao, T. *Solid State Nuclear Magnetic Resonance* **1998**, *11*, 189-96.

(17) Frisch, M. J.; Trucks, G. W.; Schlegel, H. B.; Scuseria, G. E.; Robb, M. A.; Cheeseman, J. R.; Scalmani, G.; Barone, V.; Mennucci, B.; Petersson, G. A.; Nakatsuji, H.; Caricato, M.; Li, X.; Hratchian, H. P.; Izmaylov, A. F.; Bloino, J.; Zheng, G.; Sonnenberg, J. L.; Hada, M.; Ehara, M.; Toyota, K.; Fukuda, R.; Hasegawa, J.; Ishida, M.; Nakajima, T.; Honda, Y.; Kitao, O.; Nakai, H.; Vreven, T.; Montgomery, Jr., J. A.; Peralta, J. E.; Ogliaro, F.; Bearpark, M.; Heyd, J. J.; Brothers, E.; Kudin, K. N.; Staroverov, V. N.; Kobayashi, R.; Normand, J.; Raghavachari, K.; Rendell, A.; Burant, J. C.; Iyengar, S. S.; Tomasi, J.; Cossi, M.; Rega, N.; Millam, N. J.; Klene, M.; Knox, J. E.; Cross, J. B.; Bakken, V.; Adamo, C.; Jaramillo, J.; Gomperts, R.; Stratmann, R. E.; Yazyev, O.; ; Austin, A. J.; Cammi, R.; Pomelli, C.; Ochterski, J. W.; Martin, R. L.; Morokuma, K.; Zakrzewski, V. G.; Voth, G. A.; Salvador, P.; Dannenberg, J. J.; Dapprich, S.; Daniels, A. D.; Farkas, Ö.; Foresman, J. B.; Ortiz, J. V.; Cioslowski, J.; Fox, D. J. Gaussian09 (Revision A.02) Gaussian Inc., Wallingford, CT, **2009**.

(18) Bak, M.; Rasmussen, J. T.; Nielsen, N. C. *Journal of Magnetic Resonance* **2000**, *147*, 296-330.

(19) Bak, M.; Schultz, R.; Vosegaard, T.; Nielsen, N. C. *Journal of Magnetic Resonance* **2002**, *154*, 28-45.

(20) Becke, A. D. *Journal of Chemical Physics* **1993**, *98*, 5648-52.

(21) Lee, C.; Yang, W.; Parr, R. G. *Physical Review B* **1988**, *37*, 785-89.

(22) Krishnan, R.; Binkley, J. S.; Seeger, R.; Pople, J. A. *Journal of Chemical Physics* **1980**, *72*, 650.

(23) Wolinski, K.; Hilton, J. F.; Pulay, P. *Journal of the American Chemical Society* **1990**, *112*, 8251-60.

(24) Komin, S.; Gossens, C.; Tavernelli, I.; Rothlisberger, U.; Sebastiani, D. *Journal of Physical Chemistry B* **2007**, *111*, 5225-5232.

(25) Facelli, J. C.; Orendt, A. M.; Beeler, A. J.; Solum, M. S.; Depke, G.; Malsch, K. D.; Downing, J. W.; Murthy, P.; Grant, D. M.; Michl, J. *Journal of the American Chemical Society* **1985**, *107*, 6749-6754.

(26) Nieuwendaal, R. C.; Mattler, S. J.; Bertmer, M.; Hayes, S. E. *The Journal of Physical Chemistry B* **2011**, *115*, 5785-93.

(27) Vanderhart, D.; Earl, W.; Garroway, A *Journal of Magnetic Resonance* **1981**, *44*, 361-401.

(28) van Vleck, J. H. *Physical Review* **1948**, *74*, 1168-1183.

(29) Gerhards, R.; Dietrich, W. *Journal of Magnetic Resonance* **1976**, *23*, 21-29.

(30) Levy, G.; Peat, I. *Journal of Magnetic Resonance* **1975**, *18*, 500-521.

(31) Schmidt-Rohr, K.; Spiess, H. W. *Multidimensional Solid-State NMR of Polymers*; Academic Press Inc.: San Diego, 1994; pp. 402-438.

(32) VanderHart, D. L.; McFadden, G. B. *Solid State Nuclear Magnetic Resonance* **1996**, *7*, 45-66.

Chapter 5: Wavelength Selective Photoreaction of Bipyridyl Ethylene-Co-Resorcinol

5.1 Introduction

There has been an interest recently in being able to control the chemistry and reactivity of solid state systems. The reason for the attention is the ability of solids to form stereo-selective products with high percent yields. Recognition of specific repeat units in the solid state, called synthons, can be used in the formation of new materials. Synthons are "structural units within molecules which can be formed and/or assembled by known or conceivable synthetic operations" (as defined by E.J. Corey)[1]. In solids, synthons are based on hydrogen

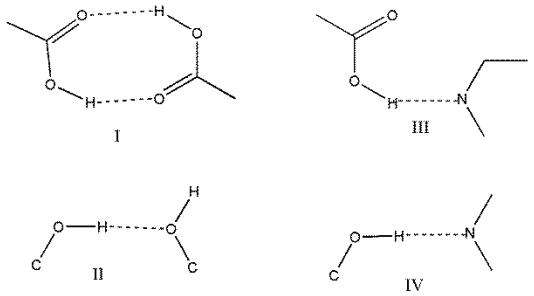

Figure 5.1: Examples of synthons that can be used to manipulate systems in the solid-state.

bonding systems[2]. Figure 5.1 shows several examples of hydrogen bonded systems that could be used to manipulate solids into confirmations that allow reactions to occur. In Figure 5.1- I and II are homosynthons, III and IV are heterosynthons. One example of a heterosynthon forming a

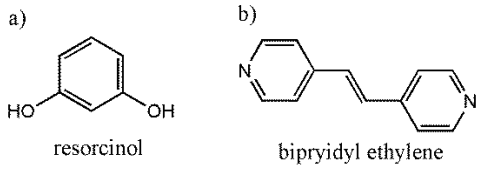

Figure 5.2: Structures used in the formation of co-crystal: a) resorcinol and b) bipyridyl ethylene.

reactive material is the 2(4, 4'-bipyridyl ethylene)·2(resorcinol) co-crystal denoted **bpe·res**.

Bipyridyl ethylene (bpe) on its own is photoinert, but when co-crystallized together with

resorcinol (res), it becomes photoreactive. Bpe·res co-crystals were provided by Prof. Leonard R. MacGillivray at the University of Iowa. The starting materials 1, 3-dihydroxy benzene and *trans*-1, 2-bis-(4-pyridyl) ethylene are given in Figure 5.2 a and b. This co-crystallization uses hydrogen bonding between the nitrogen on the pyridine ring and the hydroxides on the resorcinol to orient the bipyridyl ethylene, placing it parallel to the other vinyl bond and within 4.2Å. As you

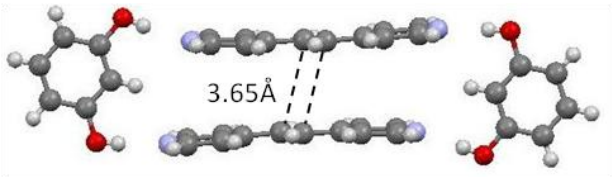

Figure 5.3: Orientation of bpe·res co-crystal in the solid-state; nitrogen is in blue, oxygen red, carbon gray, and hydrogen white.

can see in Figure 5.3, the resorcinol restricts the structure of the bipyridyl ethylene, which provides the appropriate orientation for photoreactivity. The photoreaction in these materials under broadband irradiation has been observed by several groups[3,4].

Scheme 5.1 shows the photoreaction of the reactant complex, bpe·res, forming the product, *rctt*-(tetrakis(4-pyridyl)cyclobutane)* 2(resorcinol), (hereafter known as "tpcb·res")[5]. The hydrogen bonding (dotted lines) between the alcohols on the resorcinol and the nitrogen on the pyridine rings orients the bipyridyl ethylene in such a way that it becomes photoreactive (note: bipyridyl ethylene crystallized alone is photoinert). When irradiated with ultraviolet (UV)

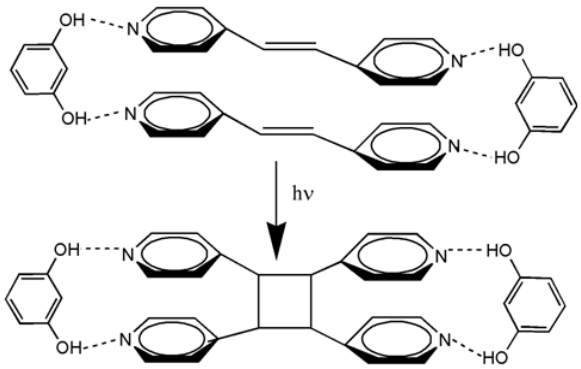

Scheme 5.1: A schematic representation of the [2+2] photocycloaddition of bpe·res co-crystal forming tpcb·res in the solid state.

light, a [2+2] photocycloaddition occurs. In this work, we demonstrate the effects of irradiation wavelength on product formation.

The effect of different wavelengths of light on this photoreaction is important in the development and understanding of these materials. Figure 5.4 shows absorption spectra for the individual components (5.4a, b) as well as the absorption spectrum for the complex (5.4c).

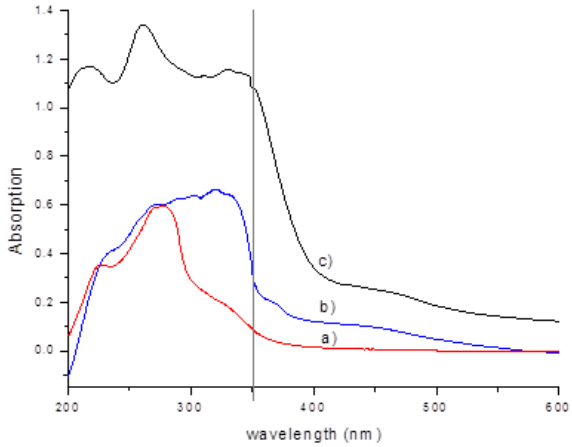

Figure 5.4: Absorption spectra for a) resorcinol (red) b) bipyridyl ethylene (blue), and c) the bpe·res co-crystal (black). The solid line indicates the irradiation wavelength tested.

Wavelength-selective irradiations were performed at multiple photon energies along the absorption band. The lowest photon energy, (longest wavelength) at which the photoreaction was observed was at λ=350 nm (solid gray line in Figure 5.4). Other wavelengths > 350 nm showed no sign of photoreaction after 24 hours of irradiation. The wavelength chosen (350 nm) is absorbed more strongly by bipyridyl ethylene (5.4b) with a smaller absorptivity for the resorcinol component (5.4a). We will demonstrate that irradiation at 350 nm produces the $P2_1/n$ product selectively, which is the thermodynamically stable product[6].

There have been several examples of single-crystal-to-single-crystal (SC-to-SC) photoreactions of materials under wavelength selective irradiations—such as *trans*-cinnamic acid, see chapter 3. The bpe·res system is of interest because under wavelength selective

irradiations the photoreaction does not occur as a SC-to-SC photoreaction. The original studies of these materials[3,7] were performed using single-crystal X-ray diffraction (XRD). Past a certain point in these experiments, the samples could no longer be analyzed using single-crystal XRD because the crystal broke apart as the photoreaction progressed. The reason that the crystals do not remain intact is due to the drastic change in the angle α of the unit cell (14° difference for a 14% reacted crystal) as the photoreaction occurs[7]. This change in angle, along with a shear that occurs along the cleavage plane, allows for easy degradation of the crystals, even in the tail of the absorption band[7]. The first wavelength that was successful in producing a photoreaction in which the crystals remained intact was at 385 nm (from experiments by Khan et.al.). The powdering of the samples could also be due to mechanical stress that is induced as the photoreaction progresses[8]. Solid-state NMR is perfect for analysis of these types of materials. As will be shown, it can be used to analyze the wavelength selective photoreaction and the kinetics at 350 nm. Monitoring the photoreaction via solid state NMR, coupled with powder XRD and simulations will be used to determine structural information.

5.2 Experimental Methods

Sample Preparation and Irradiation

The 2(4,4-bipyridyl ethylene)*2(resorcinol) co-crystals were synthesized through a recrystallization of bipyridyl ethylene and resorcinol in an ethanol/ acetonitrile (1:1) solution to form the co-crystal [3] (hereafter "bpe·res"). Crystals were generally less than 1mm in diameter and were separated by a sieve. The resulting crystallites were irradiated by placing onto a glass plate (~ 60 mg sample) and spread evenly to match the diameter of the arc lamp beam. Irradiations were performed with a 150W Xe arc lamp passed through a monochromator

centered at λ=350 ±10 nm (slit width of 3.16mm). The irradiance of the light averaged 122 ± 9 $\mu W/cm^2$ measured using a Scientech power meter. Individual samples were irradiated for different lengths of time, instead of a single sample sequentially irradiated and analyzed in between. UV-visible spectroscopy experiments were performed on a Varian Carey 100 double beam spectrometer.

NMR Experiments

Solid state NMR experiments were performed on the materials using 4mm and 5mm Varian/ Chemagnetics triple resonance HXY probes. The experiments were recorded at ν_C=74.17 MHz and ν_H=294.97 MHz with a Tecmag Apollo spectrometer, using ^{13}C cross polarization magic angle spinning (CPMAS) with two pulse phase modulation (TPPM) decoupling. The Hartmann-Hahn match was set with adamantane, which served as a secondary reference for tetramethylsilane (TMS) at 0 ppm. Typical experimental conditions were 2.3 μs ^1H π/2 pulses, 3 ms contact time, MAS rotational frequency of 6kHz, a 10 μs dwell time, and recording 600- 1000 transients. The recycle delay was changed for the photoreacted species, since the T_1 relaxation of the material shortened as the photoreaction progressed from 17 minutes to 4 minutes. The samples were limited to a rotation frequency of 6 kHz for MAS to avoid excessive heating, and to avoid physical stress on the crystallites. Previous experiments had shown a broadening of the NMR resonances when higher spinning speeds (10 kHz or greater) were used (data not shown).

Powder X-ray Diffraction Experiments

Powder X-ray diffraction (pXRD) experiments were performed on the 90-hour photoreacted sample and an unreacted sample, collected using a Rigaku Geigerflex D-MAX/A diffractometer using Cu-Kα-1 (λ = 1.54059Å) radiation. The software program Jade was used for processing to remove the background and the Kα-2 peaks.

Simulations

Ab initio calculations were performed on the anticipated product structures ($P2_1/n$ and P-1). Full geometry optimization was performed in Gaussian09 [9] using density functional theory with the B3LYP functional [10,11] and the 6-311++G basis set [12]. NMR shielding calculations were performed using the gauge-independent atomic orbital (GIAO) method [13] with the same functional and basis set. In all simulations, atomic positions were obtained from available X-ray crystal structures[3,7]. The P-1 crystal structure was modified from a partially-reacted structure, as no 100% as-dimerized (P-1) product structure is available. Chemical shift referencing of the calculations was based on TMS and benzene (C_6H_6) as a secondary reference[14] at the same levels of theory based on Equation 1:

$$\delta^{TMS}(x) = \sigma_{calc}(C_6H_6) - \sigma_{calc}(x) + \delta_{exp}^{TMS}(C_6H_6), \quad (1)$$

where x is the species of interest, and $\delta_{exp}^{TMS}(C_6H_6)$ =128.5ppm.

5.3 Results and Discussion

Wavelength Dependent Kinetics

Solid-state NMR experiments were used to monitor the progression of the photoreaction. Figure 5.5 shows representative ^{13}C CPMAS spectra of the photoreaction as it

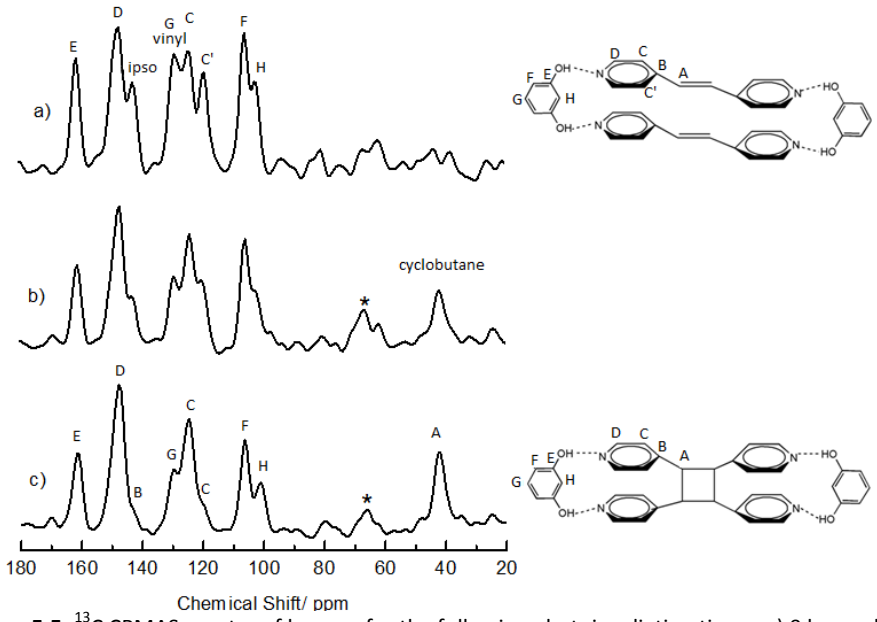

Figure 5.5: ^{13}C CPMAS spectra of bpe·res for the following photoirradiation times: a) 0 hours, b) 30 hours, and c) 90 hours. Letters are peak assignments for the given monomer (top) and dimer (bottom). (*denotes spinning sidebands)

progresses. The structures of the monomer and dimer are shown and the spectra are labeled with the associated chemical shift assignments. In Figure 5.5a the ^{13}C spectrum for the unreacted co-crystal is shown with the associated peak assignments. Several resonances are affected during the photoreaction due to the conversion of the neighboring sp^2 carbon into a sp^3 moiety. The vinyl signal, which is at 128 ppm, overlaps with another carbon (129 ppm) located on the resorcinol (site G). As the photoreaction progresses the intensity decreases in that region due to the disappearance of the vinyl carbons, the residual signal at 90 hours is attributed to the resorcinol. As the sample is irradiated, the cyclobutane signal appears at ~40 ppm, observed in

the 30 hour irradiation (Figure 5.5b) as a single resonance. After 90 hours (Figure 5.5c) a single peak is still observed and has increased intensity concomitant with the product formation. The ipso carbon, (noted in Figure 5.5a, carbon B) on the pyridine ring directly bonded to the vinyllic species, has shifted to higher frequency. There is also a shift of the ortho-carbons on the pyridine ring at 120ppm (carbon C'). When unreacted, these pyridine ring carbons are inequivalent, but as the photoreaction progresses, the structure becomes more symmetric and the resonances begin to overlap.

We have used the quantitative nature of NMR to measure the kinetics of this photoreaction by monitoring the build-up of the ^{13}C cyclobutane signal as a function of time. Figure 5.6 is the kinetics curve for the wavelength-selective photoreaction at λ=350 nm. The fraction of cyclobutane is expressed as a fraction of the total area of all protonated peaks that

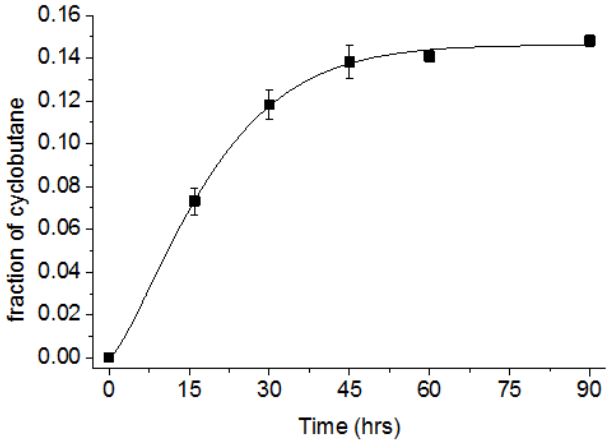

Figure 5.6: Photodimerization kinetics of bpe·res converting into tpcb·res (expressed in terms of the fraction of cyclobutane per total protonated carbons). The curve is a fit to a JMAK model with K=0.0165 ± 0.005 hr^{-1} and n=1.35 ± 0.09.

are recorded, so that signal: noise variations are accounted for between different experiments. This fractional area is determined from the area of the peak fit of a Gaussian to the cyclobutane resonance divided by the total area of the protonated carbons (also fit to Gaussian peaks). Here we use the ratio of cyclobutane over the area of all protonated carbons (in order to avoid major

differences in cross-polarization dynamics (variation in the build-up rates) for the non-protonated carbons as compared to the protonated ones). The kinetics were fit to a model based on the Johnson-Mehl-Avrami-Kolmogorov (JMAK)[15–19] nucleation and growth kinetics:

$$X(t)= a[1- exp(-Kt^n)] \quad (2)$$

where $X(t)$ is the fraction of product formed at time t, n is the Avrami exponent, K is the growth rate constant, and a is the asymptotic limit for the growth. The a parameter is needed since the fraction of product is based on cyclobutane versus total protonated carbons (instead of the product versus reactant as is normally done) due to the lack of spectral resolution of the reactant carbons. The asymptotic limit should be near 0.143 if the reaction has gone to completion based on the estimate of the number of carbons: 4 cyclobutane carbons versus 28 total protonated carbons (=0.143). The asymptotic limit based on the fit is 0.146 ± 0.002, which shows good agreement. The growth rate constant for the λ=350 nm irradiation is K= 0.017 ± 0.005 hrs^{-1} and the Avrami exponent is n= 1.35 ± 0.09.

The Avrami exponent (n) provides information about the dimensionality of nucleation and growth of the product. According to Avrami, random distributions of "germ" nuclei are present in the sample that transform into "growth" nuclei as the reaction progresses[15]. There is an associated probability of the germ nuclei transforming into growth nuclei per unit time. This probability is reflected in the value of the exponent. If the probability is small, n=4 for a 3-D (spherical) nucleation and growth, if the probability is large, then n=3. This assumption also similarly affects the 2-D (disk) and 1-D (rod) values of the exponent, n=3-2 and n=2-1 respectively [15–21]. Based on the Avrami exponent observed for the bpe·res system (n=1.35), a 1-D linear nucleation and growth occurs. The deviation from integer values is due to a departure from infinite and homogeneous nucleation and growth (such as a finite sample size and/or

inhomogeneous distribution of nuclei), which decreases the Avrami exponent[22,23]. This effect has also been observed in other systems using techniques such as solid-state NMR[20,24,25], X-ray diffraction[21,26,27], and Infrared (IR) spectroscopy[28,29].

Formation of Products

Using the NMR spectra in conjunction with modeling, we have confirmed the structure of the product. Possible crystal polymorphs (shown in Figure 5.7) have been determined via two

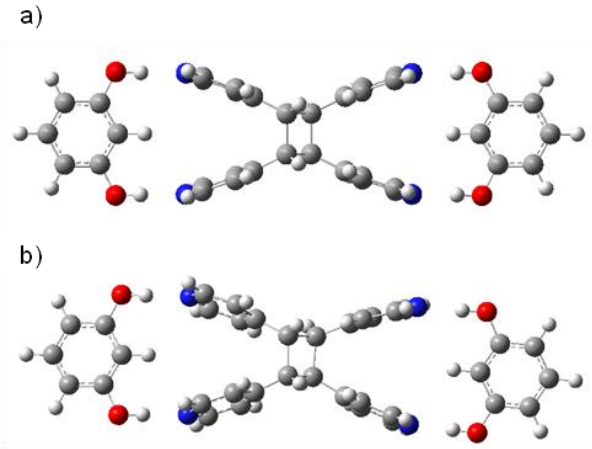

Figure 5.7: Possible crystal structures for tpcb·res product: a) the monoclinic $P2_1/n$ space group[3] and b) the triclinic P-1 space group[7].

routes. Dissolution and recrystallization of a fully-converted sample of tpcb·res forms a monoclinic $P2_1/n$ species[3] (5.7a). The triclinic P-1 polymorph (5.7b) has been reported for a partially photo-reacted (42%) as-dimerized sample (not recrystallized)[7]. Since the 100% P-1 structure has not been solved explicitly based on XRD, the atomic positions of the product are taken from the partially-reacted crystal structure. (In Figure 5.7b the reactant portion of the structure has been removed for clarity.) The symmetry of the pendant species distributed around the cyclobutane ring leads to distinct differences between the two structures. In the $P2_1/n$ polymorph, the pyridine rings are symmetric about the cyclobutane due to a center of inversion. This arrangement would lead to a single peak in the cyclobutane region of the ^{13}C

NMR spectrum. (Such a finding has also been observed by Khan et.al.[6]) In the P-1 polymorph, the pyridine rings around the cyclobutane lack inversion symmetry, creating an inequivalence which leads to multiple ^{13}C peaks in the cyclobutane region. The effect also corresponds to different shifts of the pyridine rings. The single cyclobutane resonance in our experiments leads us to conclude that the $P2_1/n$ polymorph has been formed, while avoiding the formation of the P-1 species.

Chemical shift simulations of the possible tpcb·res polymorphs were performed, and corresponding peak assignments of the product are shown for determining the structure formed. Scheme 5.2 shows the lettering scheme used in the assignment of peaks based on the experimental and theoretical chemical shifts. The assignment of the peaks is shown in the first

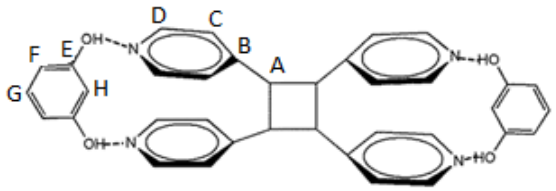

Scheme 5.2: Lettering scheme for assignment of product peaks

Table 5.1: Simulated and experimental chemical shifts for tcbp·res polymorphs; letters refer to positions of atoms in the product structure shown in Scheme 5.2 and numbers in parentheses refer to degeneracy.

Assignment	**Experimental Chemical Shifts** *(ppm)*	**Theoretical Chemical Shifts** *(ppm)*	
		$P2_1/n$ polymorph	P-1 polymorph
Cyclobutane carbons (A)	41.93 (4)	43.85 (4)	42.94 (2), 43.71(2)
Res ipso carbons (H)	101.12 (2)	96.83 (2)	94.49 (2)
Res carbons (F)	106.18 (4)	108.58 (4)	103.8 (2), 107.5(2)
Bpe carbons (C)	119.88 (8) 124.69	124.86 (8) 127.32	122.0-122.7 (8) 126.00
Res carbons (G)	129.824 (2)	130.29 (2)	125.9 (2)
Bpe ipso carbons (B)	142.80 (2)	148.85 (2)	147.0-147.4 (2)
Bpe carbons next to N (D)	147.68 (8)	151.60 (8)	148.5-151.90 (8)
Res carbons with OH (E)	161.21 (4)	162.35 (4)	158-160 (4)

column of Table 5.1 based on Scheme 5.2 and the second column of Table 5.1 contains the experimentally determined chemical shifts of the 90 hour reacted sample. The last column(s) of

Table 5.1 shows the theoretical chemical shifts of the two possible product polymorphs (see Figure 5.7) determined from Gaussian09 simulations. Note that even though the chemical shifts are not exact, simulations predict a single peak in the cyclobutane region for the $P2_1/n$ polymorph, which matches the experimentally observed single peak. The position of the ipso carbons (Scheme 5.2 site B) with respect to the other shifts and the close shifts of the bpe carbons at position C (see Scheme 5.2) match experiments. These various sites are also consistent with the symmetry of the $P2_1/n$ crystal structure (Figure 5.7a). The P-1 simulations (last column) have two chemical shifts for cyclobutane carbons; there is also a splitting in the resorcinol carbons at position F. The resorcinol carbons at position G are no longer at a higher chemical shift than the carbons in position C. The chemical shift simulations are also consistent with the symmetry of the P-1 crystal structure.

To examine the crystal structures of the products, powder X-ray diffraction experiments (pXRD) were performed. (Even though the unreacted crystallites are on the order of 1mm diameter, as the photoreaction occurs, the crystals begin to break apart forming a fine powder such that single-crystal XRD could not be performed on the product.) In Figure 5.8, the diffraction data for a) an unreacted sample of bpe·res and b) a 90-hour irradiated sample is given. Figure 5.8c) and d) are simulated powder patterns (from Mercury 2.4) based on the published structures for the $P2_1/n$ polymorph[30] and the partially-reacted (42%) as-dimerized product (P-1 polymorph)[6]. Many of the features in the reacted sample match well with reflections observed for the unreacted species and $P2_1/n$ polymorph. The vertical lines are guides for the eye. The red lines correspond to the unreacted sample features (top), and the blue lines to the $P2_1/n$ reflections (5.8c) that match. What is apparent is that there is little or no correspondence between P-1 peaks and that of our reacted sample. Features that are missing in

the reacted sample that are prominent in the P-1 powder pattern (5.8d, green), include the region between 12° - 15° 2θ values, as well as the features at 26° and 28°. No appreciable peaks were present past a 2θ value of 40° so these data are not shown.

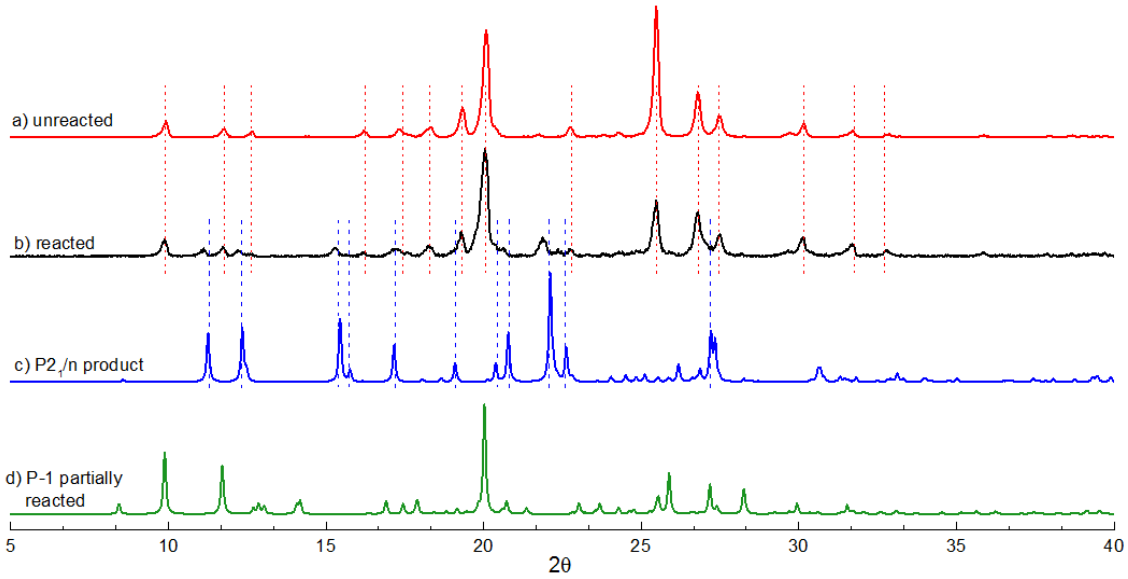

Figure 5.8: Powder X-ray diffraction experiments of a) a 90-hour reacted sample in black, and b) an unreacted sample in red. Simulated powder patterns of c) recrystallized product ($P2_1/n$) in blue and d) partially reacted (42%) product (P-1) in green. Lines highlight matching 2θ values for reacted sample.

The pXRD experiments demonstrate that there is still some unreacted species present in the 90-hour sample. Based on the NMR of the same sample, it appears that complete conversion to the product has occurred. This disparity in results (between pXRD and NMR) maybe attributed to the resolution issues associated with solid-state NMR. NMR can resolve 10^{16}-10^{17}nuclear spins in a given chemical environment, whereas pXRD has a detection limit of 5% by weight. For this system, our 60mg sample may have unreacted bpe·res of up to 3 mg, which is below the detection limit for NMR.

5.4 Conclusions

This study shows that solid –state NMR can be used to monitor the wavelength selective photoreaction of 2(4, 4-bipyridyl ethylene)*2(resorcinol) co-crystals. The effect of wavelength

on the photoreaction has been analyzed for several different wavelengths; the first wavelength in which a photoreaction was observed was at 350 nm. The [2+2] photocycloaddition at 350 nm was monitored using CPMAS techniques. The absorption at this wavelength is higher than the "tail" of the absorption band, as seen in the cinnamic acid case. From the observation of the product in the NMR experiments and corresponding simulations and powder X-ray diffraction experiments, the crystal structure of the product forming in this wavelength selective photoreaction was determined to be the $P2_1/n$ crystal structure. This structure was originally observed from dissolution and recrystallization[3] and determined to be the thermally-stable product[6]. It is the first time this structure has been observed during the progress of a photoreaction. The kinetics of the photoreaction were also determined based on NMR experiments. The kinetics were fit to a JMAK nucleation and growth model in which occurs through a 1-D linear inhomogeneous growth. Based on the kinetics, the photoreaction has gone nearly to completion, but XRD experiments confirm that there is still some reactant present; these experiments also confirm the selective formation of the product $P2_1/n$ crystal structure. In combination, these results show that at 350nm photoreaction, there is a selective product formation of the $P2_1/n$ crystal of rctt-(tetrakis(4-pyridyl)cyclobutane)* 2(resorcinol). Solid-state NMR coupled with powder X-ray diffraction gives more information than a single technique can provide; together they can confirm the extent of the reaction as well as determine the exact product structure forming.

5.5 References

(1) Desiraju, G. R. *Angewandte Chemie International Edition in English* **1995**, *34*, 2311-2327.

(2) Weyna, D. R.; Shattock, T.; Vishweshwar, P.; Zaworotko, M. J. *Crystal Growth & Design* **2009**, *9*, 1106-1123.

(3) Macgillivray, L. R.; Reid, J. L.; Ripmeester, J. A. *Journal of the American Chemical Society* **2000**, *122*, 7817-7818.

(4) Khan, M. Structural Transformations related to organic solid-state reactions: Correlation studies of NMR and X-ray analysis, Johannes Gutenberg-Universitat Mainz, 2008, Vol. 77, pp. 1-171.

(5) *rctt* stands for regional, cis, trans, trans which is the orientation of groups attached to cyclobutane.

(6) Khan, M.; Enkelmann, V.; Brunklaus, G. *The Journal of Organic Chemistry* **2009**, *74*, 2261-70.

(7) Khan, M.; Enkelmann, V.; Brunklaus, G. *Crystal Engineering Communications* **2009**, *11*, 1001.

(8) McBride, J. M.; Segmuller, B. E.; Hollingsworth, M. D.; Mills, D. E.; Weber, B. a *Science* **1986**, *234*, 830-5.

(9) Frisch, M. J.; Trucks, G. W.; Schlegel, H. B.; Scuseria, G. E.; Robb, M. A.; Cheeseman, J. R.; Scalmani, G.; Barone, V.; Mennucci, B.; Petersson, G. A.; Nakatsuji, H.; Caricato, M.; Li, X.; Hratchian, H. P.; Izmaylov, A. F.; Bloino, J.; Zheng, G.; Sonnenberg, J. L.; Hada, M.; Ehara, M.; Toyota, K.; Fukuda, R.; Hasegawa, J.; Ishida, M.; Nakajima, T.; Honda, Y.; Kitao, O.; Nakai, H.; Vreven, T.; Montgomery, Jr., J. A.; Peralta, J. E.; Ogliaro, F.; Bearpark, M.; Heyd, J. J.; Brothers, E.; Kudin, K. N.; Staroverov, V. N.; Kobayashi, R.; Normand, J.; Raghavachari, K.; Rendell, A.; Burant, J. C.; Iyengar, S. S.; Tomasi, J.; Cossi, M.; Rega, N.; Millam, N. J.; Klene, M.; Knox, J. E.; Cross, J. B.; Bakken, V.; Adamo, C.; Jaramillo, J.; Gomperts, R.; Stratmann, R. E.; Yazyev, O.; ; Austin, A. J.; Cammi, R.; Pomelli, C.; Ochterski, J. W.; Martin, R. L.; Morokuma, K.; Zakrzewski, V. G.; Voth, G. A.; Salvador, P.; Dannenberg, J. J.; Dapprich, S.; Daniels, A. D.; Farkas, Ö.; Foresman, J. B.; Ortiz, J. V.; Cioslowski, J.; Fox, D. J. Gaussian09 (Revision A.02) Gaussian Inc., Wallingford, CT, **2009**.

(10) Becke, A. D. *Journal of Chemical Physics* **1993**, *98*, 5648-52.

(11) Lee, C.; Yang, W.; Parr, R. G. *Physical Review B* **1988**, *37*, 785-89.

(12) Krishnan, R.; Binkley, J. S.; Seeger, R.; Pople, J. A. *Journal of Chemical Physics* **1980**, *72*, 650.

(13) Wolinski, K.; Hilton, J. F.; Pulay, P. *Journal of the American Chemical Society* **1990**, *112*, 8251-60.

(14) Komin, S.; Gossens, C.; Tavernelli, I.; Rothlisberger, U.; Sebastiani, D. *Journal of Physical Chemistry B* **2007**, *111*, 5225-5232.

(15) Avrami, M. *The Journal of Chemical Physics* **1940**, *8*, 212.

(16) Avrami, M. *The Journal of Chemical Physics* **1941**, *9*, 177.

(17) Avrami, M. *The Journal of Chemical Physics* **1939**, *7*, 1103.

(18) Kolmogorov, A. N. *Bull. Acad. Sci. USSR Phys. Ser.* **1937**, *1*, 355–359.

(19) Johnson, W. A.; Mehl, R. F. *Am. Inst. Mining Metall. Eng.* **1939**, *1089*, 1–27.

(20) Fonseca, I.; Hayes, S. E.; Blümich, B.; Bertmer, M. *Physical Chemistry Chemical Physics* **2008**, *10*, 5898-907.

(21) Benedict, J. B.; Coppens, P. *The Journal of Physical Chemistry A* **2009**, *113*, 3116-20.

(22) Sun, N. X.; Liu, X. D.; Lu, K. *Scripta Materialia* **1996**, *34*, 1201-1207.

(23) Weinberg, M. C.; Iii, D. P. B.; Shneidman, V. A. *Journal of Non-Crystalline Solids* **1997**, *219*, 89-99.

(24) Bertmer, M.; Nieuwendaal, R. C.; Barnes, A. B.; Hayes, S. E. *Journal of Physical Chemistry B* **2006**, *110*, 6270-6273.

(25) Fonseca, I.; Hayes, S. E.; Bertmer, M. *Physical Chemistry Chemical Physics* **2009**, *11*, 10211-8.

(26) Cao, D.-K.; Sreevidya, T. V.; Botoshansky, M.; Golden, G.; Benedict, J. B.; Kaftory, M. *The Journal of Physical Chemistry A* **2010**, *114*, 7377-81.

(27) Destro, R.; Ortoleva, E.; Soave, R.; Loconte, L.; Lo Presti, L. *Physical Chemistry Chemical Physics* **2009**, *11*, 7181-8.

(28) Busse, G.; Paulmann, C.; Scholz, M.; Techert, S. *Journal of Physical Chemisty C* **2010**, *114*, 4142-4148.

(29) Jenkins, S.; Almond, M.; Atkinson, S.; Drew, M.; Hollins, P.; Mortimore, J.; Tobin, M. *Journal of Molecular Structure* **2006**, *786*, 220-226.

(30) Varshney, D. B.; Papaefstathiou, G. S.; MacGillivray, L. R. *Chemical Communications* **2002**, *646*, 1964-5.

Chapter 6: Photocrosslinking of Poly(cinnamoyl oxyethyl methacrylate)

6.1 Introduction

Crosslinking of polymers is important for the understanding and development of useful materials. This chapter focuses on a polymer that has been used in materials with shape-memory properties[1], in development of micelles[2–4], use as potential oil absorbers[5,6], and negative photoresists[7]. The crosslinking of these materials has been studied using UV-visible (UV-vis) spectroscopy[2] and infrared (IR) spectroscopy[8]. Presented here is the first time that evaluation of this polymer photo-crosslinking has been performed using solid state NMR spectroscopy. The [2+2] photocycloaddition that is responsible for the crosslinking of these polymers is an application of the photoreactions that have been presented in the previous sections of this thesis. The intrinsic properties of these materials are affected by the amount and type of photocrosslinking that occur[9,10]; therefore, quantitative structural analyses of what is taking place is necessary for the creation of better products. Another interesting aspect of the polymer is the reversibility of the crosslinking, which is dependent on wavelength. The synthesis and respective analyses of poly(cinnamoyl oxyethyl methacrylate) will be presented using solution NMR and solid state NMR techniques.

6.2 Experimental Methods

Materials and Reagents

Hydroxyethyl methacrylate (**HEMA**) was purchased from Sigma Aldrich and then run through a column to remove inhibitors prior to synthesis. All other materials were obtained from commercial sources and used without further purification.

Synthesis of Monomer and Polymer

The monomer, cinnamoyl oxy ethyl methacrylate, (**CEMA**) was synthesized from cinnamic acid and HEMA through a Steglich esterification[11,12]. The synthesis was performed using 4-dimethylaminopyridine (**DMAP**) and 1-ethyl-3-(3-dimethylaminopropyl) carbodiimide (**EDC**) stirred under nitrogen at room temperature for 12 hours in dichloromethane. Purification steps included an extraction with dichloromethane/ sodium bicarbonate and a silica gel column using a 16:1 diethyl ether: hexane mixture.

Two polymerization techniques were employed for synthesis of poly (cinnamoyl oxyethyl methacrylate) (**polyCEMA**). Method 1 was a free radical polymerization of the monomer using azobisisobutyronitrile (**AIBN**) initiator dissolved in dry benzene under vacuum at 80°C for 12 hours[13]. The reactants underwent several freeze-pump-thaw cycles before being heated, to remove any species that could quench the polymerization (i.e. oxygen). Method 2 (material courtesy of Dr. Libo Hu)[14] was through an atom transfer radical polymerization (**ATRP**)[15–17] of HEMA and esterification of the polyHEMA with cinnamic acid to attach the side chains (as in the original monomer synthesis).

Preparation of Thin Films

Thin films were created from solutions of polyCEMA in acetonitrile or chloroform which were placed drop-wise onto glass slides. Solutions were also spin-coated onto glass slides for 20 seconds at 100% using a home-built spin coater (see below). Typical concentrations of solutions were 1.5 mg/mL.

Development and Use of Spin Coater

Spin coaters are usually necessary for the creation of thin films which can be used in many materials applications. Typically, the cost of a spin coater is ~$15,000. In this instance, a

cost effective spin coater was developed for preliminary testing of the polymers. The design was based on a CPU fan that is normally used for cooling of personal computers[18]. There is a container attached on top of the fan to place the glass slides for coating the thin films. CPU fans are built with three wires attached, the first wire (red) is responsible for controlling spinning, the second (black) is the ground, and the third wire (yellow) measures speed. This third wire is normally used so that the spinning speed can be adjusted based on the heat being produced from the computer. The red wire and black ground are attached to an on-off switch as shown in Figure 6.1. The CPU fan is powered by an AC-DC adaptor, matching the specifications of the fan (DC 12V 100mA); which is plugged into a variable AC (variac) controller (see Figure 6.2) allowing the spinning speed to be varied (measured using a Multimeter). The materials were spin coated at different speeds, varying the amount of time to gain the most effective coating of material.

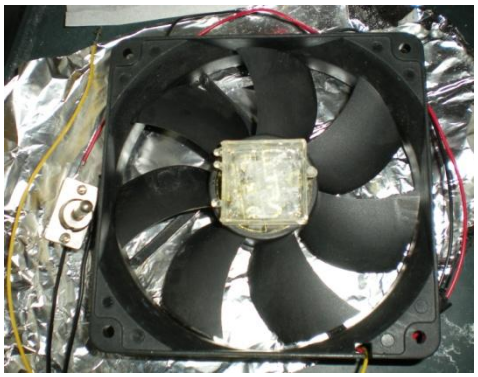

Figure 6.1: Home-built spin-coater for preparation of thin films.

Figure 6.2: Variable AC controller used for adjustment of the spinning speed.

Photo-irradiation and UV-vis Experiments

Photo-irradiation of samples (~60mg) was performed using a 150 W Xe arc lamp (Thermo Oriel). The samples were irradiated with filtered (280-400 nm) broadband light (30 mW output power) and unfiltered (250 nm-1000 nm) light. UV-visible spectroscopy experiments were performed on polyCEMA dissolved in acetonitrile at room temperature using an Agilent/Varian Carey 100 double beam spectrophotometer. The scanning wavelength was

between 190 and 800 nm with a step size of 1 nm. Quartz cuvettes were used with a path length of 1 cm. All UV-vis experiments reported have been background-subtracted.

NMR Experiments

Solution and solid state NMR experiments were used for analysis of the monomer and polymer. The solution NMR experiments were performed in $CDCl_3$ using an Agilent/ Varian Mercury-300 spectrometer with a 5mm gradient broadband probe. ^{1}H, ^{13}C and 2D-HMQC experiments were used to confirm synthesis of the product and correlate ^{1}H and ^{13}C features. Solid-state CPMAS (cross polarization magic angle spinning) experiments[19] with TPPM (two pulse phase modulation) decoupling[20] were done using a 4mm Chemagnetics/Varian HXY probe, with a Tecmag Apollo spectrometer. The working frequencies were ν_C =74. 17 MHz and ν_H = 294.97 MHz. The Hartmann-Hahn match was set with adamantane, which served as a secondary reference for tetramethylsilane (TMS) at 0 ppm. Typical experimental conditions were 2.3 μs ^{1}H π/2 pulses, 1 ms contact time, MAS frequency of 6 kHz, a 5 μs dwell time, recording 1000 transients, and a 7 s recycle delay. Spectral assignments were made using spectral editing, variable contact time, and interrupted decoupling experiments.

6.3 Results and Discussion

Preparation of Monomer and Polymer

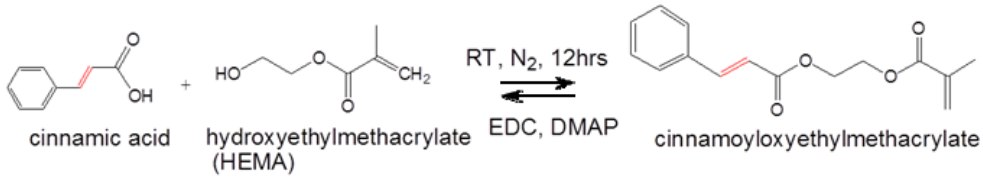

Scheme 6.1: Synthesis of monomer based on a Steglich esterification.

The first step in the analysis of the polymer species is to synthesize the material. The monomer, cinnamoyl oxyethyl methacrylate (CEMA), was synthesized using a Steglich esterification shown in Scheme 6.1. The crude material then underwent purification as described in Section 6.2. The purified monomer was analyzed using solution NMR to confirm formation of product and purity. The ^{1}H NMR spectrum and assignment based on the given structure is shown in Figure 6.3. Chemical shift assignments are given in Table 6.1 along with multiplicity, J-coupling, and number of associated protons.

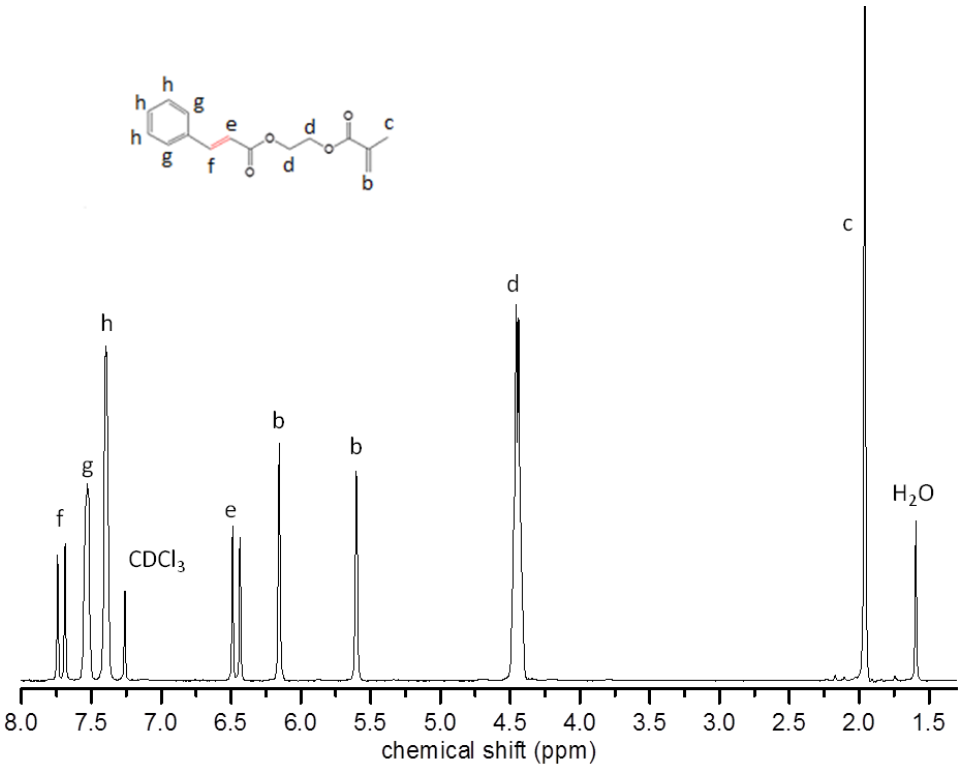

Figure 6.3: ^{1}H NMR spectrum of CEMA monomer. The peak assignments are lettered based on the given structure. Residual solvent peaks are given.

Table 6.1: Chemical shift information for assignment of ^{1}H NMR spectrum of monomer

^{1}H Chemical Shift (ppm)	**Multiplicity (J-coupling)**	**Schematic Lettering/ Number of Protons**
1.97	s	c, 3H
4.46	m	d, 4H
5.61	s (165 Hz)	b, 1H
6.17	s (165 Hz)	b, 1H
6.44	d (16 Hz)	e, 1H
7.39	m	h, 3H
7.53	m	g, 2H
7.72	d (16 Hz)	f, 1H
7.27	s	$CDCl_3$ solvent peak
1.58	s	H_2O peak

The next step of the synthesis was to polymerize the material. There were two different methods used to polymerize CEMA: Method 1 was a free radical polymerization (see Scheme 6.2) and Method 2 was an atom transfer radical polymerization (ATRP). Free radical

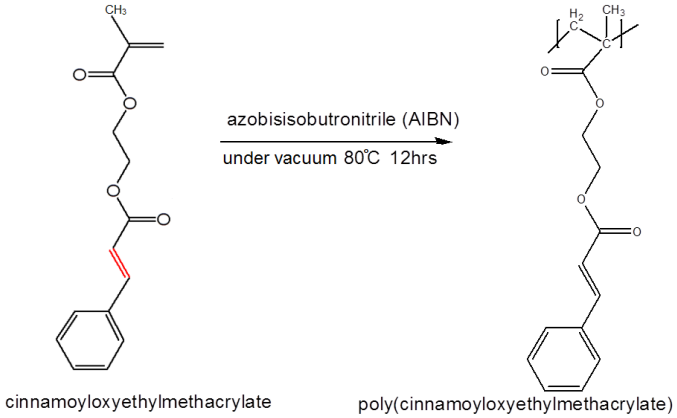

Scheme 6.2: Method 1: free radical polymerization of cinnamoyloxyethyl methacrylate.

polymerization of CEMA using AIBN made inconsistent polymers, varying visibly from batch to batch. This inconsistency is due to the difficulty in non-controlled free radical polymerizations to precisely control the molecular weight and molecular weight distribution of the product[14]. In these non-controlled polymerizations, the molecular weight increases exponentially from initiation[14]. Also, temperature has an effect on the polymerization, above 80°C, the vinyl on the side-chain of the polymer (in red, Scheme 6.2) can polymerize as well[14]. Method 2 (material

courtesy of Dr Libo Hu) used for synthesis of the polymer is ATRP which allows better control of molecular weight and a smaller dispersion[15]. It also follows a linear increase in molecular weight[14]. This controlled polymerization was performed on HEMA and the subsequent steps for purification and attachment of the side chains (see Section 6.2) help to eliminate unwanted polymerization at the crosslinking site[21]. This difference is shown by comparison of the ^{1}H NMR spectra of polymers synthesized from Method 1 and 2 as seen in Figure 6.4. The polymerization is denoted as a disappearance of the monomer peaks at 5.61 and 6.17 ppm and the appearance of signal at ~1.9 ppm. In Method 1, there is still some residual monomer present in a small amount as seen by the "bumps" at 5.5 and 6.0 ppm in Figure 6.4a. The peak assignments are denoted in Figure 6.4. There are two sets of peaks present for the two OCH_2 groups in Method 2. Note the narrower distribution of chemical shifts for the CH_2 group for Method 2 (1.8-2.0 ppm) compared to Method 1 (2.0-1.6 ppm).

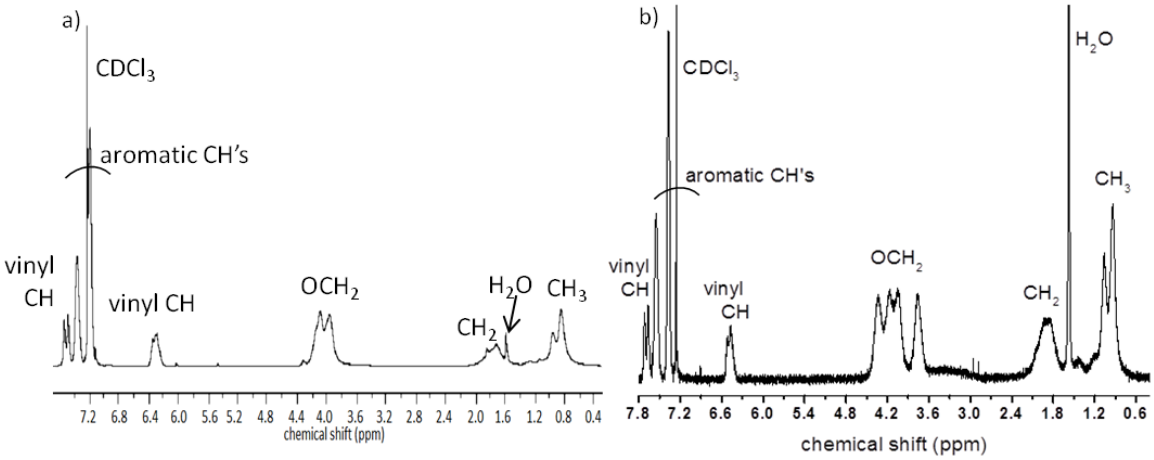

Figure 6.4: ^{1}H NMR spectra of polyCEMA synthesized via a) Method 1 and b) Method 2. Peaks are labeled with their respective assignments.

Characterization of Polymer

Several NMR techniques were used to analyze the "neat" (i.e. unreacted) polymer prior to photo-irradiation. Solution NMR experiments were used for confirmation of a successful polymerization (see Figures 6.3 and 6.4) and to assign specific resonances. Solid state NMR was also used for characterization of the polymer, which is useful for crosslinked species that are no longer amenable to solution-phase NMR analyses. The solution NMR experiments were ^{13}C NMR with ^{1}H decoupling and 2D- gradient selected HMQC (heteronuclear multiple quantum correlation)[22]. The solid state experiments used for characterization of the polymer were CPMAS

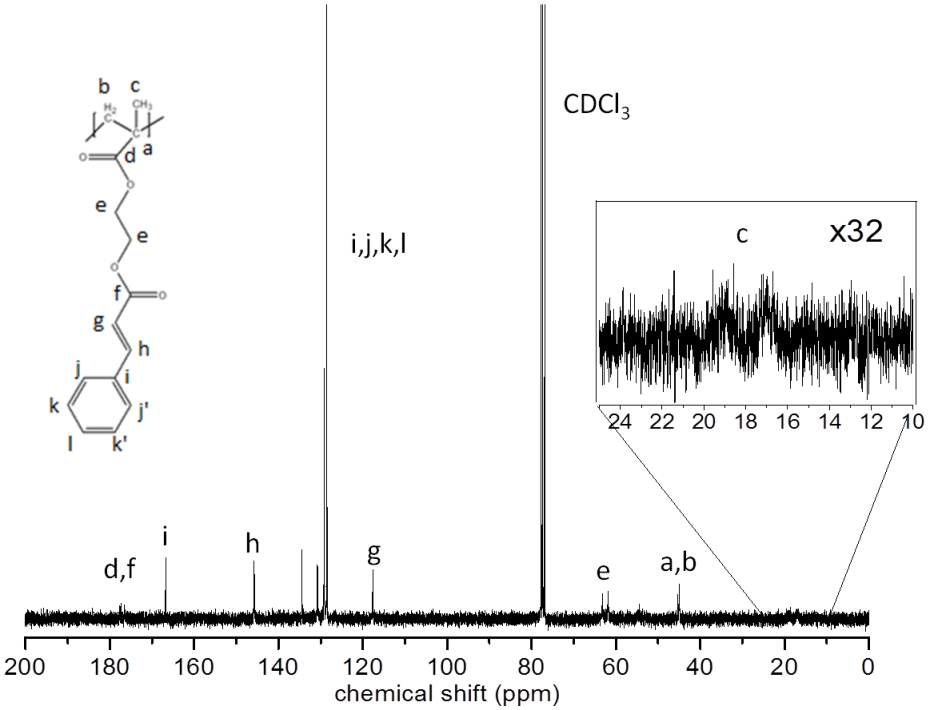

Figure 6.5: ^{13}C solution NMR spectrum of polyCEMA. Assignment of features is given in the inset structure.

experiments, interrupted decoupling (data not shown), and variable contact time CPMAS experiments for spectral editing. The ^{13}C solution NMR experiment for the polymer is shown in Figure 6.5. The peak assignments for the carbons are given based on the structure of the polymer. Some of the peaks are slightly less resolved than others such as the methyl on the

backbone of the polymer (site c, ~20ppm) (shown in the inset of Figure 6.5).The solvent used in the solution NMR experiment was $CDCl_3$ (deuterated chloroform); peaks for the residual solvent are also shown in Figure 6.5.

A second NMR experiment was also performed on the polymer to definitively assign the peaks in both the ^{1}H and ^{13}C spectra of the polymer and to also establish correlations between the two nuclei. The 2-D gradient-selected HMQC experiment was performed and is shown in Figure 6.6. HMQC is used for determination of directly bonded C-H's by correlation of ^{13}C and ^{1}H resonances in the F1 and F2 dimension, respectively. The resolved features are shown through dotted lines connecting the ^{1}H signals with the corresponding ^{13}C features. A 1-D projection of each dimension is also given in Figure 6.6. The aromatic ring CH's appear, as well as the CH_2's of

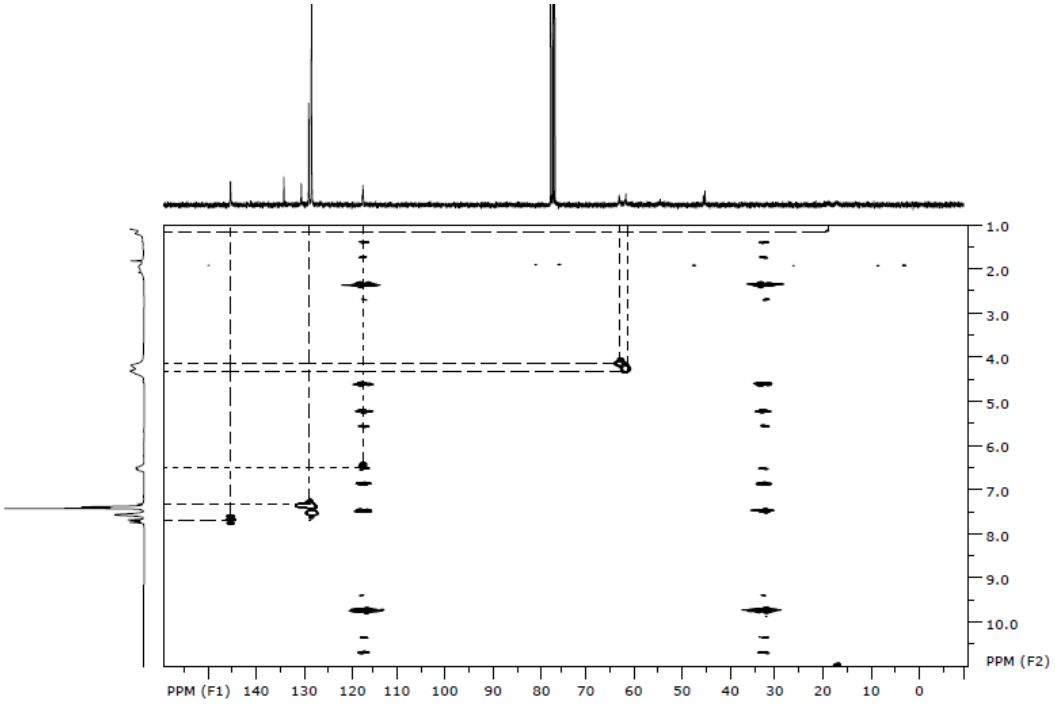

Figure 6.6: ^{13}C-^{1}H HMQC correlation experiments. Dotted lines show correlations between features.

the ester, both vinyl CH's on the side chain, and the methyl group (CH_3). The only peak not present is the CH_2 in the backbone of the polymer. It is unclear why the cross peak is not

present. The solution NMR experiments determined that the polymer synthesis was successful, and confirmed the presence of residual vinyls available for crosslinking, and assignments of the chemical shifts for both ^{1}H and ^{13}C.

When polyCEMA is irradiated with photons, it crosslinks and becomes insoluble; so, analysis of the material cannot be accomplished in solution after the crosslinking has occurred. We therefore performed solid state NMR experiments on both the unreacted and reacted polyCEMA. The solid state ^{13}C {^{1}H} CPMAS spectrum for unreacted polymer is shown in Figure 6.7 with the peak assignments indicated. Note that the shifts are similar to what was observed in the ^{13}C solution NMR experiment.

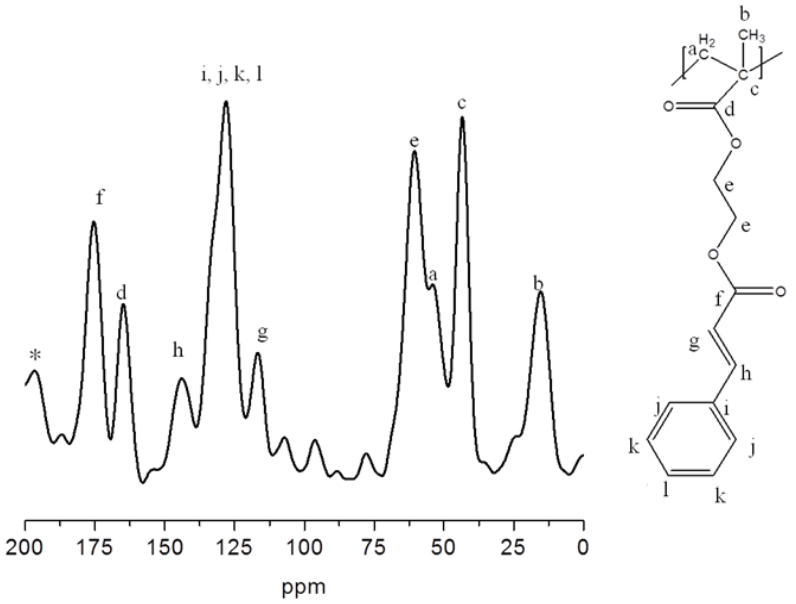

Figure 6.7: Solid state ^{13}C CPMAS experiments of polyCEMA with chemical shift assignments. (*denotes spinning sidebands)

In solid state CPMAS NMR, spectral editing methods for characterization of resonances are often used [23–25]. Variable contact time experiments were used to assist with assignments, and these experiments also give information about the kinetics and dynamics that occur during

cross-polarization[26]. The data were fit to a kinetics equation (Equation 1) that describes the relaxation that occurs during variable contact time experiments[26].

$$I(t) = I_0\left(1 - \frac{T_{HC}}{T^H{}_{1\rho}}\right)^{-1} * \left[exp\left(-\frac{t}{T^H{}_{1\rho}}\right) - exp\left(-\frac{t}{T_{HC}}\right)\right] \quad (1)$$

where $I(t)$ is the intensity as a function of time, I_0 is the initial intensity, t is the contact time, T_{HC} is the CP time constant, and $T^H{}_{1\rho}$ is the time constant for ^{1}H relaxation in the rotating frame. This equation makes several assumptions: that the system is a dilute-abundant spin system, and the ^{13}C relaxation in the rotating frame ($T^C{}_{1\rho}$) is long compared to T_{HC} [26]. These assumptions generally hold true for the polymer. Figure 6.8 is separated into a) the lower frequency chemical shifts and b) higher frequency chemical shift values for clarity. The points are measurements of intensity of the peaks for different contact times in the CPMAS experiments. The solid lines are fits to Equation 1. Table 6.2 gives a list of the values from the fits, as well as the assignment of the chemical shifts. Based on the curves, the optimal contact time of 1 ms was found (based on the curves: the time at which there is still a large amount of signal intensity without too much decay for all species) and used for all other experiments. The resolution in the variable contact

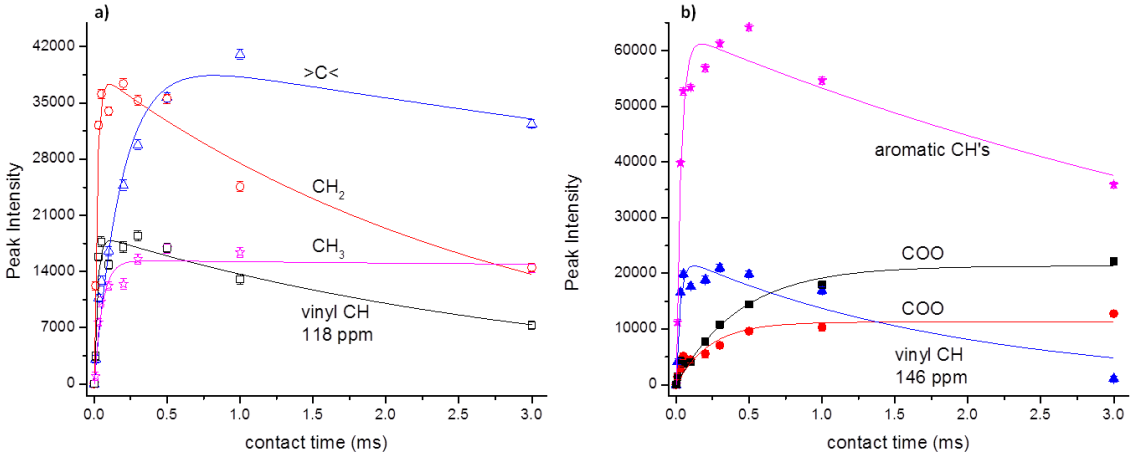

Figure 6.8: ^{13}C{^{1}H} CPMAS variable contact time experiments for a) lower frequency peaks and b) higher frequency peaks of polyCEMA. Lines are based on fits to the kinetics equation. The assignments are given.

time experiments was such that separation of the ester CH_2's and the backbone CH_2 which had similar chemical shifts (~61 ppm) was not possible.

The various time constants for each spectral feature are given in Table 6.2. The different relaxation times and time constants give insight into the polymer material itself. The spin lattice relaxation times in the rotating frame are dependent on motion. If the material is more rigid, then the dynamics are slower, and if the material is more mobile, then the dynamics will be faster[27]. A similar study of polyHEMA had room temperature $T_{1\rho}$ values of 15 ms for the methyl, the quaternary carbon was 20 ms, the CH_2 in the backbone was 2 ms, the other CH_2's were

Table 6.2: Summary of variable contact time experiments.

Spectral Assignment	**Chemical Shift** (ppm)	**Peak Intensity** I_0	**^{1}H Spin Lattice Relaxation (in Rot. Frame)** $T^H_{1\rho}$ (ms)	**CP Time Constant** T_{HC} (ms)
CH_3 (b)	17	15399	86.80	0.0541
Backbone quaternary (c)	44	40933	13.01	0.1924
Ester CH_2 (e), backbone CH_2 (a)	61	38726	2.85	0.0201
Vinyl (g)	118	18491	3.23	0.0221
Aromatic (i,j,k,l)	129	63054	5.73	0.0330
Vinyl (h)	143	22787	1.92	0.0283
Ester (d)	166	11254	(9.51 E18) ∞	0.2302
Ester (f)	177	21326	(4.15 E16) ∞	0.4361

about 3-4 ms, and the carbonyl was 40 ms[28]. The values found in the polyCEMA here are comparable to those values. Also, the rapid build-up and decay for the directly protonated carbons is to be expected. Those carbons which must be polarized through spin diffusion (non-protonated carbons) or have motion, like methyls, have a longer build-up time and therefore a longer decay. The esters in Table 6.2 would have a better fit for $T_{1\rho}$ values if the variable contact times had gone out further (longer than 3ms), so that the signal could have begun to decay. The CP time constants (T_{HC}) give a measure of the thermal contact between the two systems (the

interaction time between two spins)[29]. In general, for a rigid polymer with some motion, the values for T_{HC} range from 0.05 ms for protonated carbons and 0.5 ms for quaternary carbons[29]; therefore, it could be assumed that a more mobile polymer will have shorter times, as seen in polyCEMA (Table 6.2 column 4).

Monitoring the Photoreaction

The amount and type of crosslinking, and the reversibility of the reaction that can occur in polyCEMA have never been quantitatively measured using NMR. A schematic of several photocrosslinks that can occur in the polymer is shown in Scheme 6.3. The different types of reactions that can occur are interchain, (shown in green) forming trans-products (truxillic acid-like), and intrachain (shown in red), forming cis-products (truxinic acid-like). There may also be

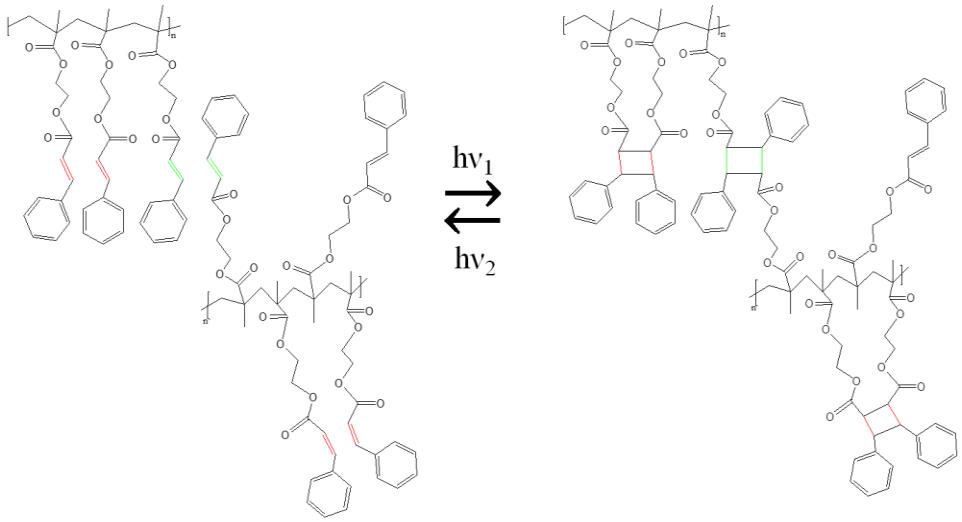

Scheme 6.3: Possible orientations for the polymer side-chains and potential photoreactive sites (green and red) in the polymer. Rreversibility of the photoreaction using different wavelengths of light is indicated.

some side chains that do not react (in black), due to the lack of an adjacent side chain in the correct proximity. (Note: the general topochemical principle for photoreactions in the solid state may apply, with ~4.2Å proximity requirement.) Scheme 6.3 also shows some possible orientations of the polymer side-chains, referred to as tacticity, which can either be all on the

same side (isotactic) (as shown at the top), or they could alternate(syndiotactic) (as shown on bottom); another possibility (not shown) is an atactic orientation, which contains no regular sequence of residues.

Figure 6.9 shows the solution UV-vis absorption spectrum for the polymer as dilute solution in CH_3CN. This solvent was chosen based on the solubility of polyCEMA, and on its absorptive range. In general, this type of photoreaction has high absorption in the UV region of

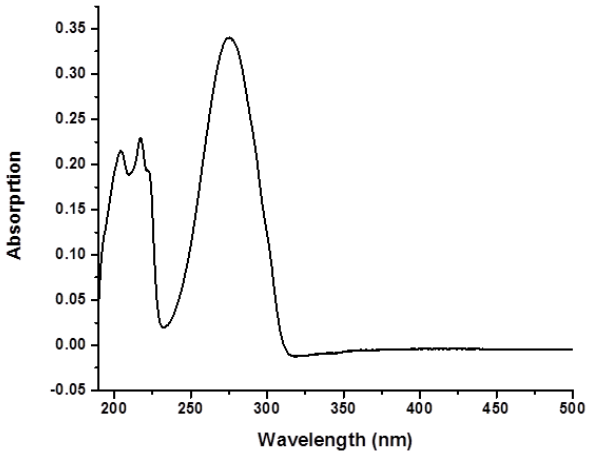

Figure 6.9: UV-vis absorption spectrum for polyCEMA dissolved in acetonitrile.

the spectrum; therefore, it is important to select a solvent that has a low absorption in the region of interest (see Appendix I for full list of solvents). The highest absorption wavelength (λ_{max}) is at 275.5 nm for polyCEMA. Some early irradiations were performed using a dichroic filter selecting a band of wavelengths between 280-400 nm, and were only irradiating at the "tail" of the absorption; no evidence of reaction was observed for these irradiations. Photoreactions in these polymers have been shown to occur more quickly than the powders or single crystals of the previous chapters. Typical irradiation times are on the order of thirty minutes to an hour.

Broadband arc-lamp irradiations (250 nm-1000 nm) were performed on polyCEMA and analyzed using solid state NMR experiments. Figure 6.10 shows the ^{13}C {^{1}H} CPMAS spectra of

the unreacted and photoreacted poly (cinnamoyl oxyethyl methacrylate) after one hour of broadband irradiation. Note the changes in intensity of the chemical shifts at 118 ppm and 140 ppm (highlighted in gray). These correspond to the vinyl carbons that are available to undergo

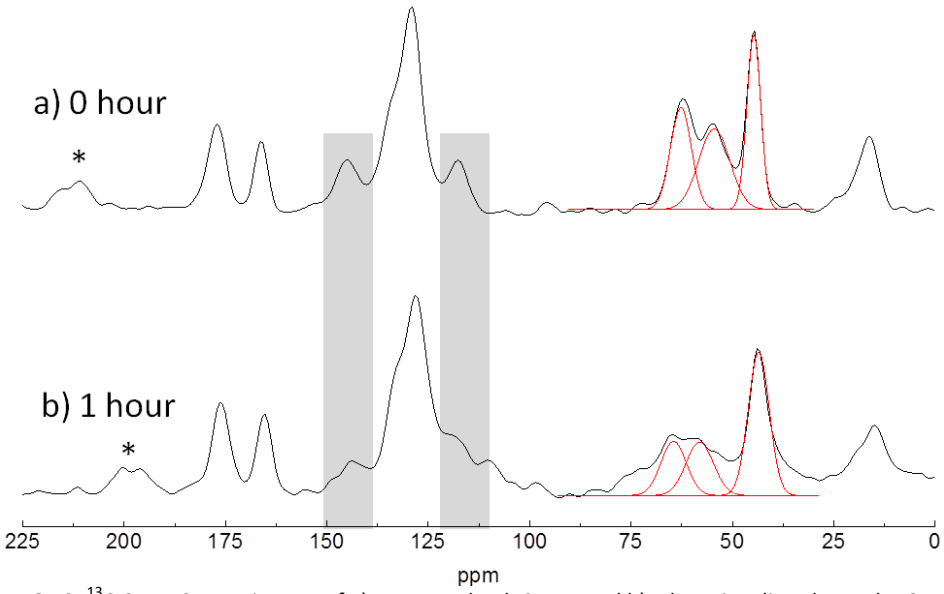

Figure 6.10: ^{13}C CPMAS experiments of a) unreacted polyCEMA and b) 1 hour irradiated sample. Gray area highlights vinyls responsible for crosslinking. Red lines denote fits of overlapping features. (* denotes spinning sidebands.)

photoreaction. The intensity decreases visibly after having been irradiated for only one hour (Figure 6.10 b). The crosslinked product (cyclobutane) is expected to appear at 40-55 ppm depending on the form of the product (cis versus trans). There is major overlap of the backbone and side chain aliphatic carbons and the quaternary carbon (see red outlined features in Figure 6.10) with the cyclobutane region; therefore resolution of the product was not able to be determined in the natural abundance ^{13}C experiments of polyCEMA. Note some broadening in the region of interest for the photoreacted polymer (6.10b), but no distinguishing features.

6.4 Conclusions and Future Work

The monomer, cinnamoyl oxyethyl methacrylate, was synthesized from cinnamic acid and hydroxyethyl methacrylate based on a Steglich esterification and purified. Poly (cinnamoyl

oxyethyl methacrylate) was prepared using two different methods of polymerization. Method 1 was a free radical polymerization which formed inconsistent products. Method 2, polymerization using ATRP, (courtesy of Dr. Libo Hu) produced a more consistent polymer and was therefore used for further analysis. This material undergoes a [2+2] photocycloaddition under UV irradiation. Solution NMR experiments showed successful synthesis of the monomer and polymer and allowed for assignment of the ^{1}H and ^{13}C chemical shifts. Solid state ^{13}C $\{^{1}H\}$ CPMAS NMR experiments were used to study the photoreaction due to the insoluble nature of the polymer once photocrosslinked. Variable contact time CPMAS experiments were also performed. After broadband irradiation, as short as 1 hour, there was a visible decrease in the reactive vinyls.

Future Work

To assist in the elucidation of the product structure of polyCEMA, future experiments will use ^{13}C labeled cinnamic acid (based on synthesis in Chapter 4) to isotopically enrich the vinyl carbons on the side chains of the polymer. Even if only 50% of the side chains are labeled, there would be a definite signal enhancement to discriminate the reactant and product. This labeling will allow more accurate quantification of the kinetics of the photoreaction. It would also help to resolve which products develop, intrachain versus interchain, in the reaction. Then, a quantitative analysis into the reversibility of the photocrosslinking could also be performed.

6.5 References

(1) Lendlein, A.; Jiang, H.; Junger, O.; Langer, R. *Nature* **2005**, *434*, 695-697.

(2) Kousaka, S.; Sugahara, M.; Endo, T.; Yusa, S.-ichi *Journal of Physics: Conference Series* **2011**, *012012*, 1-4.

(3) Rodriguez-Hernandez, J.. Checot, F., Gnanou, Y. Lecommandoux, S. *Progress in Polymer Science* **2005**, *30*, 691- 724.

(4) Liu, F.; Liu, G. *Macromolecules* **2001**, *34*, 1302-1307.

(5) Kim, S.; Chung, I.; Ha, C.; Kim, K.; Cho, W. *Journal of Applied Polymer Science* **1998**, 2349-2357.

(6) Atta, A. M.; El-Ghazawy, R. A.; Farag, R. K.; El-Kafrawy, A. F.; Abdel-Azim, A.-A. A. *Polymer International* **2005**, *54*, 1088-1096.

(7) Minsk, L. M.; Smith, J. G.; van Deusen, W. P.; Wright, J. F. *Journal of Applied Polymer Science* **1959**, *2*, 302-307.

(8) Chung, C.; Roh, Y.; Cho, S.; Kim, J. *Chemistry of Materials* **2004**, *16*, 3982-3984.

(9) Safranski, D. L.; Gall, K. *Polymer* **2008**, *49*, 4446-4455.

(10) Hong, L.; Liu, G. *Macromolecules* **2010**, *43*, 3941-3946.

(11) Neises, B.; Steglich, W. *Organic Syntheses* **1985**, *63*, 183.

(12) Shelkov, R.; Nahmany, M.; Melman, A. *Organic & Biomolecular Chemistry* **2004**, *2*, 397-401.

(13) Ali, A. H.; Srinivasan, K. S. V. *Journal of Applied Polymer Science* **1998**, *67*, 441-448.

(14) Hu, L. Examination of UV-Cross-Linkable Di-Block Copolymer Strategy for Functionalized Reaction Surface on Microelectrode Arrays, Washington University in St. Louis, 2011, pp. 1-231.

(15) Beers, K. L.; Boo, S.; Gaynor, S. G.; Matyjaszewski, K. *Macromolecules* **1999**, *32*, 5772-5776.

(16) Wang, J.-S.; Matyjaszewski, K. *Macromolecules* **1995**, *28*, 7901-7910.

(17) Ding, J.; Tao, J.; Guo, A.; Stewart, S.; Hu, N.; Birss, V. I.; Liu, G. *Macromolecules* **1996**, *29*, 5398-5405.

(18) Chakraborty, M.; Chowdhury, D.; Chattopadhyay, A. *Journal of Chemical Education* **2003**, *80*, 806-809.

(19) Schaefer, J.; Stejskal, E. O. *Journal of the American Chemical Society* **1976**, *98*, 1031-1032.

(20) Bennett, A. E.; Rienstra, C. M.; Auger, M.; Lakshmi, K. V.; Griffin, R. G. *The Journal of Chemical Physics* **1995**, *103*, 6951.

(21) Tao, J.; Guo, A.; Liu, G. *Macromolecules* **1996**, *29*, 1618-1624.

(22) Andersson, P.; Gsell, B.; Wipf, B.; Senn, H.; Otting, G. *Medical Biochemistry* **1998**, 279-288.

(23) Wu, X.; Zilm, K. W. *Journal of Magnetic Resonance, Series A* **1993**, *102*, 205-213.

(24) Wu, X.; Burns, S. T.; Zilm, K. W. *Journal of Magnetic Resonance, Series A* **1994**, *111*, 29-36.

(25) Burns, S.; Wu, X.; Zilm, K. *Journal of Magnetic Resonance* **2000**, *143*, 352-9.

(26) Kolodziejski, W.; Klinowski, J. *Chemical Reviews* **2002**, *102*, 613-28.

(27) Fülber, C.; Demco, D. E.; Blümich, B. *Solid State Nuclear Magnetic Resonance* **1996**, *6*, 213-223.

(28) Ran, A.; Schueneman, G. T.; Novak, B. M. *Solid State Communications* **1999**, *109*, 465-470.

(29) Stejskal, E. O.; Memory, J. D. *High Resolution NMR in the Solid State*; Oxford University Press: New York, 1994; pp. 78-80.

Chapter 7: Summary and Future Work

7.1 Summary

Solid state nuclear magnetic resonance spectroscopy (NMR) is very useful for elucidating structural information and for gaining insight into the dynamics present in different materials. The benefit of NMR is that it is a non-destructive technique and element selective. In this thesis, solid state NMR has been used to analyze different photoreactive materials that undergo [2+2] photocycloadditions which follow the topochemical postulate. The materials explored in this thesis include photoreactive single crystals, a supramolecular complex, and a photocrosslinking polymer.

The effect of wavelength on these photoreactions is an important part of the studies presented in this thesis, especially for insight into product development. The first two materials explored used wavelength-selective irradiations. The trend observed for these photoreactive materials is that when the wavelength is such that there is high absorptivity, the product that develops is the thermally stable product (as shown in Chapter 5). When irradiation wavelengths with low absorptivity are used, meta-stable products can be observed (as shown in Chapter 4). This trend has also been confirmed in conjunction with previous experiments in the Hayes lab[1,2].

In single crystal experiments, photoirradiation at 350 nm was performed in the "tail" of the absorption band for cinnamic acid. The light can penetrate somewhat evenly through the material, allowing for reaction of sites not just on the surface. When broadband irradiation (280nm-400 nm) was used, there is high absorption on the surface (demonstrated previously[2]). Under the former conditions, cinnamic acid has been shown to undergo a single-crystal-to-single-crystal (SC-to-SC) transformation[3]. In general, this type of transformation has been seen

only for small crystals[4] (nanometer-sized). In our single crystal experiments for cinnamic acid, (millimeter-sized) we have determined that the meta-stable product ($P2_1/n$) of truxillic acid is formed initially. Chapter 4 gives assignment of the chemical shift tensor for the truxillic acid $P2_1/n$ polymorph. Since the structure is meta-stable, the tensor for the cyclobutane of this polymorph had not been characterized previously. In the single crystal rotation experiments, it was observed that the linewidths of the partially-reacted single crystals of cinnamic acid are greater than the unreacted or simulated linewidths. This broadening is due to a slight crystalline dispersion as well as broadening from the reaction.

Inversion recovery experiments for the measurement of product development in the single crystals based on spin diffusion were performed. Even before the product is visible in the NMR spectrum (after 14 hours of irradiation) the effects of the product can be observed. This indicates a solid solution of cinnamic acid and truxillic acid. In a crystal photoirradiated for 24 hours, the domain size of the truxillic acid-rich region is on the order of 214 nm. It has been determined that product development within these crystals is a compositional heterogeneity in which the surface of the crystal has truxillic acid-rich domains and the bottom of the crystal has cinnamic acid-rich domains.

A wavelength-selective irradiation of the supramolecular complex, bipyridyl ethylene-co-resorcinol (bpe·res), was explored in Chapter 5. The resorcinol takes a photo-inert material, bipyridyl ethylene, and transforms it into a photoreactive species through hydrogen bonding[5]; the hydrogen bonding orients it such that the double bonds are within 4.2Å. The photoreactive co-crystal was irradiated with UV light at 350nm. Irradiation at this wavelength produced the thermally stable product, the $P2_1/n$ polymorph, selectively. The product formation was observed using NMR experiments (CPMAS), and confirmed with simulations and powder X-ray diffraction

experiments. The kinetics of the photoreaction were determined to follow the JMAK kinetics model for 1-D heterogeneous nucleation and growth with a rate of 0.017 ± 0.005 hrs^{-1}. The reaction, thought to have gone to completion based on the NMR experiments was observed to be only partially-reacted based on the powder X-ray diffraction experiments; evidence that multiple techniques should be used when analyzing reactions.

Poly (cinnamoyl oxyethyl methacrylate) (polyCEMA), a polymer with shape-memory properties arising from reversible crosslinking, was successfully synthesized in Chapter 6. The method that produced most consistent synthesis of the polymer was an ATRP synthesis, courtesy of Dr. Libo Hu. The understanding of the photocrosslinking will be important for exploration into the reversible nature of the polymer. Solid state NMR is useful for observing this effect, because when irradiated, the material becomes insoluble and difficult to analyze by other techniques. Using CPMAS experiments, the photoreaction was monitored through the decrease in the vinyl intensities, but resolution of the product signal was difficult due to overlap of other chemical shifts from the backbone of the polymer.

7.2 Future Work

Other supramolecular systems exist that are known to undergo a SC-to-SC transformation under UV irradiation. In the original bpe·res complex, the sample becomes a powder after irradiation. In a similar supramolecular complex, when irradiated with UV light, the sample remains a single crystal. The new complex is a cyano-substituted form of the co-crystal[6]. Future exploration of the differences between the two materials could result in a better understanding of the effect of substitutions on the reactivity of these materials, and their ability to undergo SC-to-SC transformations.

In the polymer studies, for further understanding of the crosslinking, it is necessary to isotopically label the side chain (based on isotopically labeled cinnamic acid) such that quantitative analysis of the crosslinking can be achieved. Using the signal enhancement from the isotopic labeling, it would be possible to determine the type and amount of photocrosslinking that occurs in the polymer. The signal enhancement would also allow elucidation of the reversible nature of the polymer and quantify the reversibility.

7.3 References

(1) Bertmer, M.; Nieuwendaal, R. C.; Barnes, A. B.; Hayes, S. E. *Journal of Physical Chemistry B* **2006**, *110*, 6270-6273.

(2) Nieuwendaal, R. C.; Bertmer, M.; Hayes, S. E. *The journal of Physical Chemistry B* **2008**, *112*, 12920-6.

(3) Enkelmann, V.; Wegner, G.; Novak, K.; Wagener, K. B. *Journal of the American Chemical Society* **1993**, *115*, 10390-10391.

(4) Takahashi, S.; Miura, H.; Kasai, H.; Okada, S.; Oikawa, H.; Nakanishi, H. *Journal of the American Chemical Society* **2002**, *124*, 10944-10945.

(5) Macgillivray, L. R.; Reid, J. L.; Ripmeester, J. A. *Journal of the American Chemical Society* **2000**, *122*, 7817-7818.

(6) Karunatilaka, C.; Bučar, D.-K.; Ditzler, L. R.; Friščić, T.; Swenson, D. C.; Macgillivray, L. R.; Tivanski, A. V. *Angewandte Chemie International Edition in English* **2011**, *50*, 8642-6.

Appendix I: Solvent cut-off for UV-visible Absorption Spectroscopy

A list of solvents normally used in UV-vis spectroscopy and their absorption cutoff, (wavelength at which the solvent absorbance in a 1 cm path length cell is equal to 1 AU (absorbance unit))[1].

Solvent	**UV-cutoff**
Acetonitrile UV	190
Water	190
Hexane UV	195
Cyclopentane	198
Cyclohexane	200
Heptane	200
Isopropyl Alcohol	205
Methanol	205
Ethyl Alcohol	210
2-Methoxyethanol	210
Methyl *t*-Butyl Ether	210
n-Propyl Alcohol	210
Tetrahydrofuran UV	212
n-Butyl Alcohol	215
1,4-Dioxane	215
Ethyl Ether	215
n-Butyl Chloride	220
Isobutyl Alcohol	220
Propylene Carbonate	220
Ethylene Dichloride	228
1,1,2-Trichlorotrifluoroethane	231
Dichloromethane	245
Chloroform	245
n-Butyl Acetate	254
Ethyl Acetate	256
N,*N*-Dimethylformamide	268
Dimethyl Sulfoxide	268
Toluene	284
o-Dichlorobenzene	295
1,2,4-Trichlorobenzene	308
Methyl Ethyl Ketone	329
Acetone	330
Methyl Isoamyl Ketone	330
Methyl *n*-Propyl Ketone	331

(1) UV Cutoff http://macro.lsu.edu/HowTo/solvents/UV Cutoff.htm (accessed Feb 24, 2012).

Appendix II: Rotations and Linewidth Experiments

Table A.1: Molecules 2 & 4 of photoreacted-cinnamic acid

Goniometer orientation: α'	Chemical Shift: δ (ppm)	Linewidth: FWHM (ppm)	Crystalline Dispersion Coefficients		
			Δδ/Δα deg/ppm	Δδ/Δβ deg/ppm	Δδ/Δγ deg/ppm
2	71	27	0.019	0.044	0.22
8	67	27	0.083	0.0061	0.18
14	65	16	0.036	0.047	0.10
26	74	26	0.020	0.016	0.11
38	92	26	0.028	0.0013	0.38
50	103	33	0.036	0.011	0.65
62	109	30	0.042	0.021	0.89
72	117	29	0.041	0.023	1.045
86	143	20	3.68	5.93	0.95
92	154	29	7.29E-5	0.020	1.09
104	153	39	0.12	0.16	0.97
116	158	22	0.030	0.049	0.76
128	152	9	0.022	0.040	0.49
140	143	11	0.025	0.046	0.22
152	127	15	0.025	0.053	0.022
164	84	24	0.0043	0.051	0.18
180	69.4	28	0.019	0.044	0.22

Table A.2: Molecules 1 & 3 of photoreacted cinnamic acid

Goniometer orientation: β'	Chemical Shift: δ (ppm)	Linewidth: FWHM (ppm)	Crystalline Dispersion Coefficients		
			Δδ/Δα deg/ppm	Δδ/Δβ deg/ppm	Δδ/Δγ deg/ppm
0	75	22	0.019	0.0439	0.22
24	79	21	0.022	0.040	0.25
36	95	18	0.018	0.026	0.31
48	119	16	0.015	0.012	0.23
58	149	18	0.014	0.0012	0.071
73	180	18	0.0079	0.0031	0.29
89	207	18	0.010	0.0093	0.76
102	220	10	0.016	0.030	1.05
110	219	10	0.016	0.021	1.18
120	209	12	0.017	0.014	1.25
130	198	13	0.019	0.0032	1.26
142	171	15	0.021	0.010	1.15
150	155	15	0.023	0.024	1.02
160	126	21	0.027	0.038	0.76
170	104	21	0.059	0.081	0.45
176	86	22	0.11	0.025	0.22

Table A.3: Molecules 2 & 4 of photoreacted cinnamic acid

Goniometer orientation: β'	Chemical Shift: δ (ppm)	Linewidth: FWHM (ppm)	Crystalline Dispersion Coefficients		
			Δδ/Δα deg/ppm	Δδ/Δβ deg/ppm	Δδ/Δγ deg/ppm
0	75	22	0.019	0.044	0.22
24	122	16	0.025	0.024	0.88
36	148	20	0.022	0.0082	1.13
48	180	13	0.019	0.0068	1.28
58	207	12	0.018	0.017	1.29
73	223	11	0.015	0.027	1.13
89	223	8	0.011	0.0094	0.76
102	207	10	0.0040	0.040	0.42
110	184	19	0.010	0.0079	0.20
120	153	21	0.013	0.0093	0.029
130	131	21	0.014	0.018	0.22
142	98	22	0.016	0.029	0.36
150	84	20	0.019	0.041	0.32
160	62	21	0.024	0.050	0.19
170	56	19	0.042	0.041	0.030
176	68	16	0.11	0.025	0.22

Appendix III

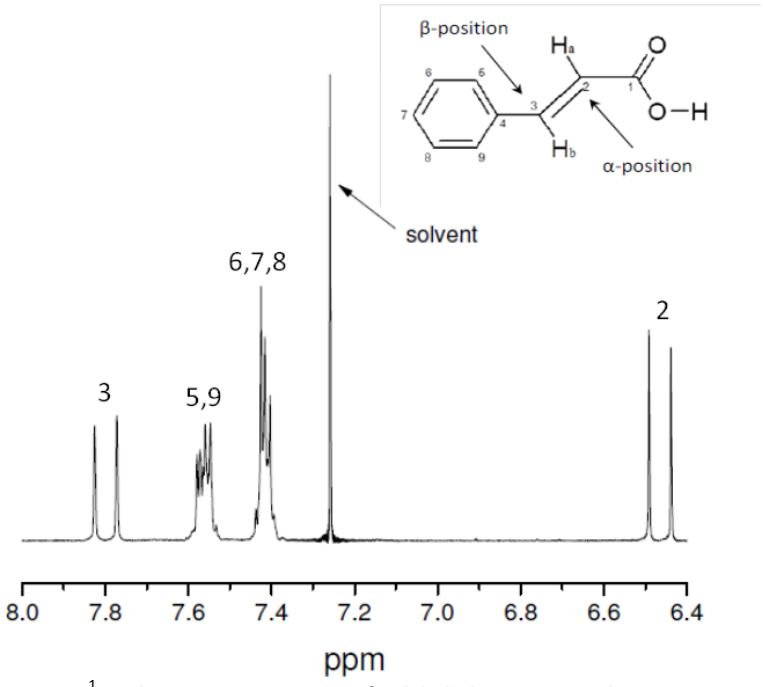

Figure A.III.1: ^{1}H solution NMR spectrum of unlabeled cinnamic acid.

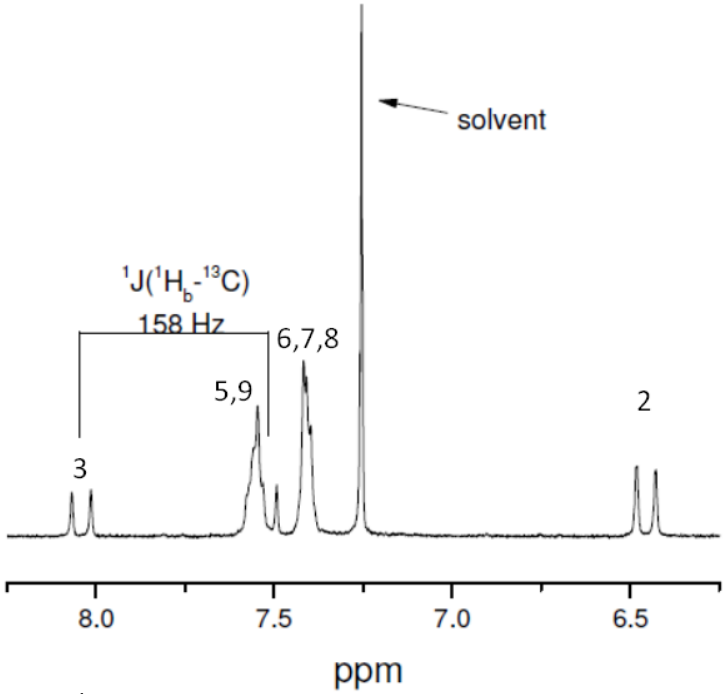

Figure A.III.2: ^{1}H solution NMR spectrum of isotopically labeled cinnamic acid (β position).